

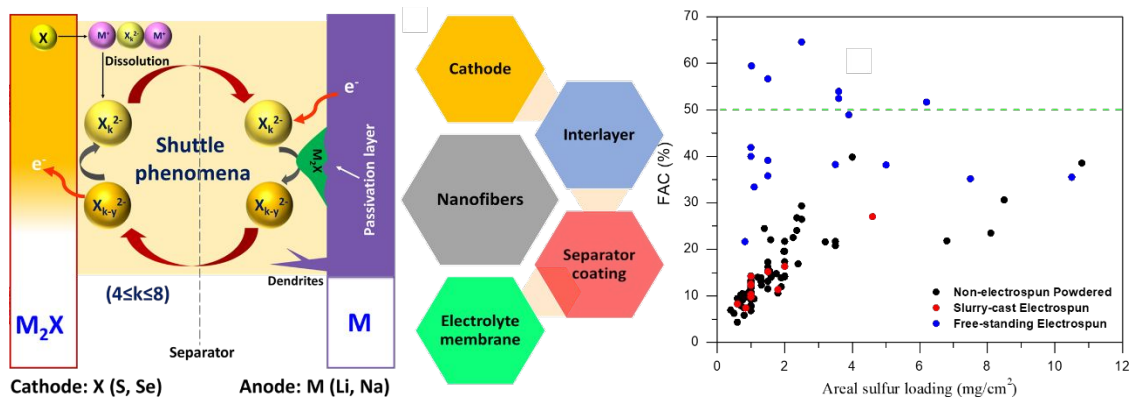
**Electrospun Nanostructures for Conversion Type Cathode  
(S, Se) based Lithium and Sodium Batteries**

Journal:	<i>Journal of Materials Chemistry A</i>
Manuscript ID	TA-REV-01-2019-000327.R1
Article Type:	Review Article
Date Submitted by the Author:	15-Mar-2019
Complete List of Authors:	Singh, Arvinder; Drexel University, Chemical and Biological Engineering Kalra, Vibha; Drexel University, Chemical and Biological Engineering

SCHOLARONE™  
Manuscripts

### Table of content:

Various electrospun nanostructures as cathode, interlayer, electrolyte membrane and separator coating in S and Se based Li and Na batteries



## **Electrospun Nanostructures for Conversion Type Cathode (S, Se) based Lithium and Sodium Batteries**

Arvinder Singh and Vibha Kalra\*

Chemical and Biological Engineering

Drexel University, Philadelphia, PA-19104, USA

\* Email: vk99@drexel.edu

### **Abstract**

Sulfur and selenium based rechargeable batteries have attracted great attention due to their high gravimetric/volumetric energy densities owing to multielectron conversion reactions. Over the last few years, rationally designed nanomaterials have played a crucial role in the continuous growth of these battery systems. In this context, electrospun nanostructures are of paramount interest for the development of these rechargeable secondary batteries due to their high surface area to volume ratio, and good mechanical stability. Here, a systematic and comprehensive review of the recent advances in the development of electrospun nanostructures as novel materials for next generation sulfur and selenium based lithium and sodium batteries is presented. In this review, we highlight the recent progress made in Li-S, RT Na-S, Li-S<sub>x</sub>Se<sub>y</sub>, RT Na-S<sub>x</sub>Se<sub>y</sub>, Li-Se and RT Na-Se batteries using electrospun carbon, polymer or heterostructures with tailored texture properties, compositions and surface functionalities (polysulfide trapping capability and catalytic activity) in cathodes, interlayers, separator coatings, and electrolyte membranes. The emphasis is placed on various synthesis strategies to design advanced electrospun nanostructures with tunable structural properties and the impact of these features on capacity, rate capability and long-term cycling. Moreover, we have introduced ‘fraction of (electrochemically) active cathode (FAC)’ as a parameter to highlight the advantages of free-standing electrospun nanostructures compared to

non-electrospun or slurry-cast electrospun counterparts. Furthermore, current challenges and prospects in the use of electrospun nanostructures in each battery system are also discussed. We believe that this review provides new opportunities in the field of advanced sulfur and selenium based rechargeable batteries using electrospun nanostructures.

## **1. Introduction:**

With rapidly depleting fossil fuel reservoirs (crude oils, coal, and natural gases), increasing environmental pollution, and human civilization, there is an urgent call for cheaper and environmentally benign renewable energy sources.<sup>1</sup> The primary key to decreasing the dependence on fossil fuels is harvesting and converting clean energy from sources such as solar, geothermal, wind, and mechanical vibration.<sup>2</sup> At the same time, it is crucial to develop highly efficient energy storage systems owing to the intermittent nature of renewable sources and ever-increasing dependency of our modern life on advanced technologies.<sup>3-5</sup> Several energy storage technologies are potentially available, which either store electricity directly into the electrical field (potential difference; electric charges) or into another form of energy such as chemical, kinetic, or potential energy.<sup>1,6,7</sup> Conventional dielectric capacitors and supercapacitors are examples for the former case mainly used for power management (e.g., frequency regulation) due to their high coulombic efficiency (~100%) and rapid charge-discharge capability.<sup>8,9</sup> Typical examples for the latter case involve flywheel (FWs; kinetic energy), compressed air energy storage (CAES; potential energy) or pumped hydro (PHS; potential energy) and electrochemical energy storage or batteries (chemical energy). Like other direct energy storage technologies, FWs are also useful for power management due to their low energy density.<sup>10</sup> PHS can be a potential candidate for bulk energy storage, but it is a site-dependent technology, which involves an extended construction period (7-8 years), reaction time (10 minutes), and massive initial investment.<sup>11</sup> Similarly, CAES demands

suitable geographic locations with salt domes, caverns, depleted aquifers or rock formation for air storage.<sup>12</sup> In contrast, electrochemical energy storage technologies or batteries can chemically store electricity and release it on demand.<sup>13</sup> Advances in rechargeable secondary batteries based on alkali lithium metal anode came about later in the 1960s.<sup>14,15</sup> Over the last two decades, rechargeable Li-ion batteries (LIBs), with an energy density between 150-240 Wh/kg and no memory effect, have established themselves globally in a wide range of electronic and communication devices.<sup>16,17</sup> Currently, these rechargeable batteries are among the prominent electrochemical energy storage technologies due to their long cycle life (~5000 cycles) and efficiency (>90%).<sup>14,18</sup> However, for their use in stationary grids and hybrid/ electric vehicles (EVs), we need sizeable LIB packs due to their limited state-of-the-art energy density.<sup>19</sup> Fig. 1 (a-b) represents the battery pack size, vehicle range and cell chemistry of variously available LIB packs in the market for hybrid and electric plug-in vehicles, respectively. It is evident that only the Tesla Model S can cope with the energy demand for the vehicle range (~500 km) targeted by automobile industries in a single charge/discharge. However, in this scenario, size and cost of the large-sized LIB packs (e.g., 85 kWh battery pack, 7104 cells, 1200 lb/540 kg, ~\$150 per kWh-Tesla Model S) impose the most crucial and insurmountable challenge. The limited energy density of LIBs is mainly due to intercalation type transition metal based heavy compound electrode materials (e.g.,  $\text{LiCoO}_2$ ).<sup>20,21</sup> Several other alternatives to  $\text{LiCoO}_2$  such as  $\text{LiFePO}_4$  and  $\text{LiNi}_{1-y-z}\text{Mn}_y\text{Co}_z\text{O}_2$  have also penetrated the market with enhanced performance.<sup>20,21</sup> Nonetheless, all these materials exhibit intrinsically limited capacity (<200-300 mAh/g) due to the number of electron transfer involved in the intercalation chemistry and crystal structure aspects during accommodation of  $\text{Li}^+$  cations.<sup>20-22</sup> The energy density values of LIBs based on these intercalation type materials are gradually reaching to theoretical limits and can be increased further at most by

30% of current values with future technical optimizations.<sup>20</sup> Therefore, LIBs may not ever reach the targeted device level 500 Wh/kg energy density and size-cost aspects for applications in hybrid/electrical vehicles.<sup>20,23</sup> Thus, there is a worldwide consensus that a revolution in rechargeable secondary batteries is needed by employing lightweight materials with multi-electron chemistry in order to use them in hybrid vehicles and large stationary grids.<sup>24</sup> Various rechargeable batteries of different chemistries based on conversion type electrodes such as metal-sulfur (e.g., Li-S and Na-S), and metal-selenium (e.g., Li-Se and Na-Se) are appealing due to their astonishing gravimetric/volumetric energy.<sup>24-28</sup> As mentioned earlier, for stationary grid storage and hybrid/electric vehicles, large-sized LIB packs are available. However, these alternate rechargeable secondary batteries will be more practical due to their projected much higher gravimetric/volumetric energy at a relatively low cost and a small size.

The cell structure of these rechargeable batteries generally comprises of a metal M (Li or Na) anode – suitable electrolyte (aqueous/non-aqueous) – X (S, Se) cathode. Lithium (Li) is the most suitable candidate among all the metal (M) anodes with a profoundly negative reduction potential of  $-3.04$  V vs. standard hydrogen electrode (SHE) and a high gravimetric capacity of  $\sim 3861$  mAh/g. In contrast, sodium (Na) exhibit relatively low gravimetric capacity of  $\sim 1166$  mAh/g and lesser reduction potentials of  $-2.7$  V vs. SHE.<sup>2,27,29-32</sup> However, Na is far more abundant than lithium (crustal content- Li (20 ppm), Na (23000 ppm)), and cheaper, which thus has prompted researchers to explore new chemistries by integrating Na with conversion-based cathodes.<sup>2,33,34</sup>

Among the high energy density conversion-based cathodes (X) from group 16, S is one of the most compelling candidates. In 1962, Herbet and Ulam reported for the first time the use of elemental sulfur (S<sub>8</sub>) as a high capacity cathode (1675 mAh/g) in rechargeable batteries.<sup>35,36</sup>

Despite their high energy density compared to conventional Li-ion batteries, metal-S batteries did not appeal significant interest due to their very short cycle life.<sup>35</sup> The seminal work reported in Li-S batteries by Nazar's group in 2009 with the rationally designed S-cathodes resuscitated the attention worldwide for revisiting the potential of room temperature metal-sulfur batteries. Fig. 1(c) presents the theoretical gravimetric and volumetric energy density of various metal-sulfur (M-S) batteries and their maximum practical operating voltage.<sup>23,36-44</sup> The Li-S batteries have the highest gravimetric energy density of  $\sim 2600$  Wh/kg compared to other M-anode based S batteries.<sup>35,44</sup> Due to their astonishing energy density, M-S batteries are also promising alternatives to large-sized LIB packs for future hybrid vehicles.<sup>23,36-44</sup> However, M-S batteries are plagued by various long-lasting technical challenges due to the lack of sustainable and highly reversible sulfur cathodes. In metal-S batteries; elemental S electrochemically reduces to  $M_2S_2/M_2S$  usually through the formation of soluble intermediate metal-polysulfides ( $M_2S_n$ ;  $3 \leq n \leq 8$ ).<sup>44,45</sup> The critical challenges for practicality of metal-S cells are (1) low conductivity of S i.e.,  $5 \times 10^{-30}$  S/cm at  $25^\circ\text{C}$  (undermined sulfur utilization and low capacity) and solid-state products  $M_2S_2/M_2S$ , (2) high reactivity (harmful by-products), (3) substantial volume expansion during reduction (e.g.,  $\sim 80\%$  in Li-S batteries from S ( $2.07 \text{ g/cm}^3$ ) to  $\text{Li}_2\text{S}$  ( $1.66 \text{ g/cm}^3$ ) conversion) reactions (mechanical instability), (4) dendrite formation at the metal anode due to non-homogeneous nucleation (short cycle life), and (5) infamous shuttle phenomena of soluble polysulfides (low coulombic efficiency and short cycle life).<sup>23,28,36-46</sup> Significant progress has been made in M-S batteries with the introduction of advanced functional nanomaterials as sulfur hosts, polysulfide blocking (interlayer) layers, thin layers on separators and selective membranes (separators).<sup>23,36-44</sup>

Another promising candidate from group 16 (VI) is selenium (Se) with its salient features such as relatively low reactivity, electrochemically similar nature to sulfur, semiconductivity

( $1 \times 10^{-3}$  S/cm) and more controllable chemistry in electrochemical cells.<sup>47-51</sup> In M-Se batteries, electrochemical reduction of Se to  $M_2Se$  ( $M = Li, Na$ ) takes place through intermediate polyselenides.<sup>50</sup> Therefore, M-Se batteries also suffer from ill-famed ‘shuttle phenomena’ in commonly used ether based liquid electrolytes and volume expansion of Se during reduction, as in the case of M-S batteries.

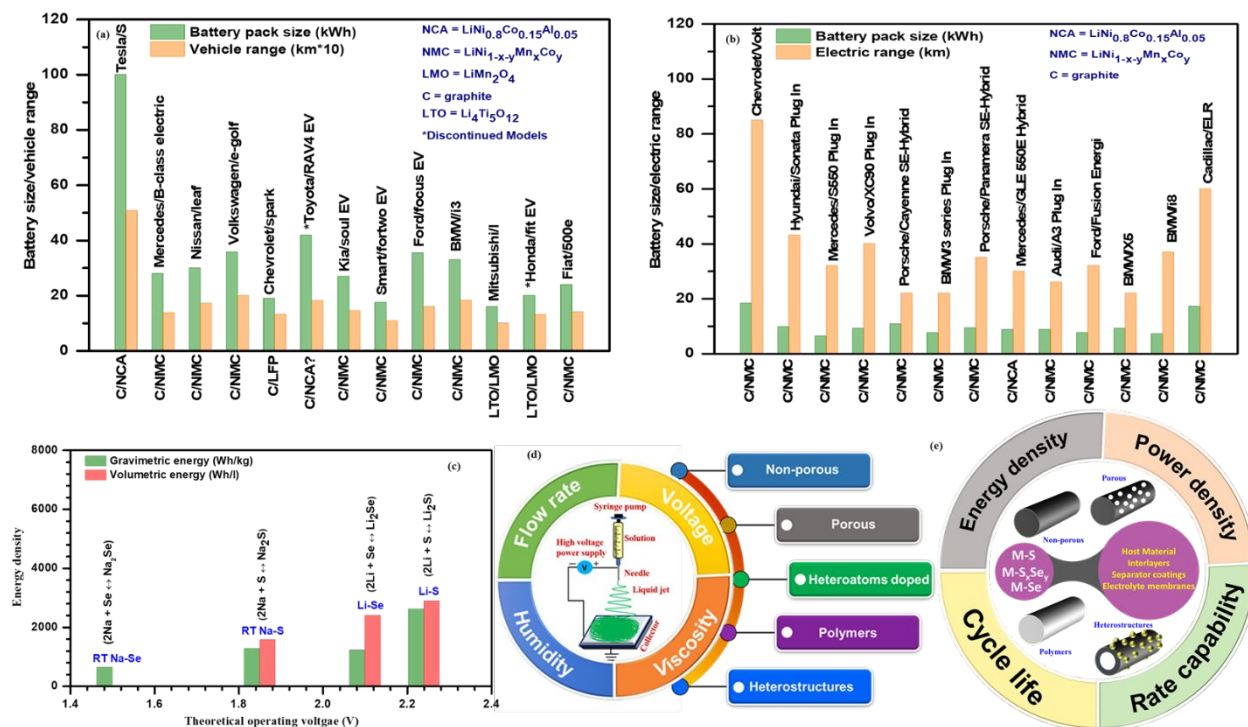


Fig. 1 Battery size and electrical vehicle range for various available models of LIB packs for (a) hybrid vehicles and (b) electric plug-in vehicles. The x-axis shows various chemistries (cell structures) in these batteries. The model/company details are mentioned vertically in figures for each battery pack. (c) Gravimetric and volumetric energy densities of X (S, density  $\sim 1.96$  g/cm<sup>3</sup>; Se, density  $\sim 4.819$  g/cm<sup>3</sup>) cathode based rechargeable batteries using M-metal anodes ( $Li^+$ ,  $Na^+$ ), (d) A typical electrospinning set up and parameters influencing the physical properties of different nanofiber structures, and (e) A schematic showing the use of different electrospun structures as various components in M-S,  $M-S_xSe_y$  and M-Se batteries and their effect on the electrochemical characteristics (e.g., energy and power densities, cycle life, rate capability) of these devices.



Moreover, metal-Se cells exhibit low theoretical capacity of  $\sim 675$  mAh/g due to the high mass of selenium in comparison to sulfur.<sup>50</sup> However, regarding volumetric capacity, a relatively higher density of selenium ( $4.809$  g/cm<sup>3</sup>) than sulfur ( $\alpha$ -S,  $2.07$  g/cm<sup>3</sup>) allows metal-Se batteries to compete with metal-S batteries (e.g.,  $3467$  mAh/cm<sup>3</sup> for Li-S batteries and  $3253$  mAh/cm<sup>3</sup> for Li-Se).<sup>50</sup> Other essential advantages of elemental Se are (a) higher utilization rate and faster electrochemical reactions rate due to selenium's semiconducting nature, (b) higher autoignition and melting point than S (S =  $115.2^\circ\text{C}$ ; Se =  $221^\circ\text{C}$ ) - relatively safer during short-circuiting and overheating, and (c) compatibility with cost-effective carbonate-based electrolytes due to considerably stable intermediate poly-selenides.<sup>50</sup> While M-Se batteries have invaluable advantages and compete with M-S batteries, they are still in their nascent stage.

In the last few decades, the development of nanoscale materials with different morphologies and dimensionalities (0-D, 1-D, 2-D, and 3-D) has played a deterministic role in the advancement of secondary M-X (S, Se) batteries. Among the nanoarchitectures explored in these batteries, electrospun 1-D materials have emerged as forerunner due to their interesting peculiarities such as 1-D longitudinal electron transport, high surface to volume ratio and less agglomeration than ordinary nanoparticles.<sup>52</sup> Among many available synthetic strategies including template-directed synthesis, solution-phase method, vapor-phase route, self-assembly, and electrodeposition, electrospinning is one of the most straightforward, cost-effective, and industrially viable technology for developing 1-D nanofibrous materials.<sup>53</sup> Electrospinning is a versatile technique that uses electrohydrodynamical mechanism to fabricate 1-D organic, inorganic and hybrid nanofibers on a large scale with the incorporation of interesting properties such as porosity, low density, and controllable dimension/diameter.<sup>53</sup> Moreover, electrospinning allows the production of application-oriented homogeneous and heterogeneous nanofibers in a variety of

solid non-porous, porous, hollow, and core-shell architectures for their use in different M-X (S, Se) batteries.<sup>53-56</sup> In the recent past, rationally designed electrospun carbon nanofibers (CNFs), functionalized carbon/polymer nanofibers, and composite nanofibers (e.g., CNFs/oxides, CNFs/carbides) nanofibers, and heteroatom-doped (e.g., N-doped CNFs) have been utilized in M-S batteries.<sup>43,57-59</sup> These nanostructures have shown great potential for M-S batteries not only as functional sulfur hosts for trapping the dissolved polysulfides (through physical adsorption and confinement, chemisorption, polar or Lewis-acid type interactions), but also as electrolyte membranes/functional separator coatings, or interlayers.<sup>43,58,59</sup> As the electrochemistry of M-Se batteries is analogous to M-S batteries; there is a growing interest for the use of such electrospun nanostructures in M-Se batteries as selenium hosts, polyselenide blocking layers and functional separators. Since the gravimetric capacity (energy) of the M-X (S, Se) batteries depends on the total weight of all the components, it is vital to eradicate the additional dead elements such as binders, current collectors (e.g., Al foil) and conducting additives (e.g., carbon black). Electrospun structures have the advantage of free-standing nature, which makes them even more suitable for such M-X (S, Se) batteries.<sup>43,58,59</sup>

There exist several articles that review the recent progress on the application of electrospun nanostructures in rechargeable batteries.<sup>52,53,56,58,60-73</sup> However, these review articles primarily focus on their use in Li-ion and Na-ion batteries and rarely discuss conversion cathode (S, Se) based batteries.<sup>4,55,56,63,66,67,72,73</sup> To the best of our knowledge, there is no review article in the literature comprehensively focusing on the recent progress made in various next-generation sulfur (Li-S, Na-S), sulfur-selenium (Li-S<sub>x</sub>Se<sub>y</sub> and Na-S<sub>x</sub>Se<sub>y</sub>), and selenium (Li-Se and Na-Se) batteries using rationally designed electrospun nanostructures. In this article, we critically review the synthesis strategies used for electrospinning of novel nanostructures and the recent progress

accomplished with function-directed use of these nanostructures as cathodes, interlayers, and electrolyte membranes/separators coatings in lithium and sodium metal-based sulfur/selenium batteries. First, we provide an introduction of M-S (Se) batteries and a brief overview of the electrospinning technique to build a foundation for analyzing structure-property correlation given in the literature. The review then focuses on the recent advances made in Li-S batteries using various electrospun nanostructures of (a) carbon, (b) polymer, and (c) oxide, carbide, and metal based heterostructures as cathodes, interlayers, separator coatings and electrolyte membranes. We further discuss the recently reported strategies for the advancement of RT Na-S, and Se based lithium and sodium batteries ( $\text{Li-S}_x\text{Se}_y$ , RT Na- $\text{S}_x\text{Se}_y$  and RT Na-Se) using electrospun nanostructures. Furthermore, we define a significant parameter denoted as ‘fraction of (electrochemically) active cathode (FAC)’ and calculate the effective sulfur utilization and effective capacity in Li-S cells for a comparative analysis between various powder/slurry based nanomaterials and electrospun nanostructures. Finally, we provide a concluding remark on the state-of-the-art progress and remaining critical challenges along with prospects towards electrospun nanostructures based M-S (Se) batteries.

## **2. A brief introduction of electrospinning:**

Electrospinning is a fiber-spinning process that uses high voltage ( $\sim 7\text{-}32$  kV) to produce fibers with controllable diameters ranging from a few nm to micrometers. It is a versatile technique that can be tailored to control the degree of graphitization, heteroatom functionality (i.e., N), and a variety of function-directed homogeneous and heterogeneous complex architectures such as hollow, core-shell or porous nanofibers.<sup>53</sup> Electrospinning set up typically consists of four major components viz., a metallic needle with a blunt tip, a high voltage source/electric field supply, a syringe filled with the viscous polymeric/spinning solution, and a grounded conducting

substrate/collector (e.g., Al-foil) as shown in Fig. 1(d).<sup>54</sup> During the electrospinning process, when the applied electric field (voltage) overcomes the surface tension of the solution droplet, the charged solution gets ejected as a jet towards the grounded conducting collector.<sup>55</sup> The jet typically undergoes a whipping motion enabling significant thinning of the diameter. While traveling to the collector, the solvent evaporates from the jet solution and charged fibers eventually get accumulated on the collector.<sup>74</sup> This spinning procedure gives a non-woven fiber mat made up of nanofibers with diameters between few nanometers to micrometers. Several factors are known to influence the diameter of nanofibers and the final nanostructure including intrinsic properties of the spinning solution such as electrical conductivity, concentration, surface tension and viscosity as well as operating conditions such as flow rate, applied voltage/electric field intensity, tip-collector distance and humidity.<sup>54,55,74</sup> Since surface tension, conductivity and concentration are related to the spinning solution, which is largely determined by the targeted application, the flow rate of the solution turns out to be a critical factor in determining the diameter of fibers as follows:<sup>54,75</sup>

$$D_f \sim c^{1/2} (Q/I)^{2/3} \gamma^{1/3}$$

Where  $D_f$  is the fiber diameter, 'c' is the concentration, 'Q' is the flow rate,  $\gamma$  is the surface tension, and 'I' is the characteristic current of the spinning set-up. Therefore, following the above power law, the diameter of the fibers is predicted to increase with the increasing flow rate, which is in agreement with the experimental findings reported earlier.<sup>76</sup> The diameter of the fibers is also influenced by the viscosity and generally increases with increasing viscosity of the solution as follow:<sup>54,75</sup>

$$D_f = k\eta^n$$

Where  $\eta$  is the viscosity of the spinning solution ( $\eta$  is proportional to  $M^a$ ),  $M$  is the molecular weight of polymers,  $k$  and  $a$  are constants (function of applied temperature, types of polymer and solvent), and  $n$  depends on polymers. The diameter of the as-spun fibers further decreases during heat treatments (for formation of carbon, for example) due to evaporation of the residual solvents and removal of heteroatoms. Furthermore, the viscosity and surface tension of the solution must be adequate in order to get smooth fibers. A solution with very low viscosity will result in particles (electrospraying) instead of continuous smooth fibers (electrospinning).<sup>54,55,74</sup> In contrast, a solution with very high viscosity will be enormously hard to pull and will result in unstable feed rate.<sup>54,55,74,75</sup> Humidity is another factor, which strongly affects the morphology of the fibers. A highly humid environment will result in condensation of water on the fiber surface and lead to the pore formation on the surface.<sup>54,55,74</sup> Applied voltage and tip-collector distance also affects the structure and morphology of the fibers. A high applied voltage and small tip-collector distance will reduce the time for the solvent to evaporate and result in bead formation. Therefore, tip-collector distance (voltage) should be optimum to form bead-free smooth fibers.<sup>54,55,74,75</sup>

The electrospinning technique offers immense opportunities to develop unique fiber architectures such as porous, hollow, or core-shell by varying post-treatment conditions, polymer solutions or using specially designed spinnerets.<sup>74,77</sup> Generally, the porosity/texture properties can be controlled/enhanced by (a) changing the post-fabrication heating process (heating at different temperatures in different environment such as Ar, H<sub>2</sub>, CO<sub>2</sub>)<sup>78-80</sup>, (b) activating nanofibers with various agents (e.g., KOH)<sup>81</sup> (c) using additional sacrificial polymers (e.g., Nafion, polymethyl methacrylate, polystyrene) along with the primary polymer such as polyacrylonitrile (PAN; a common polymer for carbon nanofibers with high yield)<sup>82-84</sup>, and (d) employing thermally stable and easily removable hard templates (e.g., SiO<sub>2</sub>, ZnO, Fe, Ni, Fe).<sup>53-55,74,75,77</sup> Co-electrospinning

or coaxial electrospinning techniques allow the synthesis of hollow or core-shell nanofibers to impart multiple chemistries/functionalities into a single fiber.<sup>85,86</sup> In these approaches, two different solutions flow into either single or two specially designed concentric capillaries/nozzles using two individual syringe pumps and eventually consolidate after stretching and solvent evaporation.<sup>53,54,85,86</sup> The hollow or core-shell nanofibers can be designed by carefully choosing solvents and precursors (polymers, alkoxides or salts) for core and shell solutions. The final structure of the fibers depends on the miscibility of the core and shell solutions. The miscible solutions usually result in various phases/porosity into fibers due to phase separation during solidification whereas immiscible solutions give core-shell nanofibers. Hollow nanofibers can be produced by carefully selecting the core solution (e.g., mineral oil or aqueous), which can be easily removed by pyrolysis or selective dissolution using solvents/etching agents.<sup>86</sup> More details about the choice for core and shell solutions and governing electrospinning parameters to obtain hollow and core-shell nanofibers are available in recently published review articles.<sup>52,85,86</sup>

So far, we have discussed the pros and cons/challenges of various emerging rechargeable battery chemistries based on conversion type S and Se cathodes. Then we briefly introduced the electrospinning technique and various parameters influencing the final structure and morphology of the fibers. As mentioned above, the one-step electrospinning technique is capable of producing homogeneous/heterogeneous function-directed nanofiber structures on a large scale. In the recent past, various non-porous, porous, core-shell, and hollow nanofiber structures of carbon, metal oxides, polymers and composites have been introduced to M-X (S, Se) batteries aiming at their long cycle life, high coulombic efficiency and enhanced capacity. In subsequent sections, we will focus on the use of such electrospun structures in various metal-sulfur (selenium) batteries as sulfur (selenium) hosts, polysulfide (selenide) blocking layers (interlayers), and selective

membrane/separators. Finally, we will provide our conclusions and future perspectives on the roadmap for developing M-X (S, Se) batteries using these advanced electrospun nanostructures.

### 3. Electrospun Nanofibers in Metal-Sulfur and Metal-Selenium Batteries:

A typical metal-sulfur (selenium) battery comprises of sulfur (selenium) cathode, a separator, an electrolyte, and a metal (M) anode.<sup>36,46,87</sup> The difference between the electrochemical potentials of the anode ( $\mu_M^{oc}$ ) and cathode ( $\mu_X^{oc}$ ) at the open circuit state defines the maximum voltage that the M-S (Se) battery can hold ( $\phi_{oc}$ ).<sup>46,51,87</sup> Upon discharge, the electrochemical potential of the S (Se) cathode increases ( $\mu_X$ ) until the battery reaches the cut-off potential ( $\phi$ ).<sup>46,51,87</sup>

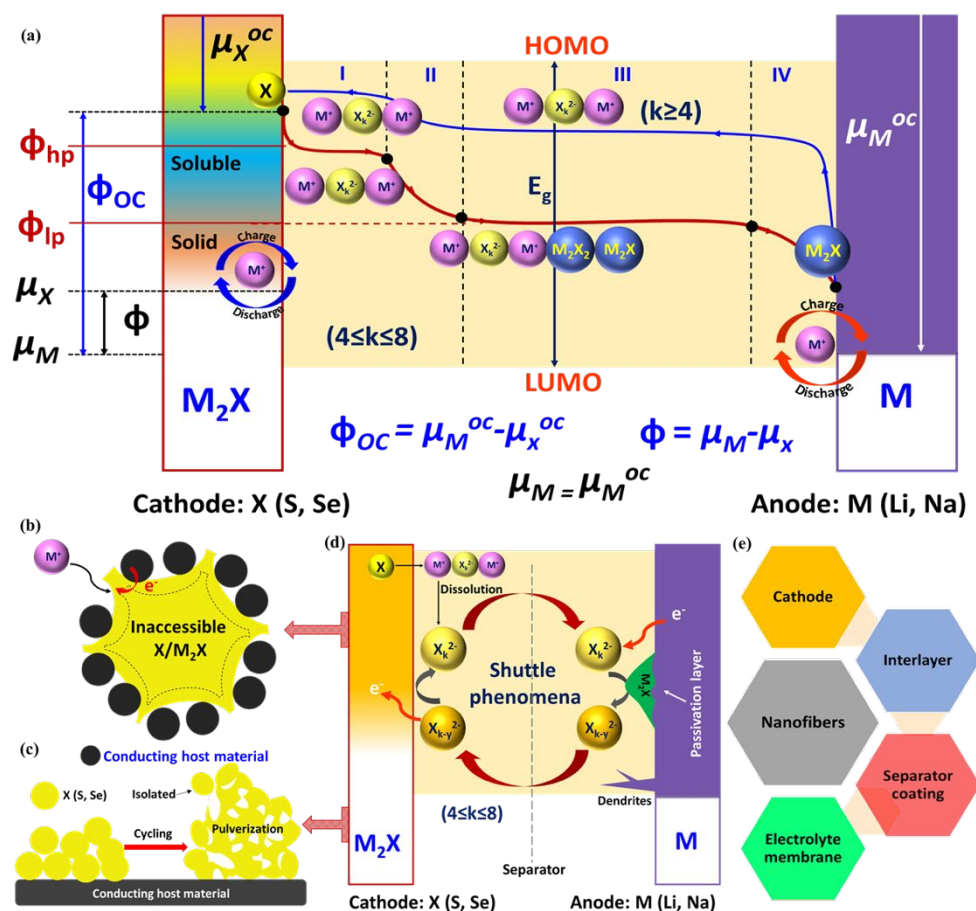


Fig. 2 A schematic showing (a) fundamental electrochemistry involved in M-S (Se) batteries, (b) effect on the utilization of X (S, Se) due to inaccessible insulating cores, (c) pulverization of electrodes due to repeated volume changes, (d) loss of active material due to shuttle effect and

resultant passivation layer on the metal (M) anode, and (e) use of electrospun nanofibers as various components in M-S (Se) batteries.

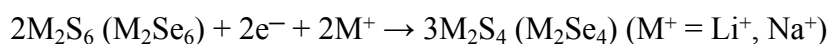
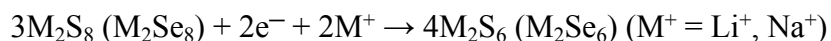
In the typical discharge process, S (Se) electrochemically reduces to  $M_2S/M_2Se$  ( $M^+$ :  $Li^+$ ,  $Na^+$ ) via soluble intermediate poly-sulfides (-selenides), i.e.,  $(S, Se)_k^{2-}$  ( $4 \leq k \leq 8$ ).<sup>46,88</sup> Therefore, M-S (Se) batteries typically show two plateaus during the electrochemical reduction of S (Se) to  $M_2S/M_2Se$  (Fig. 2 (a)).<sup>46,88</sup> The high plateau at a potential  $\phi_{hp}$  (e.g.,  $\sim 2.30$  V for  $S^{46}$  and  $\sim 2.1$  V for  $Se^{88}$  in ether electrolyte based Li-S (Se) cells) corresponds to the reduction of elemental S (Se) to higher order soluble poly-sulfides (selenides) (region I).<sup>36,46,47,50,51,89-93</sup> In case of M-S batteries, the most stable allotrope at 25 °C i.e., octasulfur (cyclo- $S_8$ ) known as orthorhombic  $\alpha$ - $S_8$  is reduced through ring opening, resulting in the formation of soluble higher-order polysulfides (region I):<sup>36,46,89-93</sup>



On the other hand, trigonal Se (t-Se) constructed from Se chains is the most thermodynamic stable phase among all the major allotropes of Se. The reduction process of Se resembles that of sulfur cathode, therefore results in the formation of long chain polyselenides in ether electrolyte (region I)<sup>47,50,51</sup>:

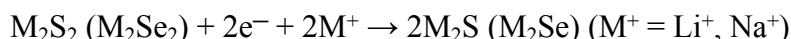
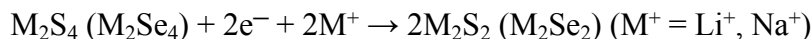


The sloped region (II) between higher and lower plateaus (region with a change in chemical potential) is due to the conversion of higher order poly-sulfides (selenides) to lower order poly-sulfides (selenides) through disproportion reactions given below:<sup>36,43,46,47,50,51,87,89-95</sup>





The liquid-liquid transition of higher order polysulfides (polyselenides) to lower order polysulfides (polyselenides) is the most complicated step.<sup>36,46,89-93</sup> The second plateau at a lower potential  $\phi_{lp}$  (e.g.,  $\sim 2.1$  V for  $S^{46}$  and  $\sim 1.95$  V for  $Se^{88}$  in ether electrolyte based Li-S (Se) cells) represents a further reduction of these lower order intermediate poly-sulfides (selenides) to solid state products, i.e.,  $M_2S/M_2Se$  (region III and IV):<sup>36,46,47,50,51,89-93</sup>



The transition of solid-state S (Se) to soluble polysulfides (polyselenides) and lower order polysulfides (polyselenides) to solid-state  $M_2S_2$  ( $M_2Se_2$ ) involve fast or moderate kinetics, while the last solid to solid transition of  $M_2S_2$  ( $M_2Se_2$ ) to  $M_2S$  ( $M_2Se$ ) is kinetically slow and likely suffers from high polarization.<sup>36,46,47,50,51,89-93</sup> Consequently, the discharge process terminates rapidly once the  $M_2S$  ( $M_2Se$ ) covers the whole cathode framework.<sup>36,46,89-93</sup> It is noteworthy that the discharge/charge rate, stability of intermediate species, electrolyte composition, chemical equilibria between each type of polysulfide (polyselenide) species, and that the choice of solvent ultimately governs the mechanistic pathway for the conversion of S (Se) to  $M_2S$  ( $M_2Se$ ).<sup>36,46,47,50,51,89-93</sup> During oxidation (charge), a reversible solid-liquid-solid process occurs and  $M_2S/M_2Se$  products convert back to elemental S (Se) via soluble intermediates polysulfides (polyselenides).<sup>36,43,46,47,50,51,87,89-95</sup> The M-S (Se) batteries are confronted with the long-lasting challenges, which are discussed below:

(i) the poor electrical and ionic conductivity of S and its deep discharge products  $M_2S_2/M_2S$  result in high internal resistance of battery (large polarization  $\rightarrow$  reduced energy efficiency of battery).<sup>36,46,89-93</sup> Further, due to poor conductivity of S (or  $M_2S_2/M_2S$ ), large insulating cores formed during S-infiltration/cathode preparation (or  $M_2S_2/M_2S$  deposition during discharge)

become inaccessible and lead to underutilization of active material (low capacity) as shown in Fig. 2(b).<sup>36,46,89-93</sup> Therefore, use of S as cathode material necessitates its integration with nanoscale conducting host materials.<sup>36,46,89-93</sup> Although Se has semiconducting nature, it also requires (like S) conducting host materials in order to suppress shuttle effect, long cycling and high coulombic efficiency.<sup>47,50,51</sup>

(ii) The repeated volume change (expansion during reduction and shrinkage during oxidation) during reduction/oxidation causes pulverization of the electrode (mechanical instability due to cracks, fractures, loose contact (or complete isolation) of active material with conducting network or current collector) as shown in Fig. 2(c), which ultimately leads to fast capacity decay.<sup>36,46,47,50,51,89-93</sup>

(iii) the infamous shuttle effect, which involves the shuttling of dissolved polysulfides (polyselenides) between the M anode and S (Se) cathode during the charge process.<sup>47,50,51</sup> The shuttle effect results in the loss of active material and side reduction reactions with the M anode (passivation layer of  $M_2S/M_2Se$ ) as shown in Fig. 2(d), which ultimately lead to short cycle life.<sup>36,43,46,47,50,51,87,89-95</sup>

(iv) the anode (M) instability due to dendrite (Fig. 2(d)) and solid electrolyte interphase (SEI) layer formation, causing low deposition efficiency of M, and irreversible capacity loss upon charging process or short-circuiting of the battery system.<sup>36,46,47,50,51,89-93</sup> In this scenario, an excess amount of M is required to pair with S (Se) cathode, which eventually deteriorates the energy density of battery systems.<sup>36,46,47,50,51,89-93</sup>

In the context of the practically challenging unique electrochemistry of M-S (Se) batteries, various rationally designed electrospun nanostructures of carbon, transition metal oxides, carbides, polymers, and nanocomposites have been employed in M-S (Se) batteries. These novel structures

not only help to minimize the escape of polysulfides (selenides) towards the anode via physical or chemical adsorption, polar-polar, Lewis acid-base or thiosulfate type interactions but also provide channels for electron transfer and accommodate volume expansion during reduction/oxidation reactions. Consequently, these materials actively govern the capacity, rate performance, cycling and coulombic efficiency of M-S (Se) batteries. The following sections provide a comprehensive perspective of the recent progress made in M-S (Se) batteries with the use of various electrospun nanostructures as host materials in the cathode, interlayers, separator coatings and electrolyte membranes.

### **3.1. Electrospun nanostructures in Li-S batteries**

#### **3.1.1 Carbon nanofibers in Li-S batteries**

##### ***CNF-based cathodes with Sulfur as active material:***

Electrospun carbon nanofibers (CNFs) have attracted considerable attention for a long time in Li-S batteries as conducting host material due to their low density, high surface to volume ratio, nanosized pore distribution, good electrical conductivity, and remarkable structural strength. However, electrospun CNFs from a single polymer matrix usually offer insufficient surface active sites due to their considerably small surface area (mostly non-porous) and micro/meso pore volume. Therefore, S-cathodes prepared using these non-porous CNFs and the most common melt-sulfur infiltration technique (155°C/10-12 h) result in accommodation of sulfur mostly into inter-fiber macropores/voids, which limit prolonged cycling of the Li-S cell due to severe polysulfide dissolution.<sup>96</sup> Over the past decade, electrospun carbon nanofibers with different morphologies and architectures have been designed for Li-S batteries to surmount these challenges.<sup>81-84,97-111</sup> Ji *et al.* reported early work with the use of PAN/PMMA (polyacrylonitrile/Poly (methyl methacrylate); mass ratio 1:1) derived electrospun porous CNFs (Fig. 3 (a)) and chemically

deposited sulfur as cathodes in Li-S batteries.<sup>82</sup> The prepared CNF-S with 42 wt% S in the composite showed a high specific capacity of  $\sim 1439$  mAh/g at 0.05 C rate with 85% capacity retention after 30 cycles (Fig. 3 (b)). The high specific capacity was attributed to a large contact area between chemically deposited sulfur and porous CNFs (surface area =  $123$  m<sup>2</sup>/g and pore volume =  $0.27$  cm<sup>3</sup>/g). However, the poor cycling stability of these cathodes was possibly due to (a) significant loss of sulfur confined in pores under wetting conditions during cell operation (ether electrolyte), which ultimately resulted in severe polysulfide dissolution<sup>112</sup>, and (b) weak interactions (physical adsorption) of the intermediate polysulfides with nonpolar CNFs.<sup>113,114</sup> It is important to mention that addition of the additive and binder during cathode preparation ultimately reduced the sulfur content to 29.4% in this study. Recently, Zhang *et al.* developed free-standing porous graphitic carbon nanofibers (surface area =  $409$  m<sup>2</sup>/g) using *in-situ* formed FeO<sub>x</sub> nanoparticles (10-30 nm) (during carbonization at 800°C in N<sub>2</sub>) as a template and employed them in Li-S batteries without binders or additives.<sup>105</sup> The developed porous graphitic CNF/S cathodes (Fig. 3 (c)) with a high sulfur loading of 70 wt% in the final cathode delivered a high initial capacity of  $\sim 840$  mAh/g at 1C rate with  $\sim 83\%$  capacity retention over 200 cycles (Fig. 3 (d)). The excellent electrochemical performance of the porous graphitic CNF/S cathodes was ascribed to several structural advantages including porous carbon structures (polysulfide reservoirs), improved electrical conductivity of CNFs due to graphitization (efficient sulfur utilization and fast reaction kinetics), and inherent macropores/voids (facile diffusion of Li<sup>+</sup> ions) of free-standing interlaced nanofibers. It is important to mention that the areal capacity of Li-S cells is mostly under-emphasized in the literature, but it is as crucial as the gravimetric capacity for practical applications. The areal capacity of the CNF/S based Li-S cells discussed above is  $< 5$  mAh/cm<sup>2</sup>.<sup>81,82,105</sup> Considering the lower average voltage ( $\sim 2.15$  V) than that of LIBs ( $\sim 3.5$ V),

practical Li-S cells will need to have an areal capacity of  $\geq 6$  mAh/cm<sup>2</sup> and specific capacity of  $\geq 800$  mAh/g. Therefore, practical Li-S cells demand areal sulfur loading of  $\geq 5$  mg/cm<sup>2</sup> along with high sulfur content ( $\geq 70\%$  in the final cathode) and sulfur utilization ( $\geq 70\%$ ) to outperform the energy density of commercial Li-ion batteries (ceiling areal capacity  $\sim 4$  mAh/cm<sup>2</sup>).<sup>115,116</sup> These prerequisites recently encouraged researchers to develop Li-S batteries with high areal sulfur loading and sulfur content. However, an increase in the areal sulfur loading (or areal capacity) and sulfur content brings about slow kinetics due to the formation of inaccessible cores of insulating sulfur, poor electrolyte wetting of the cathode, underutilization of sulfur, extreme pulverization of the cathode due to repeated volume change, and exacerbated shuttle effect. These severe issues ultimately result in the limited areal/gravimetric capacity, low coulombic efficiency, and the compromised cycle life of Li-S batteries.<sup>110,111</sup> Therefore, many research efforts have been aimed at development of structurally featured electrospun CNF with large pore volume and highly distributed pores to overcome the abovementioned problems.<sup>84,110,111,117</sup> Pore volume of the porous host matrix directly influences the achievable sulfur loading in the cathodes as given below<sup>91,96</sup>:

$$\text{Sulfur content (\%)} = 100 * \frac{\frac{V}{1.8}d}{\frac{V}{1.8}d + 1}$$

Where  $V$  is the pore volume, and  $d$  is the density of sulfur (2.07 cm<sup>3</sup>/g for  $\alpha$ -S). In this regard, free-standing CNFs provide added advantage of large pore volume along with other benefits such as elimination of dead weight (binders, conducting additives and additional current-collectors). Besides the high pore volume, wide pore size distribution is another valuable asset of the CNF for their sustainable performance at high sulfur loading. Micropores (<2 nm) in CNFs enable large interfacial contact area with sulfur and serve as reservoirs for trapping the intermediate polysulfides. Nevertheless, micropores often lead to low pore volume (low sulfur content) and

slow  $\text{Li}^+$  transport (sluggish kinetics). In contrast, mesopores (2-50 nm) and macropores (>50 nm) of CNFs are desirable for achieving high sulfur content and better electrolyte penetration but generally result in inferior cycling stability. Consequently, most recent focus is on the development of CNFs with complex hierarchical porosity (micropores as well as mesopores/macro-pores), which could potentially accommodate a high amount of sulfur through large pore volume, provide a large contact area for effective sulfur utilization, accommodate volume changes, and also trap polysulfides through micropores for prolonged cycling of Li-S batteries.<sup>110,111</sup> Moreover, the robust free-standing 3D architecture of interlaced CNF could provide a high structural/mechanical strength at high sulfur loading during the volume changes.<sup>84,110,111,118</sup> In most cases, activation process or sacrificial templates have been used to design such CNF structures. For example, Lee *et al.* prepared sulfur cathodes (loading  $\sim 2.2 \text{ mg/cm}^2$ ,  $\sim 64 \text{ wt\%}$  in the final cathode) using multichannel carbon nanofibers (MCNFs; surface area  $\sim 1617 \text{ m}^2/\text{g}$  and pore volume =  $1.82 \text{ cm}^3/\text{g}$ ) developed through a single-nozzle co-electrospinning technique.<sup>81</sup> The PAN/PMMA blend was electrospun and then activated using KOH ( $6\text{KOH} + \text{C} \rightarrow 2\text{K} + 3\text{H}_2 + 2\text{K}_2\text{CO}_3$ ;  $T = 800^\circ\text{C}$ ) to prepare MCNFs. The MCNF structures possessed parallel mesoporous channels (hollow channels with diameter  $\sim 20 \text{ nm}$  along the length of carbon fibers) interconnected to micropores (Fig. 3 (e)). The sulfur was infiltrated by combining chemical precipitation and melt diffusion ( $155^\circ\text{C}/12 \text{ h}$ ) processes. The TEM and elemental mapping results showed that sulfur was infiltrated within the fiber as given in Fig. 3 (f-g). The MCNFs/sulfur composite cathodes displayed excellent rate performance (initial capacity of  $\sim 1351 \text{ mAh/g}$  at  $0.2 \text{ C}$  rate and  $847 \text{ mAh/g}$  at the  $5 \text{ C}$  rate), maintaining  $\sim 68\%$  of the initial capacity after 300 cycles at  $0.2 \text{ C}$  rate. Moreover, these MCNFs/S cathodes with  $\sim 4.6 \text{ mg/cm}^2$  sulfur loading showed a high initial capacity of  $\sim 1000 \text{ mAh/g}$  at a  $0.5\text{C}$  rate with  $\sim 76\%$  capacity retention after 200 cycles (Fig. 3(h)). The excellent electrochemical

performance of Li-S cells was attributed to the novel MCNF structure where the parallel mesoporous channels promoted high sulfur loading and utilization, while microporous channels assisted with functional groups act as polysulfide reservoirs.

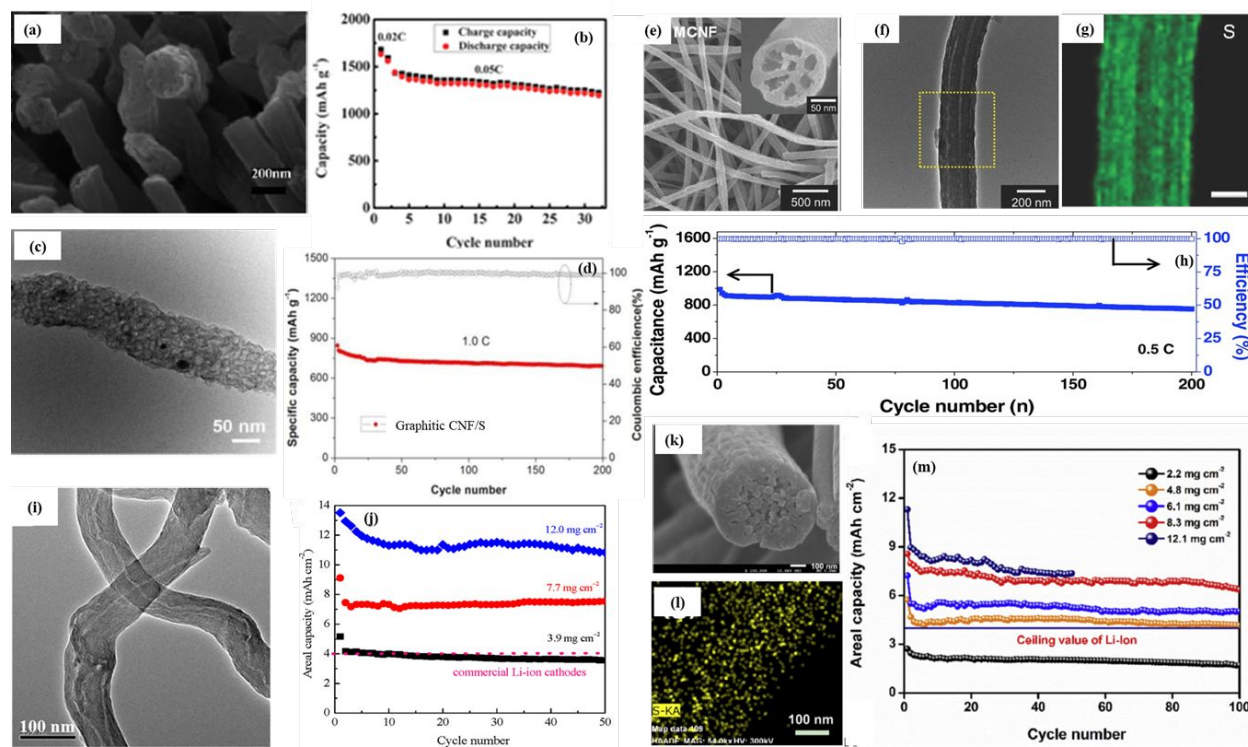


Fig. 3 (a-b) SEM image of CNF-S nanocomposite and its cycling performance at a constant rate of 0.05 C after an initial activation processes at 0.02 C for 2 cycles, respectively (Reproduced with permission from ref. 82. Copyright 2014 The Royal Society of Chemistry.); (c-d) TEM image of porous graphitic CNFs after sulfur infiltration, and cycling performance and coulombic efficiency of graphitic CNFs/S cathodes for 200 cycles at a current rate of 1 C (Reproduced with permission from ref. 105. Copyright 2016 The Electrochemical Society.); (e) Low- and enlarged cross-sectional (inset) FE-SEM image of MCNFs, (f) TEM image of the sulfur-embedded MCNFs, (g) EELS dot mapping of the sulfur in sulfur-embedded MCNFs (scale bar: 50 nm), and (h) Discharge capacity and Coulombic efficiency of MCNFs/S cathodes with  $\sim 4.6$  mg/cm<sup>2</sup> sulfur

loading over 200 cycles at 0.5C rate (Reproduced with permission from ref. 81. 2016 WILEY-VCH Verlag GmbH & Co. KGaA, Weinheim.); (i-j) TEM image of CNF/CNT electrode and areal capacity of CNT/CNF/S cathodes with different sulfur loading by stacking different layers during cycling at the current density of 0.6 mA/cm<sup>2</sup>, respectively (Reproduced with permission from ref. 105. 2018 American Chemical Society.); (k-l) FE-SEM image of HPCNF/S cathode and EDS mapping of sulfur and (m) cycle performance of the Li-S cells with HPCNF/S cathode at sulfur loading from 2.2 to 12.1 mg/cm<sup>2</sup> at 0.2 C-rate (Reproduced with permission from ref. 111. 2017 Elsevier Ltd).

Similarly, Zhang *et al.* recently used sulfur infiltrated electrospun porous CNF/carbon nanotubes (CNT) mats as cathodes and achieved a high areal capacity in Li-S batteries.<sup>110</sup> The free-standing porous CNF/CNT mats were fabricated by electrospinning a solution of SiO<sub>2</sub> (template)/PAN/CNT in dimethylformamide (DMF) and tetrahydrofuran (THF) solvents. The pyrolysis of PAN and removal of SiO<sub>2</sub> nanoparticles allowed CNF/CNT mats to achieve high surface area ~1020 m<sup>2</sup>/g, pore sizes between 2-10 nm, and large pore volume of ~1.66 cm<sup>3</sup>/g. Moreover, the CNT structures embedded into CNFs (Fig. 3 (i)) resulted in a more flexible 3D CNF/CNT architecture with improved electrical conductivity and mechanical stability. Therefore, the developed CNT/CNF/S cathodes (stacked two layers with the total sulfur loading of ~3.9 mg/cm<sup>2</sup>, ~62 wt%) through solution infiltration method (S/CS<sub>2</sub>) displayed a high initial discharge capacity of ~1321 mAh/g (5.15 mAh/cm<sup>2</sup>) at 0.1 C rate and excellent cycling stability with ~80% capacity retention after 100 cycles. Moreover, the CNT/CNF/S cathodes with a high sulfur loading of ~12.0 mg/cm<sup>2</sup> (stacked three layers) showed excellent areal capacity of ~10.8 mAh/cm<sup>2</sup> (~900 mAh/g) even after 50 cycles (Fig. 3 (j)). The incorporation of CNT into electrospun CNF add together peculiarities of both the components into free-standing 3D architecture, i.e., robustness,



electrical conductivity, interfiber macropores for better electrolyte accessibility, and eradication of inactive elements (e.g., binders, conducting additives, Al-foil). These features of CNT/CNF/S cathodes allowed them to show a high areal capacity of  $\sim 10.8$  mAh/cm<sup>2</sup> ( $\sim 900$  mAh/g) at a high sulfur loading of  $\sim 12$  mg/cm<sup>2</sup>. More recently, Zhao *et al.* demonstrated Li-S batteries with an areal capacity of  $\sim 11.3$  mAh/cm<sup>2</sup> using electrospun root-like hierarchically porous carbon nanofibers (HPCNF) based free-standing sulfur cathodes.<sup>111</sup> The free-standing HPCNF mats were fabricated by electrospinning PVP (polyvinylpyrrolidone)/P123 (Pluronic P123)/TEOS (tetraethyl orthosilicate) solution followed by carbonization at 800°C in the inert N<sub>2</sub> environment. The silica template formed *in-situ* (assisted by P123) served as the pore-forming agent and helped HPCNF to exhibit a surface area of  $\sim 1626$  m<sup>2</sup>/g, a pore volume of  $\sim 3$  cm<sup>3</sup>/g and combined micropores (<2 nm) and mesopores (2-50 nm). The HPCNF/S cathodes were prepared with various sulfur loadings (2.2 – 12.1 mg/cm<sup>2</sup>) by combining solution (S/CS<sub>2</sub>) and melt diffusion methods (155°C/12 h). The FESEM image and elemental mapping of HPCNF/S cathode showed that sulfur was infiltrated within root-like hierarchically porous carbon nanofibers (HPCNF) as given in Fig. 3 (k-l). The unique free-standing HPCNF/S cathode material with 12.1 mg/cm<sup>2</sup> sulfur loading exhibited an areal capacity of  $\sim 11.3$  mAh/cm<sup>2</sup> at 0.2 C rate in the first cycle (sulfur utilization >80%) and retained an areal capacity of  $\geq 7.5$  mAh/cm<sup>2</sup> over 50 cycles. Moreover, at 8.3 mg/cm<sup>2</sup> ( $\sim 80$  wt%) sulfur loading, these HPCNF/S cathodes delivered an initial areal capacity of  $\sim 9$  mAh/cm<sup>2</sup> and retained  $\geq 6.0$  mAh/cm<sup>2</sup> after 100 cycles (Fig. 3 (m)). The excellent performance of HPCNF/S cathodes was attributed to the unique root-like porous CNF structures (similar to the vascular structure in plant roots) with central macropores (along with the fiber diameter) surrounded by micro-/mesopores on the periphery. The developed robust free-standing 3D HPCNF architecture enabled better sulfur utilization, provided reservoirs for polysulfides and prevented the structural

collapse during volume changes thus allows Li-S batteries to sustain up to 100 cycles at high sulfur loading.

Additionally, some efforts have been committed to altering sulfur infiltration conditions/methods into free-standing electrospun nanofiber mats aiming at a high gravimetric/areal capacity of Li-S batteries.

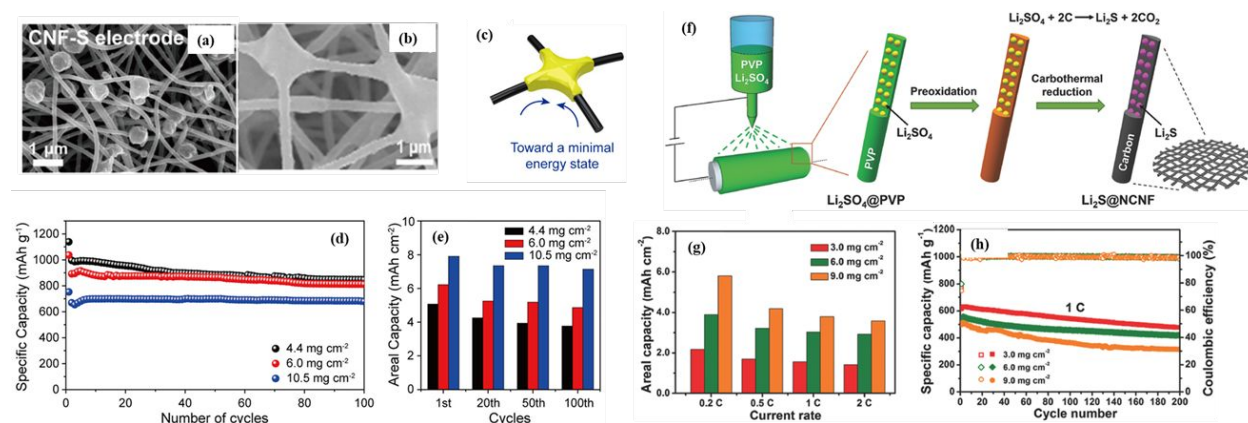


Fig. 4 (a) SEM image of (a) CNF/S cathode and (b) after first charge CNF/S cathode, (c) Schematic of the deposition of sulfur species during the electrochemical reaction via the cohesive force of viscous polysulfides, and (d-e) cycle performance and areal capacity of CNF/S cathodes (0.1 C) with sulfur loadings of 4.4, 6.0, and 10.5 mg/cm<sup>2</sup>, respectively (Reproduced with permission from ref. 108. Copyright 2017 American Chemical Society.); (f) Schematic illustration of the production of freestanding flexible Li<sub>2</sub>S/CNF paper electrodes via Ar-protected carbothermal reduction of Li<sub>2</sub>SO<sub>4</sub>@PVP fabrics made by electrospinning at ambient conditions, (g) cycling performance and Coulombic efficiency of Li<sub>2</sub>S/CNF cathodes with Li<sub>2</sub>S loading of 3.0, 6.0, and 9.0 mg/cm<sup>2</sup> at 1.0 C, and (h) areal specific capacities of Li<sub>2</sub>S/CNF cathodes with various Li<sub>2</sub>S loading at varied current rates of 0.2–2.0 C (Reproduced with permission from ref. 125. 2016 WILEY-VCH Verlag GmbH & Co. KGaA, Weinheim.).

For example, Yun *et al.* demonstrated the high areal capacity of  $\sim 7.9$  mAh/cm<sup>2</sup> in Li-S batteries using PAN-derived electrospun CNF (surface area = 23 m<sup>2</sup>/g) based sulfur cathodes.<sup>108</sup> The CNF/S cathodes were prepared by simply immersing CNF mats directly into a sulfur-containing slurry (Fig. 4 (a)). The slurry was prepared using sublimed sulfur and the MWCNT additive (weight ratio of 95:5) in N-Methyl-2-pyrrolidone (NMP) solvent followed by ultrasonication (2 h) and stirring (2 h) at room temperature. The disk shape punched 12 mm circular CNF electrodes were immersed in the slurry for 10 seconds and dried at 60°C in a vacuum oven for 12 hours. The developed CNF/S cathodes delivered a high areal capacity of  $\sim 7.9$  mAh/cm<sup>2</sup> ( $\sim 752$  mAh/g) at a high sulfur loading of  $\sim 10.5$  mg/cm<sup>2</sup> with  $\sim 90.3\%$  capacity retention ( $\sim 7.14$  mAh/cm<sup>2</sup>) after 100 cycles (Fig. 4 (d-e)). The excellent performance was attributed to solidification of the intermediate polysulfides into Li<sub>2</sub>S in the inter-fiber macropores of CNF matrix with specific wetting angles through cohesive forces as shown in Fig. 4 (b-c).<sup>108</sup> Our group (Dillard *et al.*)<sup>119</sup> recently developed an ultra-rapid technique for sulfur infiltration requiring only 140°C and slight pressure (<250 psi) for 5 seconds to design light-weight free-standing CNFs (or other free-standing 3D substrates) based sulfur cathodes, which is cost-effective and scalable compared to conventional sulfur melt deposition techniques requiring high temperatures (155-300°C), long times (8-10 h), and heavy components (Al-foil) as substrate for slurry-cast process. Chung *et al.* then extended this ultra-rapid technique to achieve 10 mg/cm<sup>2</sup> areal loading and  $\sim 65$  wt% sulfur content in S/CNF (although commercial CNFs).<sup>120</sup> The developed free-standing S/CNF cathodes delivered high gravimetric and areal capacity values of 415–730 mAh/g and 7–12 mAh/cm<sup>2</sup> at low E/S ratio of 6  $\mu$ L/mg and achieved excellent capacity retention rates of over 70% after 200 cycles.

***CNF-based cathodes with Li<sub>2</sub>S as active material:***

The fully lithiated Li<sub>2</sub>S (a sulfur compound) is also a promising alternative cathode material for developing Li-S batteries with high energy density due to its high theoretical gravimetric capacity 1166 mAh/g and ability to pair with safer Li-metal free anodes (e.g., graphite, silicon, tin).<sup>121-124</sup> However, the low electrical conductivity ( $10^{-13}$  S/cm) of Li<sub>2</sub>S necessitates the use of conducting host materials for significantly improving its electrochemical activity.<sup>121-124</sup> Further, the commonly used sulfur melt-infiltration techniques become impractical in case of Li<sub>2</sub>S due to its (a) very high melting temperature (1372°C) in comparison to sulfur (~115°C) and (b) environmental sensitivity of Li<sub>2</sub>S, which makes the cathode preparation more stringent.<sup>125</sup> There are few reports on the development of Li<sub>2</sub>S/carbon cathodes for Li-S batteries using alternative methods such as solution precipitation from organic lithium compounds or ball-milling.<sup>121-124</sup> However, these studies show limited areal capacity (<2 mAh/cm<sup>2</sup>) in Li-S batteries due to low Li<sub>2</sub>S loading (<2 mg/cm<sup>2</sup>).<sup>121-124</sup> Further, these studies use expensive Li<sub>2</sub>S as a raw material/precursor, which increases the overall cost of cathode production. There is surprisingly not much attention paid to the development of Li<sub>2</sub>S based free-standing cathodes. The few papers that exist in the literature focus on the development of free-standing Li<sub>2</sub>S/CNF composite material using electrospinning approach.<sup>125,126</sup> Among these studies, Yu *et al.* demonstrated the most impressive areal/gravimetric capacity of Li-S batteries using electrospun free-standing Li<sub>2</sub>S/CNF composite cathodes.<sup>125</sup> The free-standing Li<sub>2</sub>S/CNF cathodes were developed by electrospinning a blend of highly stable (against moisture and oxygen) inexpensive lithium sulfate (Li<sub>2</sub>SO<sub>4</sub>) and PVP polymer at ambient conditions (Fig. 4 (f)). Here, the carbothermal reaction between Li<sub>2</sub>SO<sub>4</sub> and carbon ( $\text{Li}_2\text{SO}_4 + 2\text{C} \rightarrow \text{Li}_2\text{S} + 2\text{CO}_2$ ) at high annealing temperature (800°C) led to the formation of ultrafine Li<sub>2</sub>S nanoparticles in conducting CNF network. After the simple electrospinning process, the triple-layered Li<sub>2</sub>S/CNF

cathodes with a very high areal loading of  $\text{Li}_2\text{S}$  ( $9.0 \text{ mg/cm}^2$ ) delivered an initial areal capacity of  $4.68 \text{ mAh/cm}^2$  and gravimetric capacity of  $520 \text{ mAh/g}$  with  $\sim 65\%$  retention over 200 cycles (Fig. 4 (g-h)). The excellent performance was attributed to homogeneously dispersed ultrafine  $\text{Li}_2\text{S}$  nanoparticles in mechanically robust conducting interwoven 3D architecture of CNF. Moreover, this simple single-step electrospinning approach greatly reduced the cost for production and processing complexity of  $\text{Li}_2\text{S}$  cathodes.

***CNF-based cathodes with Catholyte as active material:***

Similarly, the use of polysulfides ( $\text{Li}_2\text{S}_k$ ) as the starting active material (known as catholytes) has proven to be a promising approach to increase the areal capacity of Li-S batteries.<sup>127-129</sup> The catholyte provides enhanced  $\text{Li}^+$  transportation and reaction activity over solid state sulfur thus results in better utilization of the active material at high loading.<sup>127</sup> To this end, there are a few approaches in the literature centered on the development of self-standing 3D architecture for catholyte via electrospinning as it can provide 3D long-range conducting channels for electron transfer and voids for high volume catholyte loading.<sup>127,129</sup> For example, Han *et al.* recently demonstrated an outstanding areal capacity of the Li-S pouch cell using electrospun CNF/reduced graphene oxide (rGO) as the conductive frameworks for hosting lithium polysulfide ( $\text{Li}_2\text{S}_6$ ) containing liquid catholyte.<sup>129</sup> The developed CNF/rGO/catholyte electrodes delivered an areal capacity of  $\sim 15.5 \text{ mAh/cm}^2$  corresponding to a sulfur loading of  $\sim 20.3 \text{ mg}_{\text{sulfur}}/\text{cm}^2$  with  $>80\%$  capacity retention over 50 cycles. The synergy between  $\text{Li}^+$  conducting  $\text{Li}_2\text{S}_6$  catholyte and electrically conducting free-standing 3D CNF/rGO architecture led to such excellent performance. The electrolyte to sulfur (E/S) ratio is another critical parameter, which is essential in determining the final energy density of Li-S batteries. It has been realized that even with outstanding gravimetric/areal capacity at satisfactory sulfur loading and utilization, the final energy density of

Li-S batteries cannot outmatch that of commercial LIBs with the use of an excessive amount of electrolyte ( $>4 \mu\text{L}/\text{mg}$ ).<sup>91</sup> To address this issue, Agostini *et al.* recently designed Li-S cells with the high areal capacity of  $\sim 4.8 \text{ mAh}/\text{cm}^2$  ( $\sim 800 \text{ mAh}/\text{g}$ ) at a relatively low E/S ratio of  $\sim 1.66 \mu\text{L}/\text{mg}$  ( $10 \mu\text{L}/\text{cm}^2$ ).<sup>117</sup> In this study, first, self-supporting, binder-free, functionalized CNFs were prepared through electrospinning of a solution containing PAN/PMMA/SiO<sub>2</sub>. The as-spun nanofibers were then stabilized in air at 250°C for 1 h and subsequently, carbonized at 700°C for 3 h under a constant Ar/H<sub>2</sub> (95:5) flow to get CNFs with oxygen functionalities. Then, a solution of 1M Li<sub>2</sub>S<sub>8</sub> in dimethyl ether (DME) was dropped directly on the CNF at 100°C, and DME was allowed to evaporate to get final cathodes with the sulfur loading of  $\sim 6 \text{ mg}/\text{cm}^2$ . In this process, most of the deposited Li<sub>2</sub>S<sub>8</sub> polysulfides were dissolved in the electrolyte and resulted in *in-situ* formation of the catholyte. Part of sulfur species were retained on the CNF as inactive Li<sub>2</sub>S-(S)-O<sub>3</sub> species. The developed CNF/S cathodes displayed an areal capacity starting from  $\sim 5.4 \text{ mAh}/\text{cm}^2$  (900 mAh/g) and stabilizing at  $\sim 4.8 \text{ mAh}/\text{cm}^2$  (800 mAh/g) with no further drop up to 400 cycles (coulombic efficiency 100%). The *in-situ* formed catholyte and polar oxygen functionality of CNF prevented the shuttling of polysulfides to the anode thus making it possible for these Li-S cells to deliver a remarkable performance at a meager E/S ratio.

#### ***Heteroatom doped CNFs as Cathodes:***

Besides tuning the texture properties — porosity and surface area of carbon materials, chemical doping with heteroatoms (e.g., N, O) is also a promising approach for improving their activity in Li-S batteries.<sup>129-137</sup> The heteroatom doping in carbon materials can synchronously ameliorate their electrical conductivity, facilitate ionic transport and provide anchoring sites for strong coupling with intermediate polysulfides (B. E. = 1.3-2.6 eV).<sup>114,134-136,138,139</sup> In this context, Hou *et al.* systematically calculated the interaction energies of various hetero-atoms (B, N, O, F, P, S, Cl)

doped nanocarbon (C) with intermediate lithium polysulfides ( $\text{Li}_2\text{S}_k$ ) using density functional theory (DFT).<sup>140</sup> Based on their DFT calculations, rationales to favor a stiff binding with lithium polysulfides are summarized as follow:

- (1) The dopant should have a lone pair of electrons (Lewis base) to interact with Li (Lewis acid) of polysulfides via electrostatic dipole-dipole interactions.
- (2) The dopant should possess a higher electronegativity than C atom to generate a permanent dipole moment at the local doping site.
- (3) The dopant should have a sufficiently small radius to pair with the Li of polysulfides.
- (4) The dopant should exhibit a stable bonding to the C lattice in order to interact with lithium polysulfides reversibly.

With all these considerations, N has been found to be the most effective dopant for carbon materials in Li-S batteries as evident from the literature.<sup>129-136,139,141-144</sup> Due to its almost similar atomic size and high electronegativity (3.04) than carbon (2.55), it can easily replace C atoms and form bonds with neighboring C atoms.<sup>140</sup> The doped N atom in the C lattice is generally present in three distinctive forms viz., pyrrolic N (rN), pyridinic N (pN) and graphitic (quaternary) N (gN). The *ab initio* calculations establish that rN and pN forms of the doped N atom are more promising than gN for polysulfide trapping.<sup>145</sup> An inclusion of pN or rN atoms in the C lattice not only can improve the electrical conductivity for enhanced sulfur utilization but also can ameliorate the binding ability of carbon materials through  $\text{LiS}_k\text{Li}^+\dots\text{N}$  type interactions for cycling stability.<sup>138,140,145</sup> Besides other N-doped carbonaceous materials such as graphene<sup>146</sup> and hollow carbon nanospheres<sup>133</sup>, N-doped electrospun CNFs have been explored in Li-S batteries. For example, Liang *et al.* recently reported the use of N-doped CNF (NCNF) with 3D interconnected pores as sulfur host in Li-S batteries.<sup>131</sup> N-doped CNFs were prepared by electrospinning a solution

of PVP with varying content (20%, 25%, and 30%) of PTFE (Polytetrafluoroethylene) followed by carbonization at 1000°C in N<sub>2</sub> atmosphere. Here, PVP worked as a source of carbon as well as N doping atoms whereas PTFE served as the sacrificial polymer to generate pores. S-NCNF composites were prepared by grinding NCNF and commercial sulfur together and heating at 300°C in Ar environment. Later, a slurry of S-NCNF in NMP solvent was prepared and coated on the Al-foil to get the final S-NCNF cathodes (~59 wt% sulfur in the final cathode).

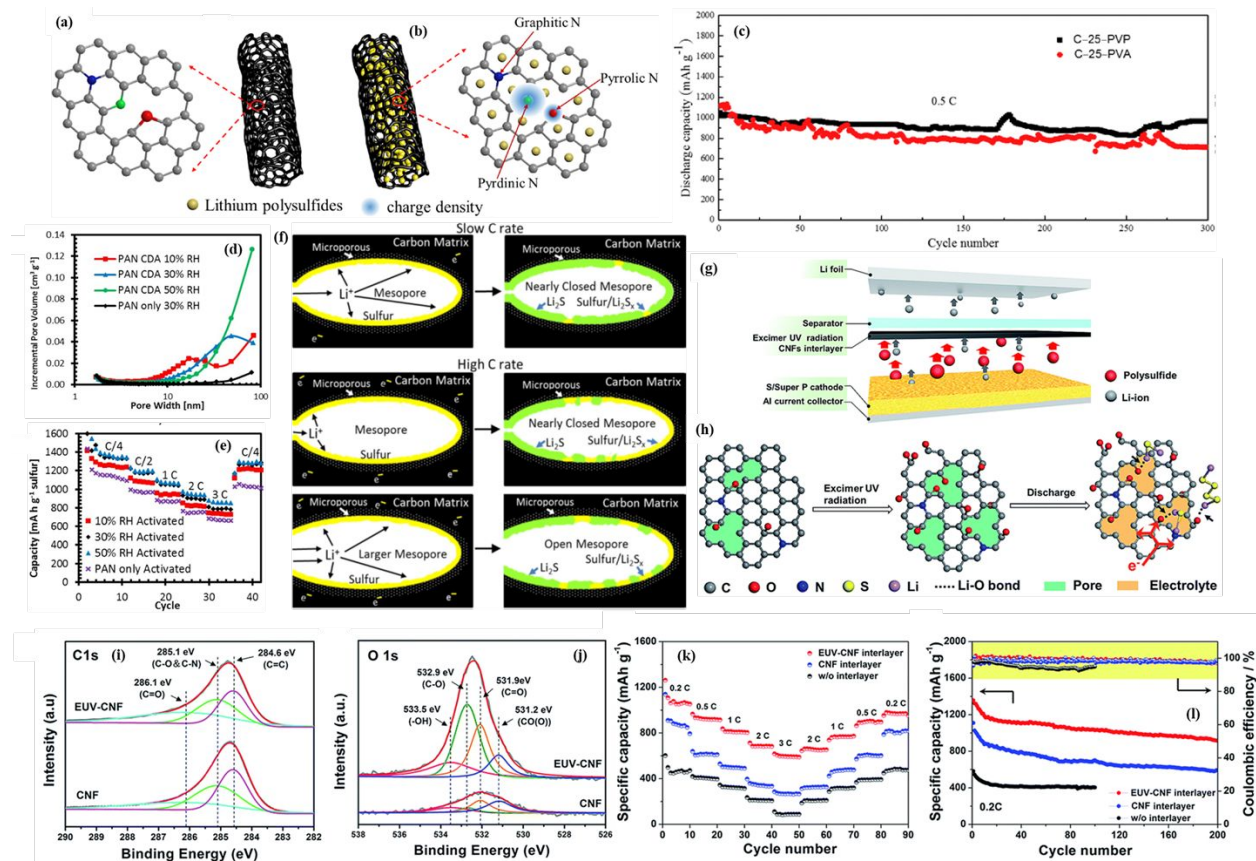


Fig. 5 (a-b) Schematic of the lithium polysulfides adsorption in the N-doped carbon: structure diagrams of NCNFs and the structure diagram for the trapping of lithium polysulfides by NCNFs and charge density of different nitrogen configuration, (c) cycling performance of S-NCNF at a constant rate of 0.5 C (Reproduced with permission from ref. 131. Copyright 2018 Elsevier Ltd.); (d) Incremental pore volume distribution of four carbonized and activated samples initially



electrospun at different relative humidities (RH). The first three samples are 1:1 blends of PAN and CDA and the fourth is PAN only, (e) Rate performance with 10 cycles at 0.25C and 5 cycles at 0.5 C, 1C, 2C, 3C, and 0.25C of cells with 18 mg interlayers of different mesopore and micropore distributions and 1.8 mg sulfur cathodes, and (f) Illustration for the potential effect of the charging rate. At slow charging rates lithium ions can enough time to diffuse throughout the pore before reacting while at higher charging rates, the ion does not diffuse as far, which nearly blocks the pore more quickly before all the sulfur is lithiated. Larger mesopores tend to have larger openings, which prevent diffusion limitations (Reproduced with permission from ref. 150. Copyright 2016 The Electrochemical Society.); (g) Model of the assembled Li–S cell featuring a S cathode, EUV-CNF interlayer, separator, and Li metal. The EUV-CNF interlayer effectively blocks the migration of polysulfides to Li metal during discharge. (h) Element content variation on the CNF surface before and after excimer UV light irradiation and the mechanism of polysulfide adsorption, (i–j) C 1s high-resolution, and O 1s high-resolution XPS spectra of CNF and EUV-CNF interlayers, respectively, (k) Rate performance of batteries with EUV-CNF, CNF, or no interlayer at current rates of 0.2–3C, (l) Charge–discharge capacities and coulombic efficiencies of the Li-S cells at a rate of 0.2C over 200 cycles (Reproduced with permission from ref. 156. Copyright The Royal Society of Chemistry 2018).

The S-NCNF cathodes fabricated from 25% PTFE content showed better performance with a high discharge capacity of ~1094 mAh/g at C/2 rate and ~76% capacity retention after 300 cycles (Fig. 5 (c)). The S-NCNF (25% PTFE) cathodes exhibited suitable 3D interconnected porous channels for accommodation of volume changes, relatively high conductivity than other two NCNF (20% and 30% PTFE) for better sulfur utilization, and significant fraction of rN (25.6%) and pN (15.7%) atoms in the C lattice for trapping polysulfides (A schematic of the lithium

polysulfides adsorption in the N-doped carbon is given in Fig. 5 (a-b)). These features allowed S-NCNF (25% PTFE) to show a high capacity and long-term cycling. Similarly, Gao *et al.* recently designed self-standing N and O dual-doped carbon nanofibers (NOCNF) based on polymer chain design and electrospinning followed by carbonization at 800°C for 1 h in N<sub>2</sub> environment and used them as interlayer in Li-S cells with slurry based cathodes (~4.5 mg/cm<sup>2</sup>, 80 wt% S in the whole cathode).<sup>147</sup> The solution for electrospinning was prepared by dissolving 4,4'-oxydianiline (ODA) and pyromellitic dianhydride (PMDA) into DMF with and without dicyandiamide. Here, dicyandiamide was introduced to substantially improve the N concentration in the polymer chains. The developed slurry-cast sulfur cathode based Li-S cells with NOCNF interlayer delivered a high initial discharge capacity of ~947 mAh/g with ~84% capacity retention after 200 cycles (areal capacity ~3.54 mAh/cm<sup>2</sup>) at 0.1 C rate and excellent rate performance up to 5 C; superior to Li-S cells fabricated with CNF interlayer and no interlayer. Authors showed that dual N and O functionality not only suppressed the shuttle effect with strong polysulfide absorption ability but also improved the sulfur utilization in two step reaction, especially from S<sub>8</sub> to Li<sub>2</sub>S<sub>4</sub> conversion. Very recently, Yao *et al.* developed zeolitic imidazolate framework (ZIF-8) derived nitrogen-doped carbon nanofibers using electrospinning/carbonization process and applied them as the current collector and binder free membrane containing Li<sub>2</sub>S<sub>6</sub> catholyte for lithium-sulfur batteries.<sup>148</sup> The Li-S cells based on free-standing N-CNFs/Li<sub>2</sub>S<sub>6</sub> membrane showed a high first-cycle discharge capacity of ~1175 mAh/g at 0.1 C and excellent rate capability (~702 mAh/g at 1C), more stable electrochemical behavior than the CNFs/Li<sub>2</sub>S<sub>6</sub> membrane. Further, the Li-S cell with N-CNFs/Li<sub>2</sub>S<sub>6</sub> (~3 mg/cm<sup>2</sup> S loading) exhibited an initial discharge capacity of ~677 mAh/g and retained a capacity of ~467 mAh/g after 150 cycles. The superior performance of NCNFs membrane than CNFs membrane was ascribed to synergistic effects of physical (porosity)

and chemical (N-functionality) adsorption of lithium polysulfides and improved electronic conductivity of 3D free-standing NCNFs membranes.

### ***CNFs as Interlayers:***

The use of carbon-based porous interlayers has also been proven to be beneficial for improving the performance of Li-S batteries. An interlayer is an additional freestanding film between the cathode and the conventional separator. Su and Manthiram proposed the concept of the interlayer for the first time by introducing a microporous carbon paper.<sup>149</sup> In this configuration, the C paper (interlayer) serves as an ‘upper current collector’, which improves the electrochemical performance not only by blocking (physical adsorption/van der Waals interactions) the lithium polysulfides but also lengthening their diffusion pathways to the anode. Ever since the introduction of the interlayer concept by Manthiram and co-workers, many research efforts have been aimed at rational designing of interlayers with tunable pore size and surface area for Li-S batteries.<sup>80,146,150-153</sup> Electrospun freestanding nanofiber mats are desirable interlayers as they can be used without additional inactive elements (e.g., binders, conducting additives).<sup>80,150,152,154</sup> In this view, our group (Singhal *et al.*) studied the effects of surface area, pore size, and thickness of the freestanding binder-free electrospun CNF interlayers on the electrochemical performance of conventional sulfur cathode- (60 wt. % and *ca.* 1.45 mg/cm<sup>2</sup>) based Li-S batteries.<sup>152</sup> We prepared three carbonized PAN-derived CNF samples (different in their texture properties) viz., non-porous NCNF, CO<sub>2</sub> activated microporous CNF (ACNF), and micro-mesoporous CNF (MCNF) and used as interlayers. We found that at fast charging/discharging (1C) rate, the ACNF based Li-S batteries showed better capacity retention than the other two (NCNF and MCNF) interlayers. However, at slow (C/5) rate, the capacity retention increased with increasing surface area and pore size (MCNF>ACNF>NCNF). More specifically, the MCNF at C/5 rate delivered a high initial

discharge capacity of  $\sim 1549$  mAh/g and 83.1% capacity retention over 100 cycles. We suggested that mesopores present in the MCNF interlayers facilitate the reactivation of the deposited active materials (S during charge and  $\text{Li}_2\text{S}_2/\text{Li}_2\text{S}$  during discharge) thus resulting in higher capacity retention than other two interlayers at a slow rate. Later, Williams *et al.* systematically investigated the dependence of the rate-performance of conventional S-cathode (slurry) based Li-S batteries on large mesopores in electrospun CNF interlayers.<sup>150</sup> The CNF interlayers with micropores and large mesopores ( $<10$  nm) were produced by electrospinning a blend of two immiscible PAN and cellulose diacetate (CDA; sacrificial component) polymers in DMF solvent followed by carbonization (at  $1000^\circ\text{C}$  for 8 h under  $\text{N}_2$  environment) and activation (at  $350^\circ\text{C}$  in air for 4 h). The average size of the mesopore in CNF interlayers was further adjusted between 17-50 nm by changing the humidity conditions (10%, 30%, and 50% relative humidity (RH)) during the initial electrospinning process as shown in pore size distribution curve in Fig. 5 (d). The change in relative humidity helped control the size of phase-separated domains in the blend before solidification thus helping to adjust the average mesopore size.<sup>150</sup> The reference microporous CNF interlayer was also prepared at 30% RH without the use of sacrificial CDA polymer. Interestingly, the Li-S cell with 50% RH CNF interlayer (largest pores) displayed maximum capacity retention at 1C, 2C, and 3C; approximately 850 mAh/g at 3C from the initial capacity value of  $\sim 1500$  mAh/g at C/4. The Li-S cells with 30% RH interlayer exhibited similar performance to the cell with 50% RH CNF at C/4 and C/2 rate but did not perform well at high rates over 1C (Fig. 5 (e)). Moreover, Li-S cells with 10% RH CNF interlayer and 30% RH reference CNF interlayer (PAN only sample without CDA) showed the lowest capacity retention at high C rates (Fig. 5 (e)). The excellent rate performance of the 30% RH and 50% RH CNF interlayers was attributed to the presence of large mesopores. At high C rates, polysulfides lithiate as soon as the  $\text{Li}^+$  enters the pore, which leads to

pore-narrowing and perhaps pore-blocking. Pore-narrowing (blocking) restricts the lithiation of other polysulfides due to limited diffusion of  $\text{Li}^+$  ions. Authors suggested that the presence of large pores in 30% RH and 50% RH CNF interlayers helped them to maintain the required current at high C-rates by facilitating the diffusion of  $\text{Li}^+$  ions into the pores for polysulfide lithiation. The potential effect of the charging rate on the rate performance is schematically illustrated in Fig. 5 (f). Recently, Lee *et al.* designed highly conducting graphitic carbon fiber felt (GCFF) through graphitization of the electrospun PAN fibers and used it as an interlayer in conventional S-cathode (slurry;  $0.7 \text{ mg/cm}^2 \text{ S}$ ) based Li-S batteries.<sup>155</sup> The GFCC was prepared using three steps: I) stabilization of as-spun PAN nanofibers at  $250^\circ\text{C}$  for 3h in air; II) carbonization at  $1000^\circ\text{C}$  for 3h in Ar environment; and finally, III) annealing at  $2800^\circ\text{C}$  for 2h in Ar environment. The Li-S with GCFF interlayer delivered a high initial discharge capacity of  $\sim 1280 \text{ mAh/g}$  at C/5 rate with  $\sim 78.4\%$  capacity retention over 100 cycles, which was much better than that achieved without a GCFF interlayer (initial capacity  $\sim 785.73 \text{ mAh/g}$ ,  $\sim 43.9\%$  retention over 100 cycles). Moreover, at 1 C rate, the Li-S cell exhibited an initial discharge capacity of  $\sim 1554 \text{ mAh/g}$  with  $\sim 53\%$  capacity retention even after 300 cycles. It was shown that GCFF interlayers improved the reversibility of the reduction/oxidation process due to its highly conducting graphitic structures and decreased the electrode polarization. More recently, Wu *et al.* used an excimer ultraviolet radiation (EUV) source to modify the surface functionality of electrospun CNF interlayer (Fig. 5 (g)).<sup>156</sup> The PAN-carbonized (at  $800^\circ\text{C}$  for 6 h in argon) CNF interlayer was irradiated for 20 minutes (100% power) with UV lamp in the air (oxygen and moisture), which resulted in the formation of functional groups such as -OH and C=O (as shown in C 1s and O 1s XPS spectra in Fig. 5 (h)) as well as nanopores on the surface of CNF. The conventional S-cathode ( $\sim 1.5 \text{ mg/cm}^2 \text{ S}$ ) based Li-S cell with EUV-CNF (oxygenated functionalities) interlayer delivered the highest

capacity of ~1262 mAh/g at C/5 rate, which exceeded that of Li-S cells with CNF interlayer (~1139 mAh/g) and with no interlayer (~603 mAh/g). Further, the Li-S cell with EUV-CNF interlayer exhibited long-term cycling with ~67.6% capacity retention over 200 cycles at C/5 rate (Fig. 5 (l)). Moreover, Li-S cell with EUV-CNF interlayer also showed an improved rate performance than other two Li-S cells with reference CNF interlayer and with no interlayer (Fig. 5 (k)). The excellent performance of Li-S cell with EUV-CNF cell was assigned to physical adsorption (pores) of polysulfides, favorable Li-O interactions with diffusing polysulfides *via* oxygenated surface functionalities (chemical trapping) (Fig. 5 (h)), and improved utilization of the immobilized active material by the conducting CNF interlayer.

To summarize, electrospun CNF structures have played a significant role in the recent advancement of Li-S batteries. The Li-S cells with excellent electrochemical performance have been reported by (a) controlling the pore size, pore volume and surface area of CNF through activation agents (e.g., KOH, CO<sub>2</sub>) and sacrificial templates (e.g., SiO<sub>2</sub>, PMMA), (2) modifying methods of sulfur infiltration into CNF, and (3) using Li<sub>2</sub>S or catholytes as starting materials with CNF. Further, the new Li-S cell configurations with CNF interlayers have also shown significant improvements. However, there is still a lot more room for the improvement in the performance of Li-S batteries with electrospun CNF structures. The performance of Li-S batteries can be improved in future by rationalizing PS-functionality (optimal pores for sulfur loading and utilization, and polysulfide trapping), and e-functionality (conductivity and catalytic activity for reactivation of immobilized active materials) of CNF structures. Moreover, a deeper understanding of how key design parameters (e.g., thickness, pore size, pore shape, pore volume, surface area, surface functionality, heteroatom doping) of electrospun CNF materials affect the overall Li-S battery performance (i.e., areal and gravimetric capacity, cycling, coulombic efficiency, rate capability) is

essential. This understanding can direct researchers toward improving Li-S battery performance and exceeding the ceiling gravimetric and areal capacity of commercial Li-ion batteries. In the following sections, we will now comprehensively review the recent progress made in Li-S batteries using electrospun polymeric and heterostructures.

### 3.1.2 Polymers in Li-S batteries:

#### *Cathodes and Interlayers:*

The recent advancement of Li-S batteries has relied upon the use of various polymeric materials as cathodes, interlayers, and electrolyte membranes.<sup>157-175</sup> In this regard, the simple electrospinning technique allows innovative designing of polymeric structures to address the critical challenges imposed by Li-S chemistry. On the cathode side, the use of electronically conducting polymers such as polypyrrole (PPy) and polyaniline (PANI) with nitrogen functionality offers strong affinity towards lithium polysulfides through chemisorption thus helping in improving the cycle life.<sup>160,167,170,176</sup> For example, Zhu *et al.* recently designed freestanding 3-D CNF/S/PANI composite architecture (schematic is given in Fig 6 (a)) by combining electrospinning technique and an *in-situ* polymerization.<sup>165</sup> First, the freestanding CNF mats were developed by electrospinning a PAN solution followed by stabilization and carbonization at 1000°C for 1 h. Then, S was infiltrated into CNF mats using S/CS<sub>2</sub> solution to ensure homogeneous distribution of S on the surface of CNF and efficient contact between CNF and S in the CNF/S electrodes. Finally, *in-situ* polymerization of PANI was performed directly on the CNF/S structures using aniline monomer, phytic acid, and ammonium persulfate to get final 3D CNF/S/PANI architecture. The TEM image of single CNF/S/PANI and corresponding elemental mappings of C, S, and N elements revealed uniform distribution of S and PANI as shown in Fig. 6 (b). The electrochemical performance was evaluated in an ethereal electrolyte prepared using 1 M

bis(trifluoromethane)sulfonamide lithium (LiTFSI) and 0.1 M lithium nitrate ( $\text{LiNO}_3$ ) in a mixture solvent of 1,2-dimethoxyethane (DME)/1,3-dioxolane (DOL) (1:1 by volume). The conventional slurry based C/S cathode (70 wt% S) and CNF/S cathode ( $1 \text{ mg/cm}^2$  S; ~58 wt% S) exhibited an initial capacity of ~807 mAh/g and ~909 mAh/g, respectively at C/5 rate and maintained only ~44.8% and ~60.7 % of their initial capacity after 300 cycles with a capacity decay rate of ~0.36 and ~0.13% per cycle, respectively. Importantly, the CNF/S/PANI cathode ( $1 \text{ mg/cm}^2$  S; ~52 wt% S) displayed a high initial capacity of ~1278 mAh/g at C/5 rate and retained ~74.6 % of the initial capacity after 300 cycles with a capacity decay rate of ~0.08% per cycle (Fig. 6 (c)). Further, at  $2 \text{ mg/cm}^2$  (~67 wt%) S loading, the CNF/S/PANI cathode showed a capacity of ~711 mAh/g at C/5 rate after 300 cycles (Fig. 6 (d)). The excellent performance of the CNF/S/PANI was attributed to the presence of uniform PANI layer on the CNF/S structures. The conducting PANI layer in the 3D CNF/S/PANI architecture synergistically (a) improved the sulfur utilization, (b) inhibited the shuttling of polysulfides through their chemical trapping with N-rich functionality, (c) helped to accommodate the volume changes and to maintain the structural integrity of the cathode. In another study, Li *et al.* demonstrated an improved electrochemical performance of Li-S batteries using electrospun cyclized-PAN-CNF (CP@CNF) interlayers.<sup>171</sup> In this work, first, freestanding CNF mats were fabricated by electrospinning a PAN solution in DMF solvent. The CNF mats were then immersed in the 5 wt% PAN solution for 30 s and dried at 80°C or 12 h. The CP@CNF interlayers were finally achieved by stabilizing PAN coated CNF mats at 300°C for 10 h in Ar environment. A schematic for the CNF film, the PAN coated CNF film, the intermolecular cyclization reaction, the CP@CNF film and the chemical structures of cyclized-PAN is shown in Fig. 6 (e-i). The electrochemical performance of Li-S batteries (with CNF, CP@CNF interlayers and with no interlayer) was evaluated using conventional slurry based cathodes ( $1.2 \text{ mg/cm}^2$ ; 60 wt% S) in the



etheral electrolyte (1M LiTFSI in DME: DOL (v:v) with 1 wt% LiNO<sub>3</sub>). The Li-S cell with the CP@CNF interlayer delivered a better cycling and rate performance compared to other two Li-S cells with and without CNF interlayers. More specifically, the Li-S cell with CP@CNF interlayer exhibited high reversible capacities of ~910 mAh/g (retention = 85.1%) and ~710 mAh/g (retention = 74.6%) after 100 and 200 cycles, respectively at 0.3C rate with a high coulombic efficiency of ~99.5% (Fig. 6 (k)). In the CP@PAN interlayer structure, the conducting CNF skeleton serves as an upper current collector and enables better sulfur utilization. Using postmortem FTIR, XPS (N 1s XPS spectra is shown Fig. 6 (j)) and TEM studies, it was shown that the cyclic-PAN layer with abundant polar C=N (i.e., pN (pyridinic)) groups (than CNF interlayer alone) minimizes the shuttle effect through both physical (similar to CNF interlayer) and chemical trapping (chemisorption through p-electrons on pN) of polysulfides.

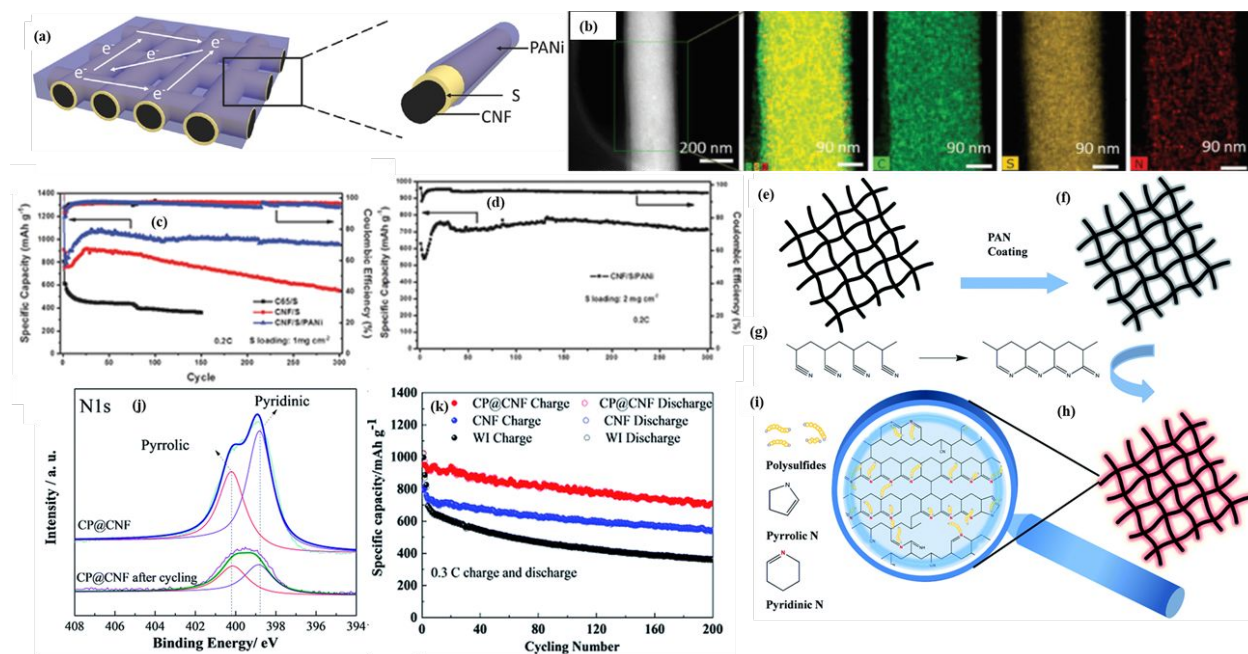


Fig. 6 (a) Schematic illustration of the CNF/S/PANI electrode configuration, (b) STEM image of single CNF/S/PANI and corresponding elemental mappings of C, S, and N elements revealing

uniform distribution of S and PANi, (c) Cycling performance of CNF/S/PANi electrode at higher current densities of 0.5 and 1 C (S loading: 1 mg/cm<sup>2</sup>), and (d) Cycling performance of CNF/S/PANi electrode (S loading: 2 mg/cm<sup>2</sup>) (Reproduced with permission from ref. 165. Copyright 2018 WILEY-VCH Verlag GmbH & Co. KGaA, Weinheim.); (e-i) Schematic of the CNF film, the PAN coated CNF film, the intermolecular cyclization reaction, the CP@CNF film and the chemical structures of cyclized-PAN, respectively, (j) XPS spectra of CP@CNF interlayers after cycling, and (k) Cycling performances of Li-S cells with CNF, without CNF (WI) and CP@CNF interlayers at 0.3 C rate (Reproduced with permission from ref. 171. Copyright 2016 The Royal Society of Chemistry.)

### ***Electrolyte membranes***

Recently, Shanthi *et al.*, for the first time, developed nanofiller incorporated freestanding poly(vinylidene fluoride-co-hexafluoropropylene) (PVdF-HFP) membranes and used them as a host matrix for the preparation of gel polymer electrolytes (GPEs)— a liquid electrolyte incorporated into polymer matrix.<sup>157</sup> In particular, they used commercial fumed f-SiO<sub>2</sub>, and sol-gel derived nm-TiO<sub>2</sub> and nm-SiO<sub>2</sub> nanoparticulates as the nanofillers. The use of GPE in Li-S batteries as electrolyte-separator assembly brings about several unique advantages over its liquid counterpart such as minimal electrolyte leakage, no internal short-circuiting, and reduced polysulfide dissolution and shuttle.<sup>177,178</sup> GPEs with electrospun porous and fibrous polymeric membranes have been shown to be more efficient in rechargeable batteries than fibrous membranes developed from melt or solution spinning due to their superior structural/mechanical stability and ionic conductivity.<sup>157,179,180</sup> Further, the use of oxide nanofillers in GPE membranes has been shown to augment the ionic conductivity and mechanical properties of GPE films.<sup>177,178</sup> Therefore, Shanthi *et al.*<sup>157</sup> first prepared PVDF-HFP-oxide/nanofiller membranes by electrospinning a

solution of PVDF-HFP (10 wt%), LiTFSI (0.1 wt%), and nanofiller (nm-SiO<sub>2</sub>/nm-TiO<sub>2</sub>/f-SiO<sub>2</sub>; 0.1 wt%) in a mixed solvent of acetone/DMF (3:7; w/w) followed by drying under vacuum at 60°C for 12 h. The final GPEs were obtained by first heat pressing these membranes at 80°C for 30 min at 1 atm pressure and then soaking them in an ethereal electrolyte (1.8 M LiTFSI and 0.1 M LiNO<sub>3</sub> in DME/DOL (1:1; v:v)) for 30 min. The SEM image of electrospun PVdF-HFP polymer membranes with dissolved LiTFSI (10 wt %) and dispersed f-SiO<sub>2</sub> (10 wt %) is shown in Fig. 7 (a). These GPEs were tested with commercial S-powder based cathodes in Li-S batteries. Control Li-S cells were also examined under identical conditions replacing the GPEs with liquid electrolyte and commercial polypropylene (Celgard 2400; PP) membrane separator.

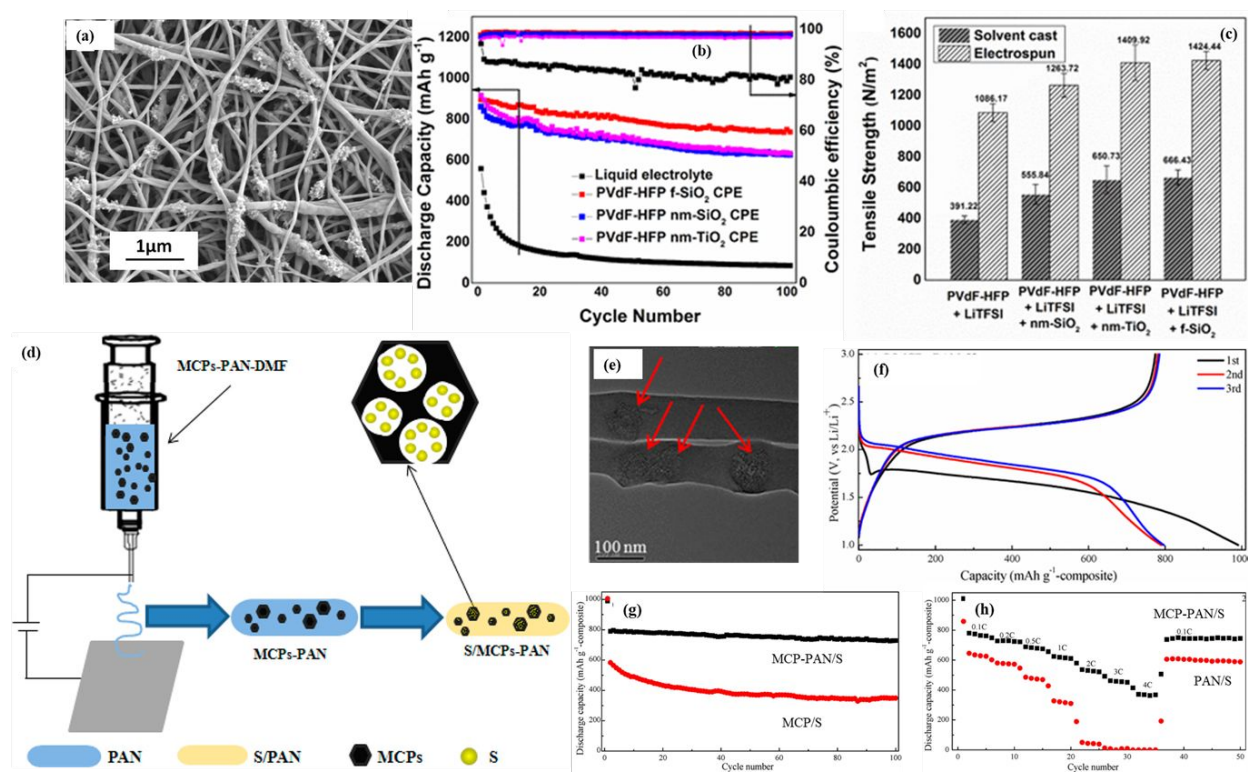


Fig. 7 (a) SEM images of electrospun PVdF-HFP polymer membranes with dissolved LiTFSI (10 wt %) and dispersed f-SiO<sub>2</sub> (10 wt %), (b) cycle performance and Coulombic efficiencies of Li-S cells with different polymer membranes, and (c) Comparison of tensile strengths of various

electrospun and solvent cast membranes. Each datum represents an average of three independent tests run on three different samples under identical conditions. (Reproduced with permission from ref. 157. Copyright 2018 American Chemical Society.); (d) Illustration of the Preparation Process for MCPs-PAN/S Multi-Composites, (e) TEM image of MCPs-PAN nanofibers with MOF-derived MCPs indicated by red arrows, (f) Initial three charge–discharge curves of MCPs-PAN/S cathodes (52 wt% S), (g) Cycle performances of MCPs/S and MCPs-PAN/S (52 wt% S) at a current density of 160 mA/g<sub>sulfur</sub>, and (h) high rate-performance of MCPs-PAN/S (52 wt% S) and PAN/S composites (Reproduced with permission from ref. 189. Copyright 2017 American Chemical Society.)

The electrochemical results showed that optimum GPE (E/S = 3-4 mL/g) based on PVDF-HFP/f-SiO<sub>2</sub> exhibits stable cycling performance over 100 cycles (fade rate ~0.056% per cycle) in Li-S batteries with an initial specific capacity of 895 mAh/g at 0.1 C-rate (Fig. 7 (b)). In contrast, Li-S cells with commercial separator and liquid electrolyte displayed a low initial capacity of ~557 mAh/g that decreased to 132 mAh/g within 10 cycles, despite a high E/S ratio of 50-65 mL/g. The GPEs based on PVDF-HFP/f-SiO<sub>2</sub> serve as electrolyte-separator assembly in Li-S cells and have superior mechanical stability (Fig. 7 (c)) due to interconnected PVDF-HPF nanofibers, high lithium ion conductivity (comparable to liquid electrolyte), and higher liquid electrolyte uptake (>250%) with structural stability. Further, these membranes exhibit higher electrochemical stability and a lower interfacial resistance. Moreover, the GPE membranes help to reduce polysulfide dissolution and shuttle due to small pore size (~15 nm) than commercial separator (~25 nm). These attractive attributes of GPEs allowed Li-S cells to show superior performance. This recent work could motivate researchers to explore electrospun-membrane based GPEs in Li-S batteries at low E/S ratios.

***Sulfurized PAN (SPAN) in carbonate electrolytes:***

Polymers have also played a significant role in enabling the use of commercially-viable carbonate electrolytes for Li-S batteries.<sup>181-183</sup> From the perspective of capacity, the high solubility of intermediate lithium polysulfides in ethereal electrolytes is essential as it enables better sulfur utilization and complete reduction of S to  $\text{Li}_2\text{S}$ .<sup>166,181-183</sup> However, in most instances, the severe internal shuttle effect and Li-corrosion in ethereal electrolytes ultimately lead to low coulombic efficiency and short cycle life of Li-S batteries.<sup>184</sup> Further, the low boiling point of commonly used ethereal electrolytes (e.g., 75°C for DOL)<sup>184</sup> and oxidizing nature of  $\text{LiNO}_3$  additive<sup>185</sup> (commonly used in ether electrolytes for stable SEI formation on the Li-anode) impose serious safety challenges for the operation of Li-S batteries at elevated temperatures.<sup>181-183</sup> On the other hand, the traditional carbonate-based electrolytes (e.g., 1M  $\text{LiPF}_6$  in ethylene carbonate (EC) and diethyl carbonate (DEC) (v:v; 1:1)) are cost-effective and have higher boiling point (e.g., 243°C for EC and 242°C for PC), and very low solubility of polysulfides.<sup>181-184,186,187</sup> Nonetheless, the use of carbonate electrolytes is only possible under certain conditions due to the formation of thioether and methylated thiolate during discharge through a chemical reaction between nucleophilic polysulfides ( $\text{S}_k^{2-}$ ) and carbonates.<sup>183,187</sup> In this regard, two feasible solutions have been proposed: confining sulfur (short chains of sulfur;  $\text{S}_{2-4}$ ) in microporous carbon (pore diameter <0.7 nm)<sup>188</sup> and using sulfurized polymers.<sup>168</sup> The short chains of sulfur confined in micropores or covalently bonded S in sulfurized polymers have been shown to give rise to a single plateau in the discharge cycle, which corresponds to a direct conversion of sulfur to  $\text{Li}_2\text{S}$ .<sup>171,188</sup> However, the confinement of S in micropores generally requires a complex multistep process and precise control of pore size in carbon using activation agents. The approach involving sulfurization of polymer is relatively simple.<sup>188</sup> Among the sulfurized polymers, sulfurized PAN (SPAN) has received significant

attention as a high-performance cathode material due to covalently bonded sulfur and nitrile groups of PAN.<sup>160,166,171</sup> The interaction of the nitrile group of PAN with Li<sub>2</sub>S through coordination bonding allows uniform distribution of Li<sub>2</sub>S.<sup>160,166,171</sup> Interestingly, Zhang *et al.* developed a novel structure of SPAN using electrospinning, which brings two approaches together- the confined short chains of sulfur and covalently bonded sulfur into a single material.<sup>189</sup> First, the synthesized Zeolitic imidazolate framework (ZIF-8) was carbonized at 900°C for 6 h under Ar flow to get microporous carbon polyhedrons (MCPs). Then, MCP encapsulated PAN nanofibers were developed by electrospinning PAN/MCP blend in DMF (TEM is given Fig. 7 (e)). The PAN/S (without MCP as control) and MCP-PAN/S (52 wt% S) composites were developed by first heating the fiber with sulfur at 155°C for 3 h and then heating at 300°C for 4 h under Ar flow. The preparation process for MCP-PAN/S multi-composites is summarized in Fig. 7 (d). The final cathodes were prepared by casting a slurry of active material on Al foil with sulfur loading of ~1 mg/cm<sup>2</sup>. The electrochemical performance was evaluated using 1.0 M LiPF<sub>6</sub> in mixed solvents of PC/EC/DEC (1:4:5 by volume; DEC: Diethyl carbonate) as electrolyte. It is noteworthy that MCP-PAN/S cathodes showed charge-discharge curves with a single plateau (except the first cycle); typically reported for S/microporous carbon or SPAN in carbonate electrolytes (Fig. 7 (f)). Moreover, the MCP-PAN/S cathode delivered superior electrochemical performance including a large reversible capacity of ~790 mAh/g<sub>composite</sub> (~1519 mAh/g<sub>sulfur</sub>) in the second cycle with ~84.4% capacity retention over 200 cycles (Fig. 7 (g)), high S-utilization (~90.7%), large initial coulombic efficiency (~78.2%), and high rate capability up to 4C rate (Fig. 7 (h)). The electrochemical results indicate that the presence of MCP in the MCP-PAN/S synergistically overcomes disadvantages (initial poor coulombic efficiency, low sulfur content and utilization, and poor rate capability) of individual components viz., MCP/S (confined sulfur) and SPAN

(sulfurized polymer) in carbonate electrolytes. While MCPs enable a sufficient sulfur loading, PAN nanofibers provide structural stability and offer 3D channels for easy ionic and electronic transport. Furthermore, S-contained PAN acts as a buffer layer, which significantly improved the initial coulombic efficiency by preventing the penetration of carbonate solvents without compromising ionic and electronic transport.

In summary, electrospun structures of polymers have shown great potential for the advancement of Li-S batteries in the recent past. In particular, the use of GPEs from electrospun polymeric membranes seems to be a foreseeable solution to the ill-famed shuttle effect. The future research efforts should aim at the development of electrospun GPE based Li-S cells under more realistic conditions in order to examine the viability of this approach. Similarly, sulfurized polymers are also promising cathode materials for Li-S batteries. However, low sulfur content (electrochemically analogous to  $S_8$ ), poor initial coulombic efficiency, and unsatisfactory rate performance of these sulfurized polymers are long-lasting limitations. More research efforts are required to rationally design the electrospun structures of sulfurized polymers in order to improve their performance further. At the same time, a better understanding of the role of electrochemically inert polymer chains would help to impart desirable properties to the sulfurized polymeric materials.

### **3.1.3. Electrospun heterostructures for Li-S batteries:**

#### ***Metal oxide based heterostructures:***

As discussed above, the electrospun CNF with complex micro-mesoporosity and 3D interconnected channels for electrons and ions are capable of accommodating sulfur and physically blocking the diffusion of intermediate lithium polysulfides towards Li-anode. The introduction of heteroatoms into the conjugate nonpolar carbon planes can further enhance the functionality of

CNFs, wherein doped-heteroatom sites can potentially anchor polysulfides through polar-polar and dipole-dipole interactions. Nanostructured polar inorganic compounds (e.g., oxides, carbides) are another class of materials, which exhibit high binding energy with polysulfides.<sup>190-197</sup> These inorganic compounds strongly bind intermediate lithium polysulfides (B. E. = 2.6-7.0 eV) through polar-polar, Lewis acid-base or thiosulfate-polythionate conversion type interactions and can enable high capacity and long cycle life in Li-S cells.<sup>113,114,195-198</sup> However, the poor electrical conductivity of these organic compounds (e.g.,  $5 \times 10^{-30}$  S/cm for vacancy free lattice of TiO<sub>2</sub>) necessitates a rational design of their composites with conducting agents (e.g., carbon).<sup>195</sup> In this context, electrospinning of hybrid organic/inorganic gel is the most straightforward approach, which simplifies the fabrication process of 3D CNF/inorganic heterostructures and allows direct anchoring of the inorganic component to CNF.<sup>190,199-201</sup> In the recent past, various electrospun CNF/inorganic heterostructures have been explored as sulfur hosts, interlayers and Li-protecting layers in Li-S batteries.<sup>190,199,200,202,203</sup> For example, Song *et al.* designed a 3D flexible CNF/graphene architecture decorated with ultrafine TiO<sub>2</sub> nanoparticles (C/G/TiO<sub>2</sub>) using the electrospinning technique and employed it as a sulfur host in Li-S batteries.<sup>204</sup> The free-standing C/G/TiO<sub>2</sub> electrodes were prepared by electrospinning a solution of PAN/graphene oxide/TEOS/titanium isopropoxide (TIP) in DMF. The as-electrospun nanofibers were stabilized at 250°C in air for 5 h and carbonized at 1000°C for 2 h under Ar/H<sub>2</sub> flow. The final free-standing C/G/TiO<sub>2</sub>-S cathodes (1.2 mg/cm<sup>2</sup>, 55wt% S in the cathode) were developed by soaking the carbonized mats in S/CS<sub>2</sub> solution for 10 minutes and drying in air at 60°C for 4 h. A schematic illustration of the fabrication process for the C/G/TiO<sub>2</sub>-S composite is given in Fig. 8 (a). The SEM image (Fig. 8 (b)) of the C/G/TiO<sub>2</sub>-S composite showed that no bulk sulfur particles were found on the surface of the C/G/TiO<sub>2</sub>-S, showing a homogeneous distribution of S inside the CNF framework. The



HRTEM image with lattice fringes and selected area diffraction (SAED) pattern (Fig. 8 (c)) of the C/G/TiO<sub>2</sub>-S further demonstrated that the rutile type polycrystalline TiO<sub>2</sub> nanocrystals (circled with white dotted lines) were present with an average size of 5 nm.

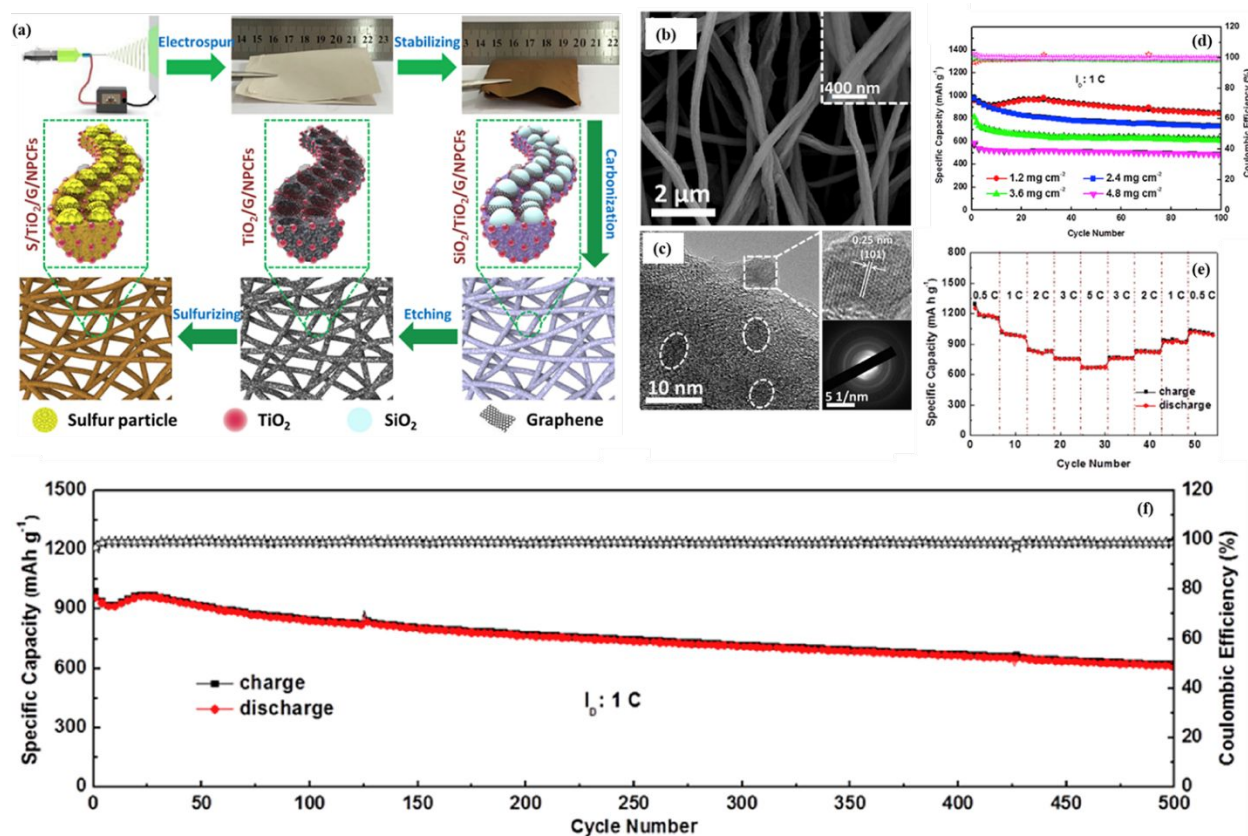


Fig. 8 (a) Schematic illustration of the fabrication process for the C/G/TiO<sub>2</sub>-S composite, (b) SEM image for the C/G/TiO<sub>2</sub>-S composite, (c) HRTEM and SAED images for the C/G/TiO<sub>2</sub>-S composite. TiO<sub>2</sub> nanocrystals (circled with white dotted lines) have an average size of 5 nm. The lattice fringes enlarged from the HRTEM image and the corresponding SAED pattern shows that the phase of the nanoparticles is rutile TiO<sub>2</sub> with a polycrystalline structure. (d) Cycling performance of C/G/TiO<sub>2</sub>-S electrode with different sulfur content at the current rate of 1 C, (e) Rate capability of C/G/TiO<sub>2</sub>-S electrode recorded at the current rates of 0.5 C, 1 C, 2 C, 3 C, and

5 C, and (f) Long-term cycling performance of C/G/TiO<sub>2</sub>-S electrode at 1 C (Reproduced with permission from ref. 204. Copyright 2017 Elsevier B.V.)

The developed C/G/TiO<sub>2</sub>-S cathodes delivered an initial capacity (1501 mAh/g at C/10), excellent rate performance (668 mAh/g at 5C as shown in Fig. 8 (e)) and long cycling stability (987 mAh/g at 1C with 62.6 % retention after 500 cycles as shown in Fig. 8 (f)). Moreover, the C/G/TiO<sub>2</sub>-S cathodes with areal sulfur loading of 2.4, 3.6, and 4.8 mg/cm<sup>2</sup> exhibited initial capacities of 967, 890, and 814 mAh/g at 1 C rate, and capacity retentions of 76, 69, and 60% after 100 cycles, respectively (Fig. 8 (d)). The excellent electrochemical performance of C/G/TiO<sub>2</sub>-S cathodes was attributed to (a) induced micro-mesoporosity (by sacrificial TEOS) and flexibility (by graphene) for accommodating the volume changes, (b) inherent 3D channels for facile transport of electrons and ions, and (c) strong affinity of polar TiO<sub>2</sub> with polysulfide anions via hydrophilic Ti-O groups and surface hydroxyl groups (B. E. = 2.1-3.6 eV).

Nazar *et al.* proposed that the nature of interactions between polysulfide anions and metal oxides is strongly governed by their redox potential vs. Li/Li<sup>+</sup>.<sup>198</sup> Metal oxides (e.g., TiO<sub>2</sub>; 1.5 V vs Li/Li<sup>+</sup>) with redox potential <2 V (below the polysulfide window of 2.1 V ≤ redox potential ≤ 2.4 V) bind polysulfides through surface interactions. In contrast, metal oxides (e.g., V<sub>2</sub>O<sub>5</sub> = 3.4 V and MnO<sub>2</sub> = 3.05 V vs. Li/Li<sup>+</sup>; redox mediators) with redox potential >3 V (above the polysulfide window of 2.1 V ≤ redox potential ≤ 2.4 V) can oxidize the polysulfides to thiosulfate (S<sub>2</sub>O<sub>3</sub><sup>2-</sup>) or sulfate. The *in-situ* formed thiosulfate species, i.e., [O<sub>3</sub>S-S]<sup>2-</sup> can potentially anchor higher order polysulfides by creating intermediate polythionate complex [O<sub>3</sub>S-S—S<sub>k-2</sub>—S-SO<sub>3</sub>; k ≥ 4] and simultaneously induce the formation of insoluble lower order sulfides (S<sup>2-</sup>). Inspired by this work, Liu *et al.* demonstrated the prolonged cycle life of Li-S cells using novel V<sub>2</sub>O<sub>5</sub>-decorated CNF (VCNF) as the interlayer.<sup>199</sup> The VCNF interlayer was developed by growing V<sub>2</sub>O<sub>5</sub>

nanoflakes on the electrospun CNF (made using PAN/DMF solution) with the solvothermal method. The FESEM image (Fig. 9 (a)) of VCNF showed that that 50 nm thick layer of  $V_2O_5$  uniformly wrapped each individual CNF. The TEM image in Fig. 9 (d) further revealed a 1D  $V_2O_5$  architecture with crystalline flaky morphology homogenously distributed on every single nanofiber. The sulfur cathodes ( $S = 2 \text{ mg/cm}^2$ ) were prepared by coating a carbon-sulfur slurry (70% S, 20% super P, 10% PVDF in NMP) on the carbon-coated Al-foil and drying at  $60^\circ\text{C}$  for 24 h. Impressively, Li-S cells with VCNF interlayer showed a high discharge capacity of 576 mAh/g at 3C rate after 1000 cycles with  $\sim 70.6\%$  retention (fading rate = 0.03% per cycle) of the initial capacity (Fig. 9 (c)). In comparison, Li-S cells with bare CNF interlayer delivered a low discharge capacity of 265 mAh/g after 1000 cycles with  $\sim 33.6\%$  retention (fading rate = 0.06% per cycle) of the initial capacity. Further, Li-S cells with VCNF interlayer exhibited excellent rate performance (up to 5C) (Fig. 9 (d)) and suppressed self-discharge (Fig. 9 (e-f)). The superior electrochemical performance of Li-S cells (with VCNF interlayer) was assigned to (a) the  $V_2O_5$  in the VCNF interlayer with a strong affinity towards polysulfides (e.g., 3.73 eV for  $V_2O_5\text{-Li}_2\text{S}_4$  interactions)<sup>205</sup> as well as redox-mediator function (high redox potential), (b) robust 3D conducting VCNF architecture for re-utilization of the active material and (c) inherent interfiber macropores/voids for facile ion transfer.

Similarly, Liu *et al.* developed CNF/birnessite- $\text{MnO}_2$  (CNF/ $\text{MnO}_2$ ) composite electrodes using electrospinning and used it as a sulfur host in Li-S battery.<sup>201</sup> A schematic illustration of the Li-S battery with a sulfur cathode covered with the CNFs/ $\text{MnO}_2$  composite is shown in Fig. 9 (g). The CNF/ $\text{MnO}_2$  electrodes were prepared by soaking CNFs (carbonized PAN nanofibers) in aqueous  $\text{KMnO}_4$  solution at room temperature for 48 h and then drying at  $60^\circ\text{C}$  under vacuum. Here, the room temperature growth of  $\text{MnO}_2$  was governed by the redox reaction between  $\text{MnO}_4^-$

and C ( $4\text{MnO}_4^- + 3\text{C} + 4\text{H}^+ \rightarrow 4\text{MnO}_2 + 3\text{CO}_2 + 2\text{H}_2\text{O}$ ). The TEM image in Fig. 9 (h) exhibited that the dense  $\text{MnO}_2$  nanosheets radially grown on the surface of CNF to a thickness about 100 nm. The CNF/ $\text{MnO}_2$ -S cathodes were prepared using commercial sublimated sulfur and cast on Al-foil. The Li-S cell with CNF/ $\text{MnO}_2$ -S cathode ( $1.5 \text{ mg/cm}^2 \text{ S}$ ) delivered a high initial capacity of  $\sim 788 \text{ mAh/g}$  at 1C (coulombic efficiency  $\geq 99\%$ ) with  $\sim 75\%$  retention after 400 cycles exhibiting a slow decay rate of 0.063% per cycle (Fig. 9 (j)).

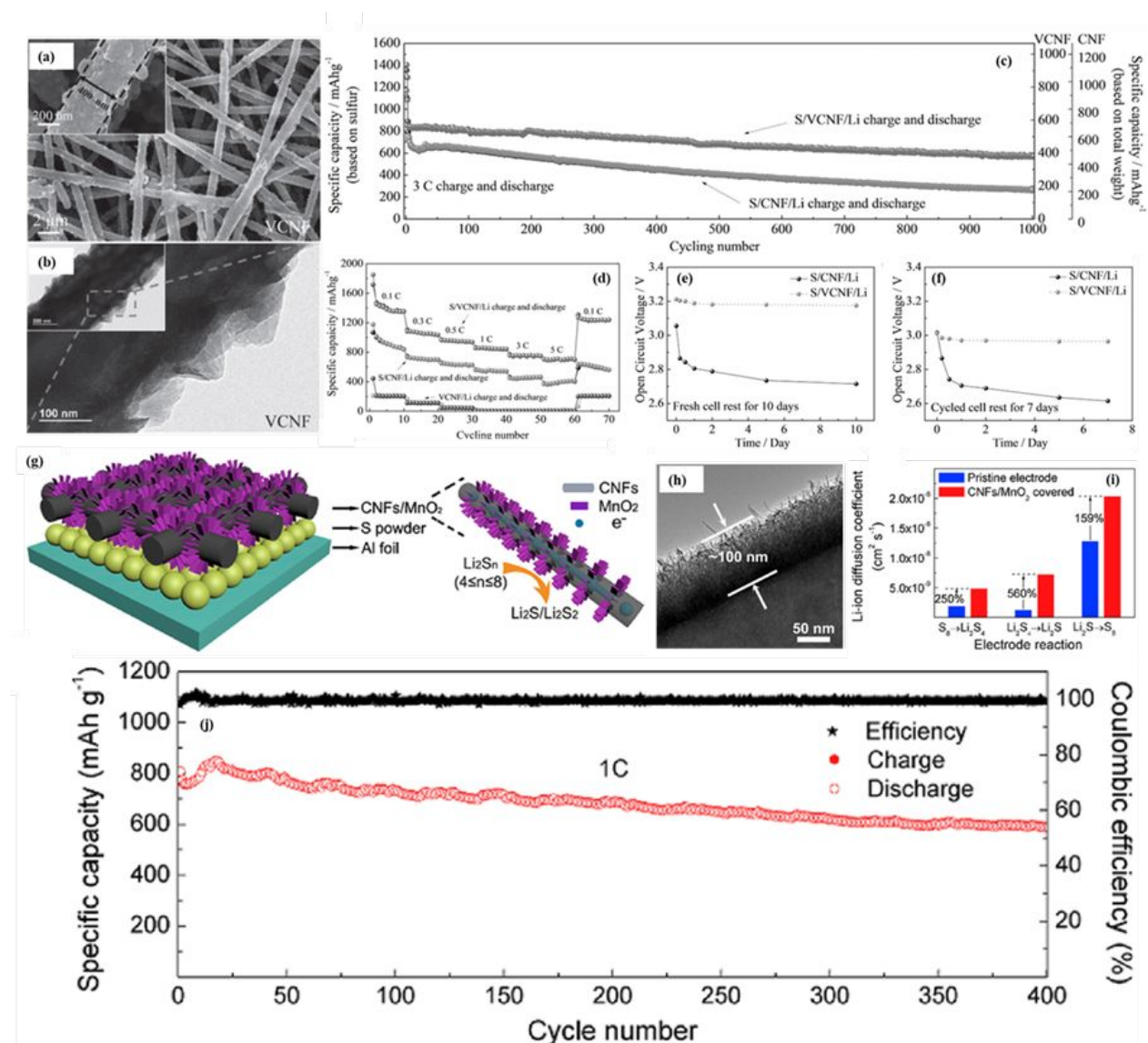


Fig. 9 (a) FESEM image of VCNFs (the high-resolution image is shown in inset), (b) HRTEM image of VCNF (high-resolution image is shown in inset), (c) Long term cycling performance of

S/CNF/Li (bare CNF interlayer) and S/VCNF/Li (VCNF interlayer) cells at 3 C, (d) Rate performances of S/CNF/Li, S/VCNF/Li, and VCNF/Li (without S cathode) cells from 0.1 to 5 C, (e) The open-circuit voltage of S/CNF/Li and S/VCNF/Li fresh cells during original storage. The initial OCV of S/VCNF/Li fresh cell (3.22 V) is higher than that of S/CNF/Li one (3.06 V), and maintains rather stable in the following 10 days with a final cut-off voltage of 3.18 V. The highly stable OCV for S/VCNF/Li fresh cell is associated with the formation and immobilization of polysulfides in cathode. (f) The open-circuit voltage of S/CNF/Li and S/VCNF/Li cycled cells during interrupt storage. S/CNF/Li and S/VCNF/Li cells were charged back to 3.0 V after 100 cycles and stored for seven days and again cycled. During the whole interrupt rest for S/VCNF/Li, OCV values are above 2.96 V, which is similar to the fresh cell thus corroborating a suppressed self-discharge due to VCNF interlayer. (Reproduced with permission from ref. 199. Copyright 2017 Elsevier B.V.); (g) Schematic illustration of the Li-S battery with a sulfur cathode covered with the CNFs/MnO<sub>2</sub> composite, (h) TEM image of the CNFs/MnO<sub>2</sub> composite. The dense MnO<sub>2</sub> nanosheets were radially grown on the surface of CNF to a thickness about 100 nm. (i) Calculated diffusion coefficient of lithium ion for the CNFs/MnO<sub>2</sub> composite covered S-electrode and the pristine S-electrode, and (j) Long-term cycling performance and the coulombic efficiency at a current density of 1C for the CNFs/MnO<sub>2</sub> composite covered S-electrode (Reproduced with permission from ref. 201. Copyright 2018 Elsevier Ltd.).

In this composite, nano-textured MnO<sub>2</sub> anchored on CNF was shown to improve the kinetics for the conversion of soluble Li<sub>2</sub>S<sub>4</sub> to insoluble Li<sub>2</sub>S<sub>2</sub>/Li<sub>2</sub>S. More specifically, the diffusion coefficient of Li<sup>+</sup> for the CNF/MnO<sub>2</sub> cathode during Li<sub>2</sub>S<sub>4</sub>→Li<sub>2</sub>S conversion was greatly enhanced (~560%) compared to that for the pristine cathode (without CNF/MnO<sub>2</sub>) (Fig. 9 (i)). Therefore, MnO<sub>2</sub> component in the composite cathode serves as a bi-functional agent, which not only entraps

polysulfides within the cathode through polythionate complex formation but also promotes reduction kinetics.

***Non-stoichiometric metal oxide based heterostructures:***

Recently, reduced forms of  $\text{TiO}_2$  such as titanium suboxides (e.g.,  $\text{Ti}_4\text{O}_7$  with two  $\text{Ti}^{4+}$  ( $3d^0$ ) and two  $\text{Ti}^{3+}$  ( $3d^1$ )), and titanium monoxide ( $\text{TiO}$  with  $\text{Ti}^{2+}$  ( $3d^2$ )) have been employed as sulfur hosts and interlayers in Li-S batteries.<sup>206-209</sup> The use of such bifunctional oxides in Li-S batteries brings two main advantages: i) substantial improvement in the electrical and ionic conductivity due to oxygen vacancies in the Ti- and O-sublattices and ii) strong binding of polysulfide anions ( $\text{S}_k^{2-}$ ; Lewis base) with unsaturated Ti-centers (vacant d-orbital; Lewis acid) through Lewis acid-base (i.e., covalent coordination) type interactions (B. E.  $\geq 3.5$  eV).<sup>114,207,210</sup> Nevertheless, the preparation of these Ti-oxides (via carbothermal reaction or reducing  $\text{H}_2$  gas) requires a high temperature (usually  $>800^\circ\text{C}$ ) treatment; resulting in highly dense materials (low surface area) with irregular particulates.<sup>211</sup> Consequently, these dense Ti-oxides show a compromised performance in Li-S battery due to reduced host-polysulfide interfacial (interaction) area. There are few reports on the development of sophisticated architectures (e.g., hollow  $\text{TiO}/\text{C}$  microsphere) of these Ti-oxides with the high surface area.<sup>207,208</sup> However, the complicated synthesis route adopted to design such novel architectures is impractical on a large scale. Further, these powder based Ti-oxides are used in a slurry form with additional inactive elements (binders and conducting additives), which results in low sulfur loading in the final cathode.<sup>207-209</sup> In this view, the combination of electrospinning and carbothermal process provides a simple, cost-effective approach for the development of free-standing Ti-oxide electrodes without the need of complicated synthesis route. For example, Tang *et al.* recently developed carbon/ $\text{Ti}_4\text{O}_7$  non-woven fabric through electrospinning and used as a multifunctional interlayer in Li-S battery.<sup>212</sup> The free-



standing  $C/Ti_4O_7$  mat was prepared by electrospinning a solution of PVP/TIP in ethyl alcohol and calcining at  $1100^\circ\text{C}$  under steady  $N_2$  flow. The TEM image of  $C/Ti_4O_7$  showed that  $Ti_4O_7$  nanoparticles were tightly surrounded with a thin layer of carbon in a bamboo-like shape as given in Fig. 10 (a).

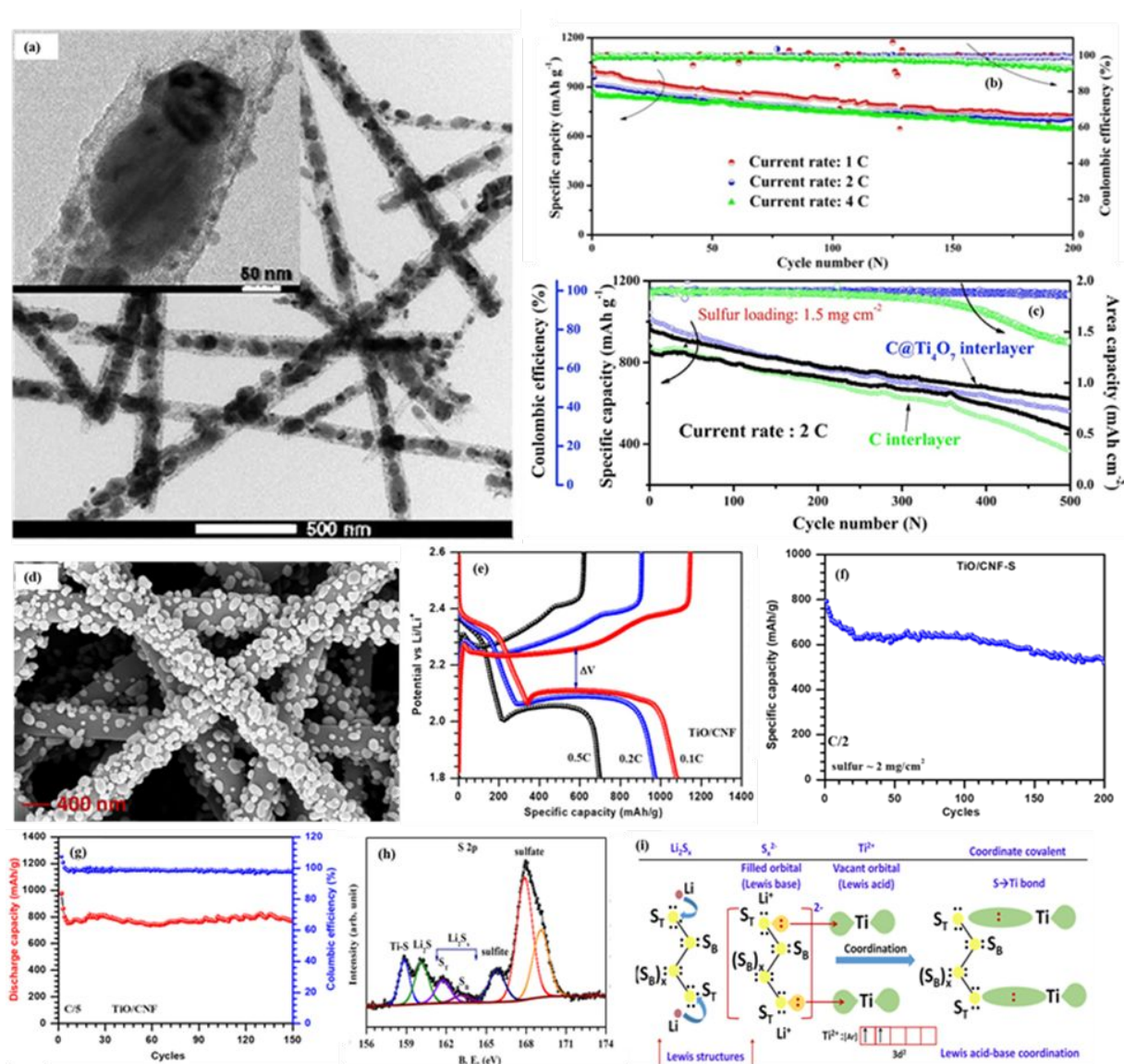


Fig. 10 (a) TEM image of  $C/Ti_4O_7$  nanofibers (the high-resolution image is shown in inset), (b) High rate cycle performance of  $C/Ti_4O_7$  interlayer cells with 0.2 M  $LiNO_3$  additive, and (c) Long term cycle life at 2 C for  $C/Ti_4O_7$  interlayer cells and C interlayer cells (Reproduced with

permission from ref. 212. Copyright 2018 Elsevier Ltd.); (d) SEM image of TiO/CNF nanofibers, (e) First galvanostatic charge–discharge curve for TiO/CNF-S cathodes at different C-rates, (f-g) Cyclic stability test at C/2 and C/5 rates for TiO/CNF-S cathodes over 200 and 150 cycles, respectively, and (h-i) Core-level S 2p for the cycled TiO/CNF-S cathode and a schematic explaining the Ti←S bond formation through coordination between unsaturated Ti-centers (Lewis acid) and terminal S ( $S_T$ ) of polysulfides (Reproduced with permission from ref. 79. Copyright 2018 American Chemical Society.).

The Li-S cells based on S-cathodes (63 wt% and 1.5 mg/cm<sup>2</sup> S in the final cathode) and C/Ti<sub>4</sub>O<sub>7</sub> interlayer exhibited superior electrochemical performance than those fabricated with bare C interlayer. More specifically, Li-S cells with C/Ti<sub>4</sub>O<sub>7</sub> interlayer delivered a high initial discharge capacity (~1046 mAh/g at 2C rate), excellent rate capability (capacities of ~721, 710 and 648 mAh/g at 1C, 2 C and 4 C, respectively after 200 cycles as given in Fig. 10 (b)), and long cycle life (~562 mAh/g at 2C even after 500 cycles as given in Fig. 10 (c)). The Ti<sub>4</sub>O<sub>7</sub> suboxide is one of the Magneli phases (Ti<sub>n</sub>O<sub>2n-1</sub>; 4≤n≤9) of Ti with two equally populated Ti<sup>4+</sup> (d<sup>0</sup>) and Ti<sup>3+</sup> (d<sup>1</sup>) states, high conductivity and ~62.5% unsaturated Ti-centers (Ti<sub>5c</sub> and Ti<sub>4c</sub>) at the surface.<sup>198,207,208,213</sup> These unsaturated Ti-centers with vacant d-orbital (Lewis acid) serve as strong anchoring sites for polysulfide anions (Lewis base- due to lone pair electrons on the terminal S) and hold them through reversible coordinate covalent S←Ti bonding (so-called ‘Lewis acid-base interaction’).<sup>198,207,208</sup> Further, ensemble of these unsaturated Ti-centers in Ti<sub>4</sub>O<sub>7</sub> (every 4<sup>th</sup> edge-shared TiO<sub>6</sub> octahedron is shearing due to the reduction of Ti and O-vacancies) are arranged in the step sites and readily available to polysulfide anions for chemical interactions.<sup>198,207,208</sup> Therefore, the conducting C/Ti<sub>4</sub>O<sub>7</sub> interlayer can alleviate the polysulfide shuttle, and catalytically re-activate



the deposited active materials in a working Li-S cell. All these features of C/Ti<sub>4</sub>O<sub>7</sub> interlayer thus enabled Li-S cells to achieve excellent performance.

Recent theoretical predictions indicate that surface defects and coordination of the terminated Ti-atoms play a decisive role in the binding capability/energy of these Ti-oxides with polysulfides.<sup>210</sup> According to DFT calculations, surface Ti<sub>5c</sub> (5 coordination) atoms have a higher affinity towards polysulfide anions than Ti<sub>6c</sub> atoms.<sup>210,214</sup> Hence, TiO could be more effective in Li-S batteries than Magneli Ti<sub>4</sub>O<sub>7</sub> (with 37-38% Ti-atoms as Ti<sub>6c</sub>) and TiO<sub>2</sub> (with 50% Ti-atoms as Ti<sub>6c</sub>) since all (100%) the surface Ti-atoms in TiO have either Ti<sub>5c</sub> or Ti<sub>4c</sub> coordination number.<sup>209,214</sup> Therefore, our group (Singh *et al.*) recently designed the free-standing mats of TiO/CNF (surface area 427 m<sup>2</sup>/g) nanofibers through electrospinning of the hybrid TIP/PVP gel in binary ethanol/acetic acid solvents and used as a sulfur host in Li-S battery.<sup>79</sup> The SEM image revealed that the fibrous structures of the TiO/CNF sample were coarser with TiO nanoparticles protruding from the surface of nanofibers (Fig 10 (d)). The TiO/CNF-S cathodes (S = ~2 mg/cm<sup>2</sup>; ~50 wt%) fabricated with rapid sulfur melt infiltration (heat-pressing at 140°C for 5 s at a pressure ≤250 psi) technique developed in our lab<sup>215</sup> delivered high initial discharge capacities of ~1080, ~975, and ~791 mAh/g at C/10, C/5, and C/2 rates, respectively (Fig 10 (e)). After an initial capacity drop within few cycles (probably due to redistribution/activation of the elemental sulfur), TiO/CNF-S cathodes showed stable cycling and retained capacity of ~787 mAh/g (C/5) and 518 mAh/g (C/2) over 150 and 200 cycles, respectively (Fig 10 (f-g)). With the postmortem XRD and XPS (S 2p XPS spectra is given in Fig 10 (h)) measurements, we confirmed the presence of reversible coordinate covalent Ti←S bond between TiO (3d<sup>2</sup>) and polysulfide (S<sub>k</sub><sup>2-</sup>) anions. A schematic explaining the Ti←S bond formation through coordination between unsaturated Ti-centers (Lewis acid) and terminal S (S<sub>T</sub>) of polysulfides is given in Fig 10 (i). The high electrical

conductivity (1.1 S/cm) and strong polysulfide binding ability of TiO/CNF allowed Li-S cells to show good performance at 2 mg/cm<sup>2</sup> sulfur loading.

***Heterostructures with catalytic functionality:***

In Li-S batteries, the slow reduction of lithium polysulfides to insoluble Li<sub>2</sub>S<sub>2</sub>/Li<sub>2</sub>S is the leading cause for shuttle effect, which eventually leads to a low coulombic efficiency and a short cycle life.<sup>214</sup> Therefore, an ideal sulfur host is desired to have not only a firm binding with polysulfides but also the ability to promote polysulfides to Li<sub>2</sub>S/Li<sub>2</sub>S<sub>2</sub> conversion (catalytic function).<sup>191,214</sup> In this context, the use of catalytic materials including transition metals and their carbides, nitrides, and sulfides is promising.<sup>191,196,214,216</sup> These materials not only exhibit high polysulfide-anchoring ability through chemical interactions (long cycling stability) but also show a strong catalytic function for the conversion of polysulfides to Li<sub>2</sub>S<sub>2</sub>/Li<sub>2</sub>S (fast kinetics, high capacity).<sup>214,216</sup> There are quite a few reports on the use of such catalytic materials (e.g., TiN, TiC, CoS<sub>2</sub>, VN) in Li-S batteries aiming at high capacity and long cycle life.<sup>195,214,217-222</sup> Nevertheless, in most of the studies, these materials are usually present as large crystallites, which eventually offer a reduced number of active sites for polysulfide interactions and catalytic function. Furthermore, a multi-step synthesis process is generally required to develop these materials for their productive use in Li-S battery. In this context, the electrospinning technique could offer a simple, and economical approach for the fabrication of heterostructures of metal carbides, sulfides, and nitrides with controllable crystallite size. At present, the development of heterostructures of these materials through electrospinning technique is still in its nascent stage. Recently, Shang *et al.* developed free-standing N-doped CNF/ $\beta$ -Mo<sub>2</sub>C (NCNF-Mo<sub>2</sub>C) electrodes by electrospinning a solution of PAN/molybdenum diacetylacetonate dioxide in DMF solvent and used them as a 3D current collector in Li-S batteries.<sup>193</sup> The annealed NCNF-Mo<sub>2</sub>C preserved the interconnected 3D

framework structure with long and straight nanofibers as shown in Fig 11 (a). The HRTEM image in Fig. 11 (b) confirmed the tight loading of ultrafine  $\text{Mo}_2\text{C}$  nanostructure (2-10 nm) without aggregation onto the nanofiber. The Energy-dispersive X-ray spectroscopy (EDS) mapping evidenced that constituent C, Mo and N elements possessed a correlated spatial distribution (Fig. 11 (c)). The electrochemical performance was tested using 1M  $\text{Li}_2\text{S}_6$  catholyte (as an active material; corresponds to 2 mg S) and an etheral electrolyte. The NCNF- $\text{Mo}_2\text{C}$  based Li-S cells delivered a high capacity of 1086 mAh/g at C/5 rate (after initial activation cycles), excellent rate performance up to 1C (750 mAh/g), high coulombic efficiency ( $\sim 100\%$ ) and prolonged cycling over 275 cycles at C/5 without apparent capacity fading (retention  $\sim 100\%$ ) (Fig. 11 (d)).

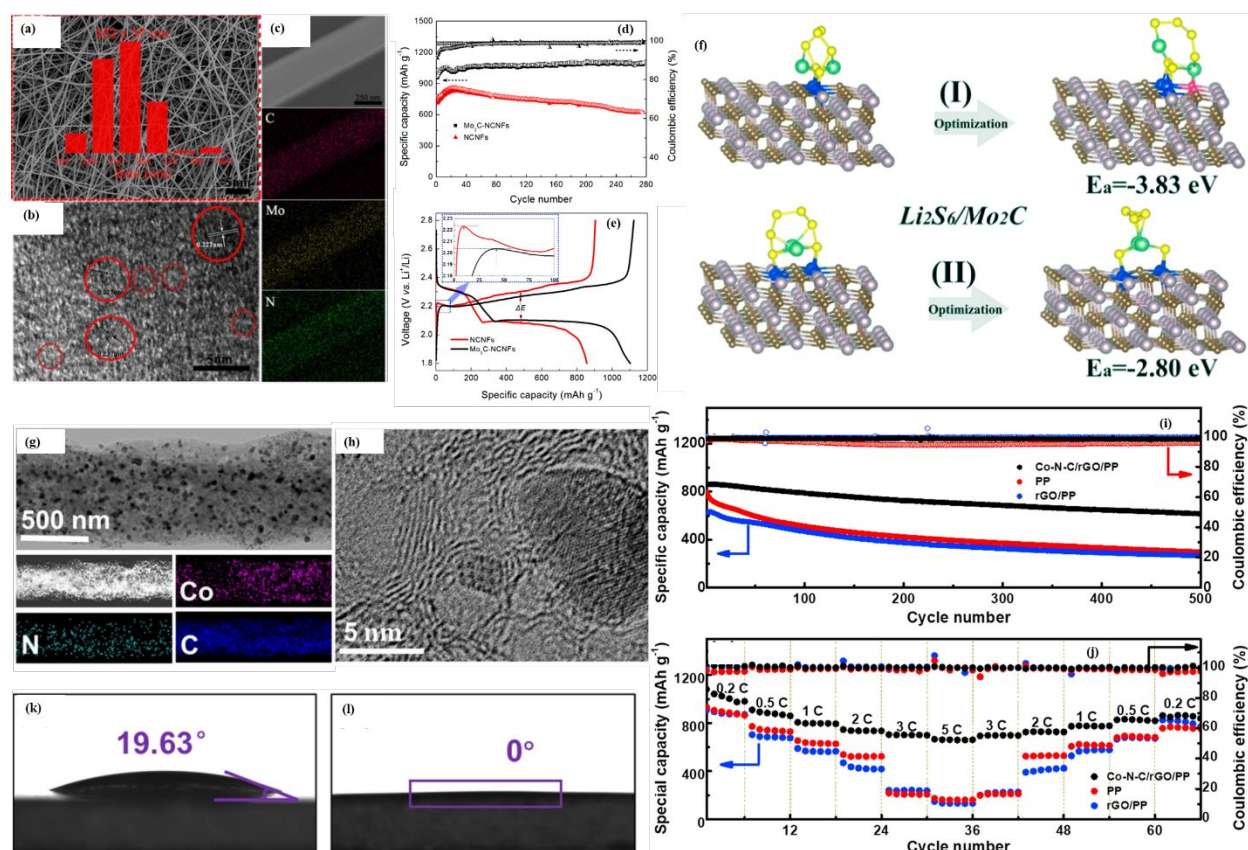


Fig. 11 (a-b) SEM and TEM images of NCNFs- $\text{Mo}_2\text{C}$ , respectively (nanofibers display average diameter of  $252 \pm 37$  nm as shown in the inset of (a)), (c) SEM image and corresponding EDS

elemental mapping of NCNFs-Mo<sub>2</sub>C, (d) Cycling stability and Coulombic efficiency of NCNFs-Mo<sub>2</sub>C and NCNFs based Li-S cells, (e) Galvanostatic charge-discharge voltage profiles of the stable cycle at 0.2 C and selected charge profiles (inset) for NCNFs-Mo<sub>2</sub>C and NCNFs based Li-S cells, and (f) DFT results of two stable binding configuration of Li<sub>2</sub>S<sub>6</sub> with a single layer of Mo<sub>2</sub>C (101) with calculated binding energy of (I) -3.83 eV, (II) -2.8 eV. (Reproduced with permission from ref. 193. Copyright 2018 Published by Elsevier B.V.); (g) TEM and EDS mapping of Co-N-CNFs, (h) High-resolution TEM image of the Co-N-CNFs, (i-j) Cycling stability and rate capability of the cells with different separators over 500 cycles at 0.5 C, respectively and (k-l) Contact angle photographs of PP and Co-N-CNFs/rGO/PP separator using liquid electrolyte (Reproduced with permission from ref. 225. Copyright 2017 Elsevier B.V.).

Moreover, the NCNF-Mo<sub>2</sub>C electrode showed a relatively lower polarization ( $\Delta E$ ; the difference between oxidation and reduction potential) and lower overpotential (energy barrier for Li<sub>2</sub>S → S<sub>k</sub><sup>2-</sup> ( $k \geq 4$ ) conversion during charge process) than that of bare NCNF (without Mo<sub>2</sub>C), which indicates its catalytic functionality (Fig. 11 (e)). Here, the hexagonal  $\beta$ -Mo<sub>2</sub>C with high electrical conductivity ( $\sim 10^2$  S/cm) served as a polar metallic substrate offering a strong affinity towards polysulfides and enhancing transformation between soluble polysulfides and insoluble solid-state products viz., S and Li<sub>2</sub>S<sub>2</sub>/Li<sub>2</sub>S. Using DFT calculations, authors also show that a much stronger Mo-S type chemical bonding (B. E. = 3.83 eV) is present between Mo of the Mo<sub>2</sub>C (101) and S of the Li<sub>2</sub>S<sub>6</sub> (Fig. 11 (f)). Therefore, the free-standing NCNF-Mo<sub>2</sub>C electrode has a 'positive' catalytic effect and strong affinity to polysulfides, which eventually led to an outstanding electrochemical performance in Li-S cell.

Recently, some approaches have also been dedicated to modifying the commercial separator with functional materials (for conductivity and polysulfide binding) in order to alleviate

the polysulfide shuttle and protect the Li-anode in Li-S batteries.<sup>223,224</sup> A thin layer of functional material on separator allows reducing the weight/volume fraction occupied by these inactive materials without sacrificing their activity, which is essential for the high energy density of Li-S batteries.<sup>223</sup> Various materials including metal oxides, polymers, and functionalized carbon have been used as ion-sieving layer on separators to improve the performance of Li-S batteries.<sup>159,173,174,223-226</sup> However, it is still critical to develop lightweight, thin coating-layers (on the cathode side) of these multifunctional materials on separators while retaining fast Li-ion diffusion, especially with nanoparticles due to aggregation during slurry-cast process.<sup>226</sup> In this regard, Chen *et al.* proposed the use of electrospun cobalt, nitrogen co-doped porous CNF/reduced graphene oxide (Co-N-CNF/rGO) as a thin layer on commercial PP (polypropylene) separator in Li-S batteries.<sup>225</sup> First, mesoporous Co-N-CNF nanofibers (a surface area  $\sim 470 \text{ m}^2/\text{g}$ , pore volume  $\sim 0.439 \text{ cm}^3/\text{g}$ , average pore diameter  $\sim 3.5 \text{ nm}$ ) were fabricated by electrospinning a solution of PAN,  $\text{SiO}_2$  (template), and Co-precursor followed by carbonization ( $800^\circ\text{C}$ , 2h, argon flow) and template removal with NaOH. The TEM results showed that ultrafine Co nanoparticles (average size  $\sim 24 \text{ nm}$ ) were dispersed uniformly in the nanofibers (Fig. 11 (g)). EDS mapping further showed a homogeneous distribution of Co, N and C elements along the whole nanofiber (Fig. 11 (g)). In addition, many crooked graphitic lattice fringes were clearly observed on the edge of metallic Co (Fig. 11 (h)), suggesting that metallic Co was wrapped by graphitic carbon through a self-assembly approach. A dispersion of Co-N-CNF and rGO (in ethanol) was then deposited on PP separator by vacuum filtration to get a  $\sim 6\mu\text{m}$  thick ( $0.083 \text{ mg}/\text{cm}^2$ ) coating of Co-N-CNF/rGO composite. The electrochemical performance was evaluated using a slurry based S-cathode ( $\sim 63 \text{ wt}\%$ ,  $1.2 \text{ mg}/\text{cm}^2 \text{ S}$  in the final cathode) and an ethereal (LiTFSI in DME: DOL) electrolyte. The Li-S cell based on the modified (with Co-N-CNF/rGO) PP separator delivered a high capacity of

~1344 mAh/g at C/10, high rate capability (~659 mAh/g at 5C) (Fig. 11 (j)), excellent cycling stability (~71.2 % retention of the initial capacity of ~865 mAh/g at C/2 over 500 cycles) (Fig. 11 (i)) and high coulombic efficiency (~100%). Here, the rGO not only served as a blocking (physical/chemical) layer for polysulfides but also helped to construct a stable film on the separator. The N-CNF component forms a 3D conducting network, which improves the electrolyte wettability of the separator and ensures easy Li<sup>+</sup> transport hence guarantee high rate performance. The contact angle results displayed that the ethereal electrolyte thoroughly wets the modified separator within 2s; much better than bare PP separator (contact angle ~19.63°) (Fig. 11 (k)). Furthermore, the ultrafine metallic Co nanoparticles in nanofibers improve the sulfur utilization (due to conductivity) and redox kinetics (due to catalytic functionality), thus giving rise to excellent cycling stability and high coulombic efficiency.

In summary, confining the lithium polysulfides through strong chemical interactions (Lewis acid-base or polythionate type) and improving the redox kinetics together is critical to achieving a remarkable electrochemical performance in Li-S batteries. Undoubtedly, the electrospun heterostructures of transition metals and their oxides, and carbides have shown great potential in this context and played a significant role in the recent advancement of Li-S batteries. However, there is lot more room for improvements by (i) designing these materials with different crystalline phases, lattice orientations, and oxidation states (of metal), (ii) rationalizing their texture properties using templates for optimal active sites, and (iii) reducing their mass/volume fraction in the final cathode. In this view, the electrospinning technique is versatile, which could offer a simple, inexpensive and industry viable synthesis approach to bring these abovementioned features into a single material. In the following sections, we will now review recent advances made in other sulfur batteries (e.g., Na-S) and metal-selenium batteries using electrospun materials.

### 3.2 Electrospun nanostructures for RT Na-S batteries:

The low-cost and natural abundance of the sodium element has stimulated research on Na-S batteries beyond the analogous Li-systems.<sup>227</sup> The high-temperature (300-350°C) Na-S technologies, with a molten Na-electrode and a solid  $\beta$ -Al<sub>2</sub>O<sub>3</sub> electrolyte are now commercially available.<sup>93,228,229</sup> However, the highly corrosive nature of molten Na imposes severe safety and maintenance challenges and demands the use of expensive highly alloyed steels.<sup>90,93</sup> Therefore, high cost and high-temperature operation impede their use in EVs.<sup>90,230</sup> The room-temperature (RT) Na-S batteries are cost-effective, and much safer thus desirable for large stationary grids and EVs.<sup>90,231</sup> Therefore, research on the development of high-performance RT Na-S is currently predominant. The RT Na-S cell comprises a sulfur cathode, suitable electrolyte (etheral or carbonate based), separator and a Na metal as the anode. In RT Na-S cells, S is electrochemically reduced to Na<sub>2</sub>S during discharge through soluble intermediates (Na<sub>2</sub>S<sub>k</sub>; k≥4), which is analogous to Li-S batteries (Fig. 2 (a)).<sup>90,227,231</sup> Therefore, RT Na-S batteries also face all the common intrinsic challenges of a Li-S system including low sulfur utilization, volume expansion, and ill-famed shuttle effect (Fig. 2 (b-d)).<sup>90,231-233</sup> Over the last few years, a range of similar conventional approaches (used for Li-S system) has been applied to cope with such issues by designing novel porous and conducting host materials for sulfur, employing sodium polysulfides (catholytes) or sulfurized-PAN as active materials, passivating the Na-anode, and modifying/coating separators with functional materials (e.g., Nafion).<sup>94,233-242</sup> However, the reported electrochemical performances are not satisfactory because the electrochemistry of RT Na-S cell is even more challenging regarding sulfur utilization due to the large size of Na<sup>+</sup> ion<sup>90</sup>, and volume change (i.e., pulverization) during sodiation (S→Na<sub>2</sub>S; ~260%),<sup>90,231</sup> which lead to low reversible capacity and rapid capacity fade during cycling. As mentioned earlier, electrospinning is a straightforward, cost-

effective and industry-viable approach, which offers flexibility in designing materials with tunable texture properties for accommodation of S and volume changes and surface activity for alleviation of the shuttle effect. Therefore, recent studies have been inclined towards the development of rationally engineered novel electrospun nanostructures for RT Na-S batteries.<sup>243-246</sup> However, in this section, we will only focus on some representative examples of these nanostructures, which are producing exceptional electrochemical performance in RT Na-S batteries. For example, Xia *et al.* recently reported the controllable fabrication of carbon hollow nanobubbles on N- and O- doped porous carbon nanofibers (CHNBs@PCNF) as a sulfur host for RT Na-S batteries (Fig. 12 (a)).<sup>107</sup> The CHNBs@PCNF electrodes (surface area = 420 m<sup>2</sup>/g, pore volume = 1.64 cm<sup>3</sup>/g) were prepared by electrospinning a solution of PVA/LiN<sub>3</sub> in water followed by drying at 75°C under dynamic vacuum and calcination at 650°C for 3h under N<sub>2</sub> environment. Before calcination, the as-spun LiN<sub>3</sub>/PVA nanofibers were stabilized at 240°C for 2 h at slow heating (0.5-1.0°C/min) under nitrogen environment. The slow stabilization could blow up the PVA through gentle N<sub>2</sub> desorption ( $6\text{LiN}_3 \rightarrow 2\text{Li}_3\text{N} + 8\text{N}_2$ ), leading to the formation of CHNBs on the CNF. The CHNBs@PCNF were finally washed with hydrochloric acid (HCl) to remove residual impurities (e.g., Li<sub>2</sub>CO<sub>3</sub>) and dried. The TGA results further showed that LiN<sub>3</sub> also served as a source of N-dopant into CNF. The SEM image in Fig 12 (b) showed that a plethora of nanobubbles with diameters between 10-60 nm were uniformly and densely distributed on the surfaces of the as-prepared CHNBs@PCNF. The TEM image further confirmed that these carbon nanobubbles were hollow and that the shells were very thin, with a thickness of only ~2 nm (Fig 12 (c)). The S/CHNBs@PCNF cathodes (~57 wt%, 1.4 mg/cm<sup>2</sup> S in the final cathode) were prepared by facile melt-infiltration method (155°C/12 h). The electrochemical tests were conducted in carbonate-based electrolyte (1M sodium perchlorate (NaClO<sub>4</sub>) in EC/PC, 1:1 v/v% with the addition of 5



wt.% fluoroethylene carbonate (FEC)) within 1.2-2.8 V potential range (vs. Na/Na<sup>+</sup>). The S/CHNBs@PCNFs cathode delivered an initial discharge capacity of ~1214 mAh/g at C/10 rate, good cycling stability with ~65% capacity retention over 50 cycles and excellent rate performance up to 2C (~302 mAh/g); exceeding those Na-S cells fabricated with the control S/CNF cathode. Furthermore, S/CHNBs@PCNFs cathodes displayed long-term cycling over 400 cycles at 2C with a low capacity fading rate (0.044% per cycle) as given in Fig 12 (d).

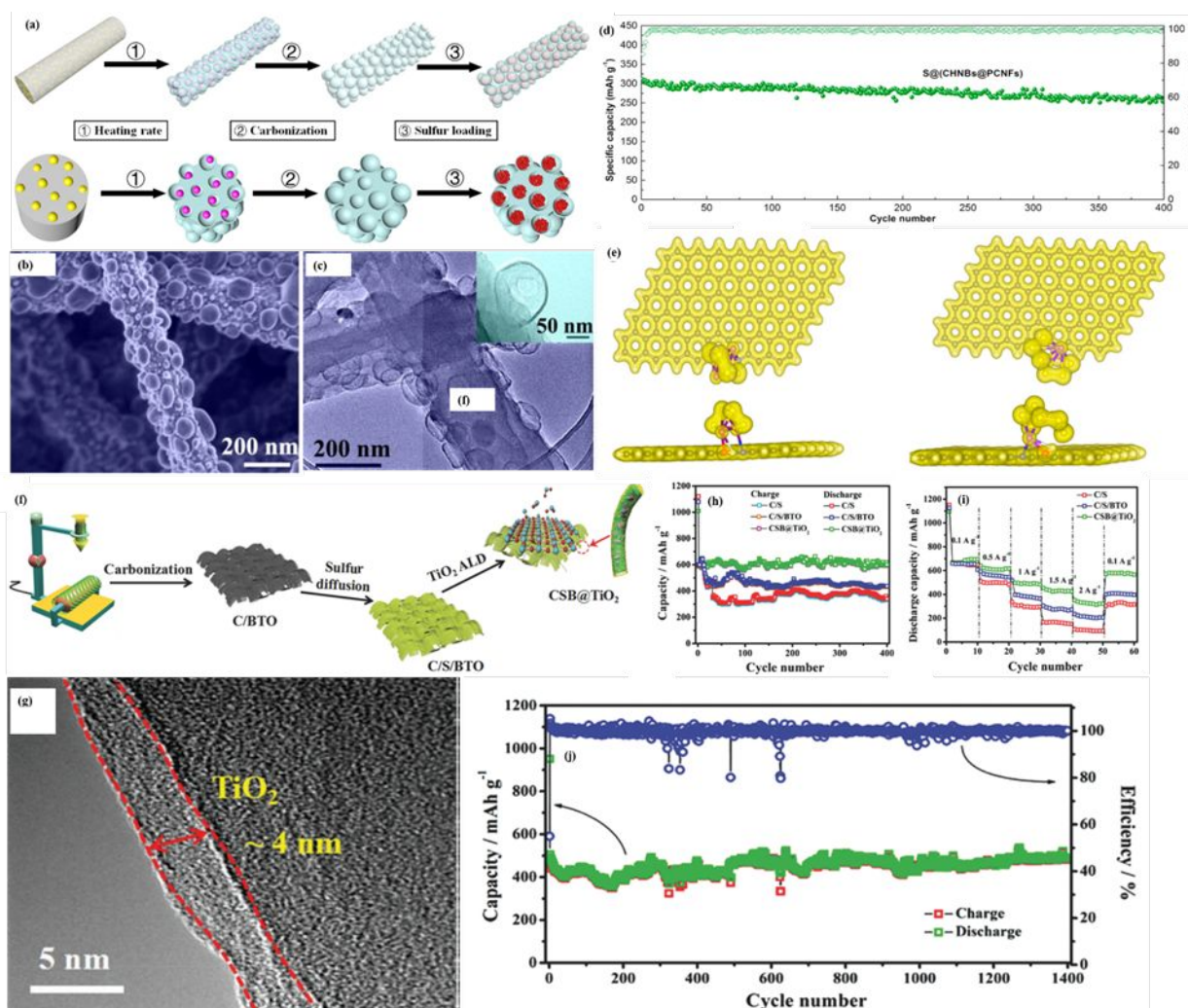


Fig. 12 (a) Schematic illustration of the preparation of S/CHNBs@PCNFs cathodes for room temperature Na-S batteries. Yellow, pink, and red balls represent LiN<sub>3</sub>, Li<sub>3</sub>N, and S particles,

respectively, (b) SEM images of CHNBs@PCNFs after calcination of as-electrospun PVA-LiN<sub>3</sub> nanofibers, (c) TEM image of the as-synthesized CHNBs@PCNFs (The high-resolution image is shown in inset), (d) Cycling performance of Li-S cells based on S/CHNBs@PCNFs cathodes at a current density of 2 C, and (e) Atom positions and charge density plot of Na<sub>2</sub>S<sub>4</sub> (left) and Na<sub>2</sub>S<sub>6</sub> (right) molecular interaction with N, O-codoped carbon. Grey, white, blue, yellow, purple, and red balls represent C, H, N, S, Na, and O atoms, respectively. (Reproduced with permission from ref. 107. Copyright 2018 Published by Elsevier B.V.); (f) Schematic illustration of the CSB@TiO<sub>2</sub> electrode preparation process, (g) TEM image of the CSB@TiO<sub>2</sub> nanofiber, (h) Cycling performance of C/S, C/S/BTO, and CSB@TiO<sub>2</sub> electrodes at 0.5 A/g, (i) Rate capability of C/S, C/S/BTO, and CSB@TiO<sub>2</sub> electrodes at varied current density from 0.1 to 0.5, 1, 1.5, and 2 A/g, and (j) The long-term cycling of CSB@TiO<sub>2</sub> electrode after 1400 cycles at 1 A/g (Reproduced with permission from ref. 247. Copyright 2018 WILEY-VCH Verlag GmbH & Co. KGaA, Weinheim.).

The excellent electrochemical performance of the S/CHNBs@PCNFs cathode was attributed to various unique features of electrospun CHNBs@PCNF structures. The CHNBs on PCNFs effectively facilitated the wettability of the electrode and accommodated the volume changes during cycling. The 1D robust PCNF structures ensured continuous electron supply during oxidation/reduction reactions and mechanical integrity of the cathode. The N- and O-functionalities led to adsorption and trapping of sodium polysulfides and alleviated the shuttle effect. Using DFT calculations, authors showed that lone pair electrons of N- and O-atoms in the C-lattice directly interacted with terminal Na of the sodium polysulfides (Na<sub>2</sub>S<sub>k</sub>) and suppressed their dissolution and shuttling (Fig 12 (e)). All these features allowed S/CHNBs@PCNFs cathodes to show excellent reversible capacity, high rate capability, and long cycle life.

As seen in Li-S batteries, polar metal oxides could strongly bind intermediate polysulfides through chemical interactions and immobilize them on the cathode side. With inspiration from these approaches, Ma *et al.* recently reported a new strategy for developing ultrastable RT Na-S batteries based on S/BaTiO<sub>3</sub>-C-TiO<sub>2</sub> (CSB@TiO<sub>2</sub>) composite cathodes.<sup>247</sup> First, they developed BaTiO<sub>3</sub> (BTO, ~3 wt%) encapsulated porous CNF (CB) by electrospinning a solution of PAN/triblock copolymer F127/BaTiO<sub>3</sub> in DMF solvent and subsequently stabilizing (280°C for 4h; air) and carbonizing (900°C for 6 h; N<sub>2</sub>) the as-spun nanofibers. Here, the F127 copolymer not only served as a surfactant for uniform dispersion of BaTiO<sub>3</sub> into CNF but also acted as a soft template for pore formation (surface area of CB = 589 m<sup>2</sup>/g, pore sizes 1-3 nm). Then, the CSB cathodes were prepared using the sulfur melt-infiltration method (160°C, 10h). Finally, a protecting layer of amorphous TiO<sub>2</sub> (~4 nm thick) was directly grown on the free-standing CSB cathodes with the help of atomic layer deposition (ALD) technique to get free-standing, binder-free CSB@TiO<sub>2</sub> cathodes (60 wt%, 1.2-1.4 mg/cm<sup>2</sup> S in the final cathode). A schematic illustration of the CSB@TiO<sub>2</sub> electrode preparation process is shown in Fig. 12 (f). The TEM image in Fig. 12 (g) showed ~4 nm thick nanolayer of TiO<sub>2</sub> grown on the surface of the nanofibers. Two control samples viz., C/S and C/S/BTO with similar S-loading were also prepared for comparison. The electrochemical measurements were conducted using 1 M of NaClO<sub>4</sub> in a binary EC: DEC (1:1 v/v) solvent. The CSB@TiO<sub>2</sub> cathodes displayed a high discharge capacity of ~592 mAh/g (2<sup>nd</sup> cycle) at 0.5 A/g, better rate capability up to 2 A/g (~350 mAh/g) and superior cycling performance (~611 mAh/g at 0.5 A/g after 400 cycles) as compared to other two (C/S and C/S/BTO) cathodes (Fig. 12 (h-i)). It is noteworthy that CSB@TiO<sub>2</sub> cathodes exhibited capacity of ~525 mAh/g after 1400 cycles at 1 A/g (Fig. 12 (j)) and ~382 mAh/g at 2 A/g after 3000 cycles. The remarkable

electrochemical performance of CSB@TiO<sub>2</sub> cathodes was a consequence of various favorable aspects present in the electrospun/ALD based CB@TiO<sub>2</sub> structures as summarized below:

(i) The electrospun 3D architecture of porous CNF facilitated the sulfur utilization and redox reactions *via* inherent electronic (conducting CNF) and ionic (inter-fiber macropores) channels.

(ii) The ferroelectric (BTO, ~3 wt%) additive further improved the surface affinity of CNF towards intermediate sodium polysulfides (Na<sub>2</sub>S<sub>k</sub>). The BaTiO<sub>3</sub> (BTO) is a ferroelectric material, which has a spontaneous electrical polarization (induced dipole moment) in the electric field. Therefore, the heteropolar intermediate polysulfides could chemisorb on the spontaneously polarized BTO nanoparticles to screen these induced surface charges (internal electric field). Similar studies have been reported in the Li-S system and shown that the BTO provides a stable interaction-surface for polysulfides trapping and maintains its ferroelectricity over cycling.<sup>248</sup>

(iii) The uniform thin layer of amorphous TiO<sub>2</sub> maintained the structural integrity of CSB@TiO<sub>2</sub> cathodes by inhibiting the pulverization of electrodes during dramatic volume changes and confined sodium polysulfides through strong polar-polar interactions.

All these features allowed CSB@TiO<sub>2</sub> cathodes to exhibit high capacity, excellent rate capability, and ultralong cycle life. It is noteworthy that both the BTO and TiO<sub>2</sub> served as additives (total wt% <10%) in the CSB@TiO<sub>2</sub> cathodes resulting in high sulfur content (~60 wt%) in the final cathode.

Undoubtedly, the research on the cost-effective RT Na-S technology is booming. Even though the significant progress regarding sulfur utilization and cycle life has been made in recent years using electrospun nanostructures, the RT Na-S technology is still in its nascent state. More intense research is required to improve the performance of RT Na-S technology further under realistic conditions. The rich experience and scientific knowledge developed over the last few years in Li-S technology should be exerted for the advancement of RT Na-S batteries. Particularly,

rationally designed various electrospun heterostructures with suitable pore size/volume and polar additives should be explored as sulfur hosts, interlayers, and electrolyte membranes to bring significant breakthroughs in RT Na-S batteries shortly.

### 3.3 Electrospun nanostructures for M-S<sub>x</sub>Se<sub>y</sub> and M-Se batteries:

Due to the semiconducting nature of elemental Se, a small amount of Se can be introduced to S molecules to improve the electrochemical activity of elemental sulfur.<sup>51</sup> The formed heterocyclic S-rich S<sub>x</sub>Se<sub>y</sub> compounds represent a new class of materials with improved conductivity (kinetics) compared to elemental S and higher theoretical capacity than elemental Se alone.<sup>87,95,249</sup> The preparation of S<sub>x</sub>Se<sub>y</sub> compounds requires a thermal treatment of S/Se mixture at a temperature close to the melting point of Se, at which both components are reasonably miscible.<sup>51,87</sup> After the seminal work reported by Amine and co-workers<sup>48</sup>, various S<sub>x</sub>Se<sub>y</sub> compounds such as SeS<sub>2</sub>, Se<sub>2</sub>S<sub>5</sub>, S<sub>0.94</sub>Se<sub>0.06</sub> with porous and conducting host materials (e.g., carbon) have been explored in Li-S and RT Na-S batteries.<sup>249-251</sup> Inspired by the recent advances obtained using electrospun nanostructures, Yao *et al.* recently developed free-standing S<sub>0.6</sub>Se<sub>0.4</sub>@CNF composite films with sulfur atoms bonded to carbon (C-S) lattice through simple electrospinning technique and used them as cathodes in Li-S and RT Na-S batteries.<sup>252</sup> The PAN nanofibers were produced by electrospinning of the PAN/DMF solution. The S<sub>0.6</sub>Se<sub>0.4</sub> compound was prepared by ball-milling of commercial S/Se (S/Se molar ratio = 1.5) powders for 24 h and subsequent heating at 260°C for 12 h in a sealed autoclave. The S<sub>0.6</sub>Se<sub>0.4</sub>@CNF composite cathodes (~57.5 wt%, 0.9 mg/cm<sup>2</sup> active material) were then prepared by co-heating PAN nanofibers and S<sub>0.6</sub>Se<sub>0.4</sub> compound at 600°C for 6 h (3 K/min) in a sealed vessel. The scanning transmission electron microscopy (STEM) image and element mapping of one part of an individual S<sub>0.6</sub>Se<sub>0.4</sub>@CNFs showed that the CNFs exhibited a smooth surface and S and Se were distributed uniformly all over the carbon matrix (Fig. 13 (a)).

The C-S stretching vibrations at 176 and 805  $\text{cm}^{-1}$  in the Raman spectra confirmed the C-S bonding in the  $\text{S}_{0.6}\text{Se}_{0.4}@CNF$  cathode after co-heating  $\text{S}_{0.6}\text{Se}_{0.4}$  and CNF fibers (Fig. 13 (b)). The XRD results showed that a reaction between S (space group of Fddd(70)) and Se (space group of P3121(152)) leads to the formation of  $\text{S}_{0.6}\text{Se}_{0.4}$  (space group of P2/c(13)) with S-Se bonding (Fig. 13 (c)). The electrochemical performance of  $\text{S}_{0.6}\text{Se}_{0.4}@CNF$  cathodes in Li-S cells was tested using 1 M  $\text{LiPF}_6$  in ethylene carbonate-dimethyl carbonate. The electrochemical impedance analysis showed a reduced charge transfer resistance for  $\text{S}_{0.6}\text{Se}_{0.4}@CNF$  than  $\text{S}@CNF$  in Li-S cells indicating conductivity enhancement due to the presence of Se. The Li-S cells with  $\text{S}_{0.6}\text{Se}_{0.4}@CNF$  cathode maintained a high reversible capacity of  $\sim 450$  mAh/g at 0.1 A/g with  $\sim 100$  coulombic efficiency and excellent rate performance (379 mAh/g at 2 A/g) (Fig. 13 (d)); exceeding those of Li-S cells fabricated with S/CNF ( $\sim 226$  mAh/g after 100 cycles and 82 mAh/g at 2 A/g). Furthermore, the  $\text{S}_{0.6}\text{Se}_{0.4}@CNF$  cathode maintained the capacity of  $\sim 346$  mAh/g at 1 A/g over 1000 cycles almost without capacity loss (Fig. 13 (e)). Moreover, the  $\text{S}_{0.6}\text{Se}_{0.4}@CNF$  cathodes were also used in RT Na-S batteries using 1 M  $\text{NaClO}_4$  in ethylene carbonate-polycarbonate as electrolyte. At 0.1 A/g, Na-S cell with  $\text{S}_{0.6}\text{Se}_{0.4}@CNF$  cathode delivered a discharge capacity of  $\sim 417$  mAh/g (with coulombic efficiency near to 100%) after little capacity loss during initial few activation cycles and retained  $\sim 90\%$  of the initial capacity over 100 cycles (Fig. 13 (f)). Moreover, at 0.5 A/g, the  $\text{S}_{0.6}\text{Se}_{0.4}@CNF$  cathode maintained  $\sim 70\%$  of the initial capacity of  $\sim 290$  mAh/g over 160 cycles (Fig. 13 (g)). The excellent performance of the  $\text{S}_{0.6}\text{Se}_{0.4}@CNF$  cathode in Li-S and RT Na-S cells was attributed to (i) the introduction of Se to S, which significantly improved the sulfur utilization and suppressed the polysulfide dissolution, (ii) the formation of the C-S bond during co-heating, which helped further in alleviating the shuttle effect, and (iii) the electrospun

free-standing 3D CNF architecture, which facilitated the electrolyte transport and accommodated the volume changes during reduction/oxidation reactions.

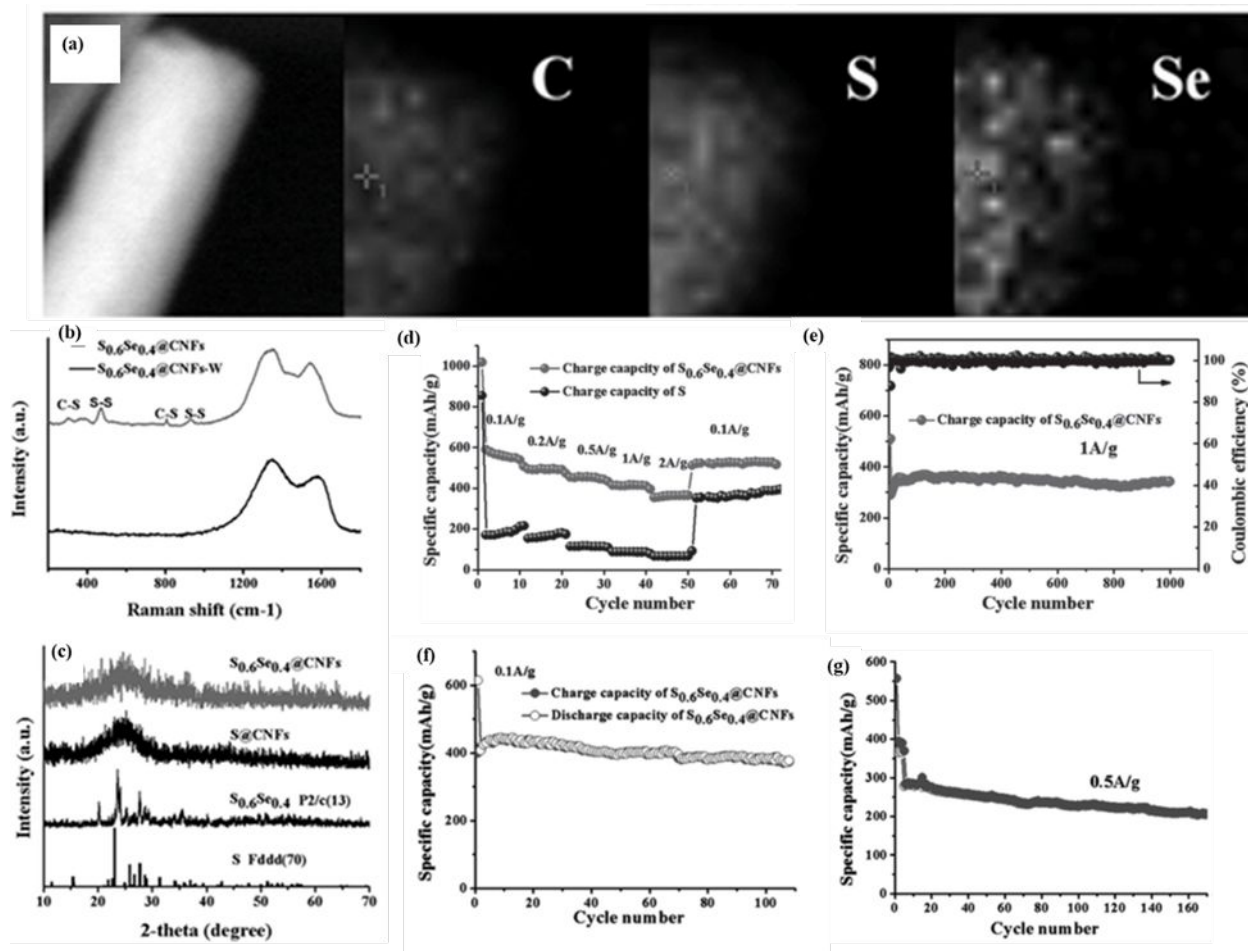


Fig. 13 (a) Scanning transmission electron microscope (STEM) and corresponding element mapping (carbon, sulfur, selenium) of one part of an individual  $S_{0.6}Se_{0.4}@CNFs$ , (b) Raman spectrum of  $S_{0.6}Se_{0.4}@CNFs$  (co-heating PAN and  $S_{0.6}Se_{0.4}$  compound) and  $S_{0.6}Se_{0.4}@CNFs-W$ . The  $S_{0.6}Se_{0.4}@CNFs-W$  electrode was prepared by first carbonizing PAN to CNFs and then infiltrating  $S_{0.6}Se_{0.4}$  compound in order to show that co-heating was responsible for C-S formation, (c) XRD patterns of  $S_{0.6}Se_{0.4}@CNFs$  and  $S@CNFs$ , (d) Rate performance of  $S_{0.6}Se_{0.4}@CNFs$  and  $S@CNFs$  for Li-S batteries, (e) Long-term cycling performance of  $S_{0.6}Se_{0.4}@CNFs$  electrode in

Li-S batteries at 1 A/g for 1000 cycles, (f) Cycle performances of  $S_{0.6}Se_{0.4}@CNFs$  in RT Na-S batteries at a current density of 0.1 A/g, and (g) Cycle performances of  $S_{0.6}Se_{0.4}@CNFs$  in RT Na-S batteries at a current density of 0.5 A/g (Reproduced with permission from ref. 252. Copyright 2017 Wiley-VCH Verlag GmbH & Co. KGaA, Weinheim).

Different M-Se (M: Li, Na) chemistries have also been developed with the use of elemental Se as an active material.<sup>95</sup> However, similar to M-S (Fig. 2 (a)), the M-Se batteries also suffer from the shuttle effect and volume changes during reduction/oxidation process (Fig. 2 (c-d)).<sup>51,87,95</sup> Consequently, various porous nanostructures of carbon such as hollow carbon spheres<sup>253</sup>, heteroatoms (N and O) dual-doped hierarchical porous carbon<sup>254</sup>, microporous carbon<sup>255</sup>, nitrogen-doped carbon scaffolds<sup>88</sup>, mesoporous graphitic carbon microspheres<sup>256</sup>, tube-in-tube carbon<sup>257</sup>, monolithic carbons<sup>258</sup>, graphite platelet nanofiber<sup>259</sup>, Co and N co-doped porous graphitic carbon<sup>260</sup>, and 3-D hierarchical porous tubular carbon<sup>261</sup> have been employed as Se host matrix to surmount these challenges and improve the electrochemical performance of M-Se batteries.

Very recently, the use of elemental Se with various electrospun host materials have also been proposed as a promising cathode in Li-Se and RT Na-Se batteries.<sup>262,263</sup> Park *et al.* recently developed Se-infiltrated MOF-derived porous CNF based cathodes (Se/BP-CNF; 42 wt% Se in the final cathode) for high capacity and rate performance in Li-Se batteries (Fig. 14 (a)).<sup>264</sup> The porous CNF with bimodal micro/mesopores (BP-CNF, surface area = 788 m<sup>2</sup>/g) and enlarged pore volumes were fabricated by electrospinning a solution of ZIF-8 nanoparticles/PAN in DMF and subsequently carbonizing at 800°C for 2 h in Ar flow and activating with KOH. The ZIF-8 with Zn ions and organic ligands served as a template to introduce mesopores into CNF whereas the chemical activation with KOH helped to create micropores into CNF. The CNF were etched with a hydrochloric solution to remove residual metallic Zn impurities before KOH treatment. The SEM



and TEM results (Fig. 14 (b-c)) showed well distributed hollow carbon nanocages within 1D BP-CNF structures originated from the removal of ZIF-8 particles and by the activation process. The Se infiltration was carried out by heating BP-CNF and Se powder together in two steps, at 260°C for 12 h and 350°C for 1 h under Ar environment. The elemental mapping images shown in Fig. 14 (d) revealed that Se was confined within the porous structure of BP-CNF, which further confirmed the existence of small-sized micropores. The electrochemical measurements were performed in 1 M LiPF<sub>6</sub> dissolved in EC/DEC (1:1 v/v). The CV curves of Se/BP-CNF cathode displayed two small peaks at 2.3 and 2.1 V (absent in the 2<sup>nd</sup> cycle) and one main reduction peak at 1.8 V in the first discharge (Fig. 14 (e)). These two small peaks at 2.3 and 2.1 V are attributed to the transformation of ring-like selenium (r-Se) to chain-like selenium (c-Se) whereas the strong reduction peak at 1.8 V is due to the conversion of Se to Li<sub>2</sub>Se. The oxidation peak at 2.1 V during anodic sweep represents the transformation of Li<sub>2</sub>Se into elemental Se. The initial discharge capacities of Se/BP-CNF and Se/M-CNF (M-CNF: mesoporous CNF without KOH activation, surface area = 209 m<sup>2</sup>/g) cathodes at C/2 rate were 921 and 342 mAh/g, respectively, and their initial coulombic efficiencies were ~81 and ~29%, respectively. The high discharge capacity of the Se/BP-CNF cathode was attributed to the high utilization of c-Se with low-range ordering formed due to the presence of well-developed micropores into the BP-CNF. In contrast, Se/M-CNF cathode displayed a low initial discharge capacity due to the formation of inactive selenium cores within large carbon nanocages of M-CNF during the selenium melt diffusion process. Notably, Se/BP-CNF cathode retained ~79.2% (from the 2<sup>nd</sup> cycle) of the initial discharge capacity at C/2 rate after 300 cycles (Fig. 14 (f)). Moreover, Se/BP-CNF cathode exhibited excellent rate performance up to 10.0C (capacity ~568 mAh/g) (Fig. 14 (g)). The excellent electrochemical properties of Se/BP-CNF cathodes in Li-Se batteries were attributed to the unique electrospun

bimodal 1D CNF structures where micropores led to the formation of c-Se with short-range ordering and mesopores facilitated the electrolyte transport and utilization of c-Se. Similarly, Yuan *et al.* recently proposed the use of encapsulated elemental Se into electrospun microporous multichannel CNF (MCNF) as free-standing cathodes ( $\sim 38.4$  wt%,  $1.33$  mg/cm<sup>2</sup> Se in the final cathode) for long cycle life in RT Na-Se batteries (Fig. 14 (h)).<sup>57</sup>

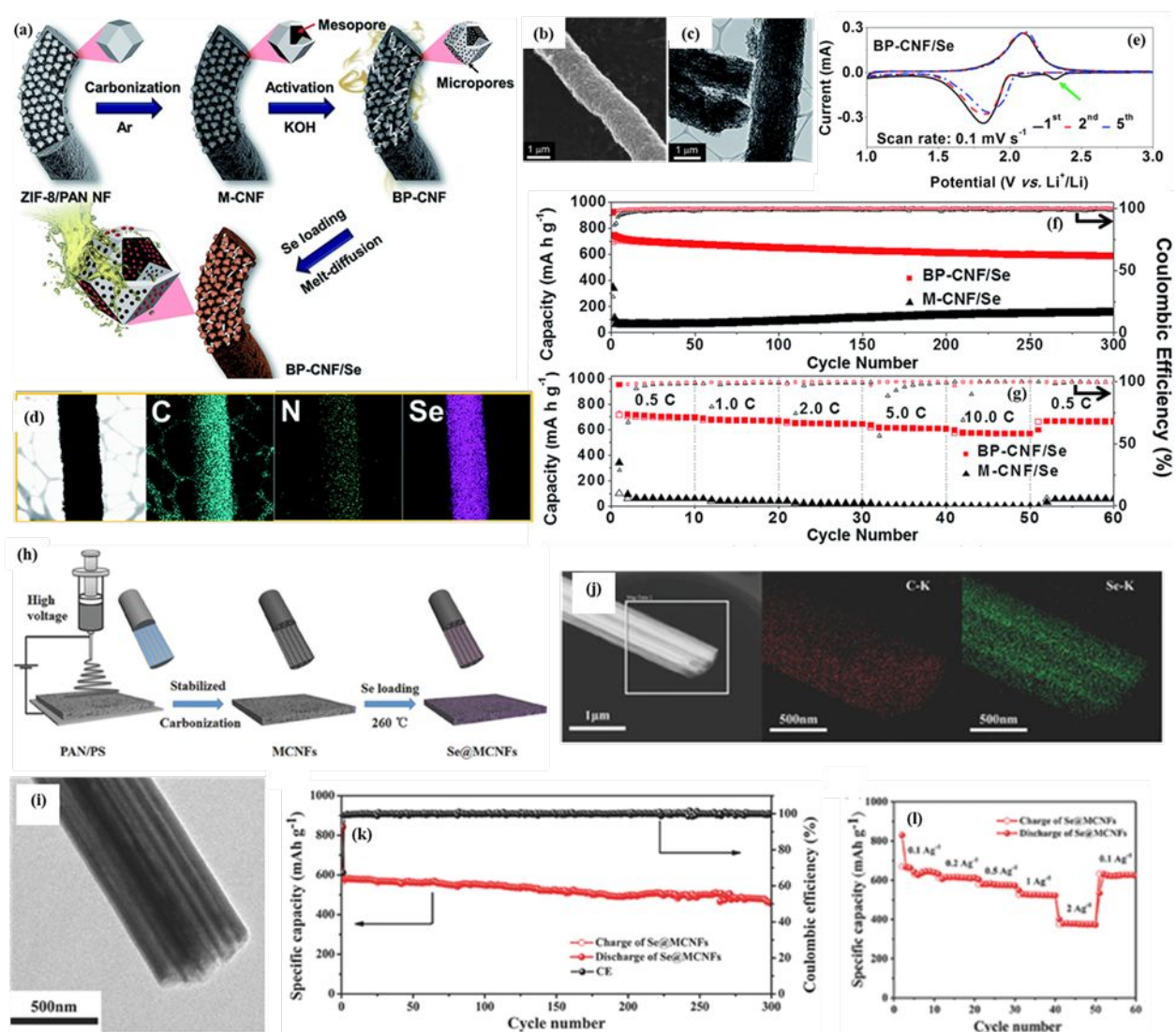


Fig. 14 (a) Formation mechanism of bimodal porous nitrogen-doped carbon nanofiber homogeneously filled with chain-like Se (c-Se), (b-c) SEM and TEM images of BP-CNF sample,

(d) Elemental mapping images of Se/BP-CNF cathodes, (e) Cyclic voltammograms (CV) of the Se/BP-CNF cathode obtained at 0.1 mV/s in the potential range of 1.0–3.0 V for the 1<sup>st</sup>, 2<sup>nd</sup>, and 5<sup>th</sup> cycles, (f-g) Cycling performance at a current density of 0.5C, and rate performances with the coulombic efficiencies for Se/BP-CNF and Se/M-CNF cathodes (Reproduced with permission from ref. 264. Copyright The Royal Society of Chemistry 2018); (h) Schematic illustration of the synthesis process for Se@MCNF electrode, (i-j) TEM image and elemental mapping of the Se@MCNF composite. Red and green correspond to C and Se, respectively. (k) Long-term cycling performance of RT Na-Se cell based on the Se@MCNF composite at a current density of 0.5 A/g, and (l) Rate capability of the Se@MCNF composite at various current densities (Reproduced with permission from ref. 57. Copyright 2017 WILEY-VCH Verlag GmbH & Co. KGaA, Weinheim).

The MCNFs were fabricated by electrospinning a solution of polystyrene (PS)/PAN in DMF solvent and carbonizing the pre-oxidized (280°C, 3 h, air) PAN/PS nanofibers at 800°C for 1 h in N<sub>2</sub> gas flow. The Se was infiltrated into MCNF by heating MCNF and Se powder together at 260°C for 12 h in a stainless steel vessel sealed under argon atmosphere. The TEM image and elemental maps of Se@MCNF showed that Se is uniformly impregnated into micropores and parallel channels present inside the 1D nanofiber structures (Fig. 14 (i-j)).

The electrochemical performance was evaluated using 1 M NaClO<sub>4</sub> in a mixture of EC:DEC solvents as the electrolyte. The RT Na-Se cells based on the flexible freestanding Se@MCNF cathodes delivered a high specific discharge capacity of ~430 mAh/g after 300 cycles at 0.5 A/g with a small capacity decay rate of ~0.067% per cycle (Fig. 14 (k)) and remarkable rate performance up to 2 A/g (379 mAh/g) (Fig. 14 (l)). The excellent electrochemical performance of Se@MCNF cathodes was a consequence of Se-encapsulation into microporous MCNF structures. The encapsulation of Se in MCNF promoted the utilization of Se, alleviated the dissolution and

shuttle of polyselenides into the electrolyte and brought structural stability to the cathode during volume changes. Consequently, the Se@MCNF composite electrode demonstrated excellent rate capability and long-term cycling when used as a cathode in RT Na-Se batteries. In Table 1, we have summarized performance of recently reported RT Na-S, Li-S<sub>x</sub>Se<sub>y</sub>, RT Na-S<sub>x</sub>Se<sub>y</sub>, Li-Se and RT Na-Se cells based on electrospun structures.

Despite the high cost and low specific capacity of Se than S, M-Se (S<sub>x</sub>Se<sub>y</sub>) batteries have invaluable advantages, which make them attractive for future EVs. With a short practical history of only five years, these batteries have delivered promising results and can compete with their M-S counterparts shortly. The encapsulation of Se or S<sub>x</sub>Se<sub>y</sub> into rationally designed freestanding electrospun heterostructures appears to be a promising strategy for future advances of these batteries in conventional carbonate electrolytes. Therefore, more intense research is required to explore various electrospun heterostructures as Se hosts, interlayers and membranes in carbonate-based M-Se (S<sub>1-x</sub>Se<sub>x</sub>) batteries. Future research efforts should also be actively focused on the use of various *ex-situ* and *in-situ* techniques to fundamentally understand about distinct features of Se electrochemistry such as interactions of polyselenides with different host materials, structural and chemical changes in the Se cathode during cycling, and the stability of the S-Se bond during cycling in M-S<sub>x</sub>Se<sub>y</sub> batteries.

Table 1: Performance of RT Na-S, Li-S<sub>x</sub>Se<sub>y</sub>, RT Na-S<sub>x</sub>Se<sub>y</sub>, Li-Se and RT Na-Se cells based on electrospun structures

Sr. No.	Electrode Structure	Electrolyte	Capacity	Cycling
1 <sup>235</sup>	SPAN/super p/PVDF 53.9 wt%, 0.7-0.84 mg/cm <sup>2</sup> S	0.8 M NaClO <sub>4</sub> in EC:DEC (1:1=v/v)	Na-S: 219 mAh/g <sub>total</sub> at C/10 (5 <sup>th</sup> cycle)	70% retention after 500 cycles
2 <sup>244</sup>	SPAN (free-standing) 41.0 wt%, ~0.3 mg/cm <sup>2</sup> S	1 M NaPF <sub>6</sub> in EC:DEC (1:1=v/v)	Na-S: 342 mAh/g <sub>sulfur</sub> at C/10	77.7% retention after 200 cycles

3 <sup>107</sup>	Carbon hollow nanobubbles on N- and O- co-doped porous carbon nanofibers (CHNBs@PCNF)/S 80 wt% active materials: 10 wt% carbon black: 10 wt% carboxyl methylated cellulose (CMC) 57.0 wt%, ~1.4 mg/cm <sup>2</sup> S	1.0 M NaClO <sub>4</sub> in EC:PC (1:1=v/v)	Na-S: 1214 mAh/g <sub>sulfur</sub> at C/10	65.0% retention after 50 cycles
4 <sup>247</sup>	S/BaTiO <sub>3</sub> -CNF-TiO <sub>2</sub> 60.0 wt%, 1.2-1.4 mg/cm <sup>2</sup> S (free-standing)	1.0 M NaClO <sub>4</sub> in EC:DEC (1:1=v/v)	Na-S: 592 mAh/g <sub>sulfur</sub> at 0.5 A/g	103.21% retention after 400 cycles
5 <sup>265</sup>	S <sub>99.96</sub> Se <sub>0.04</sub> /Porous CNF 60.0 wt%, 0.8-1.0 mg/cm <sup>2</sup> S <sub>99.96</sub> Se <sub>0.04</sub> (free-standing)	1 M LiPF <sub>6</sub> in EC: DMC (1:1=v/v); 1.0 M NaClO <sub>4</sub> in EC:PC (1:1=v/v)	Li-S: 1100 mAh/g <sub>S-Se</sub> at 0.1 A/g Na-S: 1375 mAh/g <sub>S-Se</sub> at 0.1 A/g	76.4% (Li-S) and 55.4% (Na-S) after 100 cycles
6 <sup>252</sup>	S <sub>0.6</sub> Se <sub>0.4</sub> /CNF 57.5 wt%, 0.9 mg/cm <sup>2</sup> S <sub>0.6</sub> Se <sub>0.4</sub> (free-standing)	1 M LiPF <sub>6</sub> in EC: DEC (1:1=v/v); 1.0 M NaClO <sub>4</sub> in EC:PC (1:1=v/v)	Li-S: ~350 mAh/g <sub>S-Se</sub> at 1 A/g Na-S: 417 mAh/g <sub>S-Se</sub> at 0.1 A/g	~100% (Li-S) retention after 1000 cycles and 90% (Na-S) retention after 100 cycles
7 <sup>262</sup>	Se/CNFs-CNT 35 wt% Se (free-standing)	1 M LiPF <sub>6</sub> in EC: DEC (1:1=v/v); 1.0 M NaClO <sub>4</sub> in EC:DEC (1:1=v/v)	Li-Se: ~950 mAh/g <sub>Se</sub> at 0.5 A/g Na-Se: 781 mAh/g <sub>Se</sub> at 0.05 A/g	~54.4% (Li-Se) retention after 500 cycles and 74.6% (Na-Se) retention after 80 cycles

8 <sup>263</sup>	Se/hierarchical porous CNF– rGO 80wt% active material: 10 wt% acetylene Black: 10 wt% PVDF 57 wt% Se	1 M LiPF <sub>6</sub> in EC: EMC:DMC (mass ratio 1:1:1)	Li-Se: ~632 mAh/g <sub>Se</sub> at C/5	~97.5% retention after 50 cycles
9 <sup>264</sup>	Se-infiltrated MOF-derived porous CNF 70wt% active material: 10 wt% carbon (Super P): 10 wt% sodium carboxymethyl cellulose (CMC) 42 wt% Se	1 M LiPF <sub>6</sub> in EC: DEC (1:1=v/v)	Li-Se: ~742 mAh/g <sub>Se</sub> at C/2 (2 <sup>nd</sup> cycle)	~79.2% retention (from 2 <sup>nd</sup> cycle) after 300 cycles
10 <sup>57</sup>	Se/microporous multichannel CNF 80wt% active material: 10 wt% acetylene Black: 10 wt% PVDF ~38.4 wt%. 1.33 mg/cm <sup>2</sup> Se	1.0 M NaClO <sub>4</sub> in EC:DEC (1:1=v/v)	Na-Se: ~578 mAh/g <sub>Se</sub> at 0.5 A/g (2 <sup>nd</sup> cycle)	~74.4% retention (from 2 <sup>nd</sup> cycle) after 300 cycles

#### 4. Statistical analysis of the electrochemical performance:

To understand advantages of electrospun free-standing nanostructures, we provide a comparative analysis for recently reported Li-S cells based on non-electrospun powdered, slurry-cast electrospun and free-standing electrospun nanostructures. Because it is challenging to compare the electrochemical performance of literature reports due to large differences in sulfur fraction/areal loading, conditioning cycles, and the resulting capacity, we have introduced ‘fraction

of (electrochemically) active cathode (FAC)' as a parameter to account for these differences as given below:

$$FAC (\%) = \frac{f_s \times C_s}{C_{th}} = 100 \times \frac{C_s \times W_s}{(W_T)} \times \frac{1}{C_{th}}$$

$$FAC' (\%) = 100 \times \frac{C_s \times W_s}{(W_T + A * W_{Al})} \times \frac{1}{C_{th}}$$

Where  $f_s$  is the sulfur content (weight %) in the final cathode,  $C_{th}$  is the theoretical capacity of sulfur (1675 mAh/g),  $C_s$  is the specific capacity (mAh/g) at a given C rate,  $W_s$  is the absolute sulfur amount in the cathode (mg),  $W_T$  is the absolute total weight of the cathode including binders, and conducting additives (mg),  $A$  is the area of the electrode ( $\text{cm}^2$ , equals to absolute sulfur weight/areal loading of sulfur),  $W_{Al}$  is the areal loading of the additional current collector (Al-foil,  $4 \text{ mg/cm}^2$ ). The first equation for FAC represents the sulfur (active) content in the cathode without the weight of the additional Al-foil (current collector), which is usually  $3\text{-}5 \text{ mg/cm}^2$ . We have considered areal loading of the Al-foil as  $4 \text{ mg/cm}^2$  for the present analysis. The second equation for FAC' includes the weight of the additional Al-foil as well. The 'FAC' can be seen as a fraction of sulfur electrochemically active in the final cathode (i.e., sulfur content in the final cathode multiplied by ratio of achieved capacity at a given C rate and theoretical capacity), which is the source for the cell capacity. The concept of fraction of (electrochemically) active cathode (FAC) will be of great importance in future to represent reliable electrochemical performances as FAC would be more realistic than sulfur content in the composites or in the final cathodes. Since, RT Na-S and M-Se batteries are in their nascent stage, we have not included these reports for the FAC calculations. The comparative analysis of FAC for non-electrospun powdered, slurry-cast electrospun and free-standing electrospun nanostructures have led to the following conclusions:

(a) As mentioned in the introduction section, an areal sulfur loading of  $\geq 5 \text{ mg/cm}^2$  along with high sulfur content ( $\geq 70\%$  in the final cathode), sulfur utilization ( $\geq 70\%$ ) and low E/S ratio of  $\sim 3\text{-}4$

$\mu\text{L}/\text{mg}$  is required for commercialization of Li-S cells in order to outperform the energy density of commercial Li-ion batteries. In other words, practical Li-S cells demand an areal sulfur loading of  $\geq 5 \text{ mg}/\text{cm}^2$  along with FAC of  $\sim 50\%$  (green line in figures) and E/S ratio of  $\sim 3\text{-}4 \mu\text{L}/\text{mg}$ . Fig. 15 (a) presents the calculated FAC for recently reported various non-electrospun powdered, slurry-cast electrospun and free-standing electrospun nanostructures based Li-S cells. The FAC for most of the non-electrospun powdered and slurry-cast electrospun nanostructures based Li-S cells are between 20-50%. In contrast, FAC values for most of the free-standing electrospun nanostructures based Li-S cells are lying between 30-60%.

(b) The effect of additional current collector i.e. Al-foil can be clearly seen in the Fig. 15 (b), which represents the calculated FAC content based on the total weight of the cathode material (including binders and conducting additives) and the weight of the Al-foil. The FAC content for non-electrospun powdered and slurry-cast electrospun nanostructures based electrodes are significantly reduced to  $\leq 30\%$  whereas FAC content for free-standing electrospun nanostructures based electrodes remains unchanged.

(c) Fig. 15 (c) shows the FAC content (including Al-foil weight) as functions of areal loading of sulfur and E/S ratio. Although free-standing electrospun nanostructures based electrodes exhibit relatively higher FAC content, it is still a challenge to construct such electrodes at high sulfur loading and use them at low E/S ratio as evident from Fig. 15 (c).

The free-standing 3D architecture of electrospun nanostructures not only provides continuous 1D pathways for electrons, better wettability, and robust electrode structure but also accommodates volume changes during oxidation/reduction. In contrast, the morphology and the porosity of powdered material-based cathodes after the harsh slurry process and their effect on the device performance are uncomprehended. Moreover, these free-standing architectures eliminate



the need of additional dead weight. In contrast, the use of specially designed powdered nanostructures as a sulfur host involves harsh slurry-cast process with the use of inactive heavy elements such as binders/conductive agents (e.g., 10 wt% conducting carbon and 10 wt% poly(vinylidene fluoride)) and additional current collectors (Aluminum, usually 3-5 mg/cm<sup>2</sup>). The presence of these additional dead elements deteriorates the final effective specific capacity (or FAC content) of packed Li-S cells. For example, for a free-standing carbon nanostructure based S-cathode with 70 wt% sulfur in the S/C composite (total areal loading of S/C composite = 1 mg/cm<sup>2</sup> and area of electrode = 1 cm<sup>2</sup>; no binder, no additive, no Al-foil) and 1000 mAh/g capacity at a given C rate, the FAC content will be around 42%. In contrast, for a powdered carbon nanostructure based S-cathode with 70 wt% sulfur in the composite (total areal loading of S/C composite with binder and conducting additive = 1 mg/cm<sup>2</sup>, area of electrode = 1 cm<sup>2</sup>) and 1000 mAh/g capacity at a given C rate, the FAC content will be around 33%, considering 20 wt.% being binders and conductive additive. Further, if we include the weight of additional current collector (Al foil, ~4 mg/cm<sup>2</sup>) used to prepare cathode during slurry cast process, the FAC content for this powdered S/C nanostructure will further reduce to ~7% only. Undoubtedly, free-standing electrospun nanostructures pave the way for improving the electrochemical performance of Li-S batteries by eliminating dead elements —binders, conducting additives and additional Al-foil collector as evident from Fig. 15. The intensive research carried out on the development of advanced electrospun nanostructures in recent years has brought consistent progress in these batteries in terms of capacity, rate capability, and cycle stability as discussed in this review article. With recent achievements and advanced efforts, we believe that the development of rationally designed free-standing 3D electrospun nanostructures with high sulfur loading, and high FAC

content, and low E/S ratio will be an important topic of research in future years for practicality of Li-S batteries.

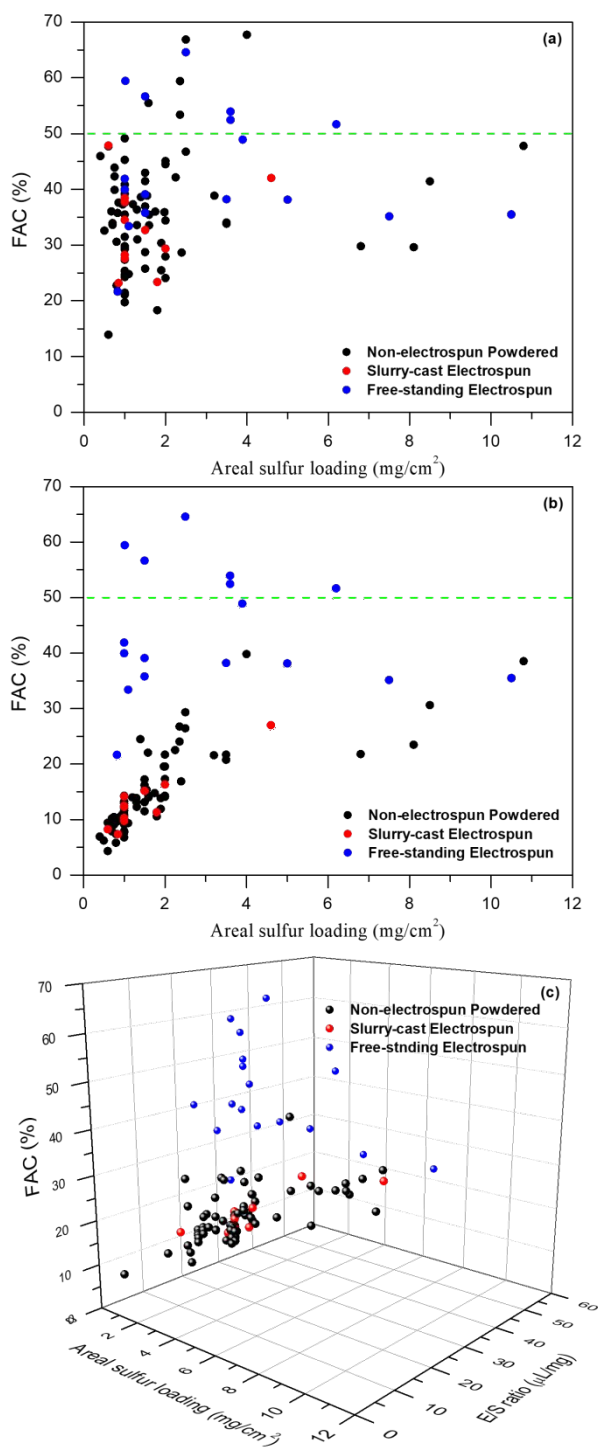


Fig. 15 (a) 'Fraction of (electrochemically) active cathode (FAC)' in the final cathode (without the weight of additional Al-current collector) vs. areal sulfur loading for various non-electrospun

powdered, slurry-cast electrospun, and free-standing electrospun nanostructures based Li-S cells reported recently in the literature, (b) 'Fraction of (electrochemically) active cathode (FAC)' in the final cathode (including the weight of additional Al-current collector- 4 mg/cm<sup>2</sup>) vs. areal sulfur loading for various non-electrospun powdered, slurry-cast electrospun, and free-standing electrospun nanostructures based Li-S cells reported recently in the literature, (c) 'Fraction of (electrochemically) active cathode (FAC)' in the final cathode (including the weight of additional Al-current collector- 4 mg/cm<sup>2</sup>) vs. areal sulfur loading and electrolyte to sulfur (E/S) ratio for various non-electrospun powdered, slurry-cast electrospun, and free-standing electrospun nanostructures based Li-S cells reported recently in the literature. The area of the electrodes/cathodes, E/S ratio, and interlayer weight are considered as 1 cm<sup>2</sup>, 20 μL/mg, and 1 mg, respectively for the papers, which haven't reported these values. Moreover, we have calculated the 'Fraction of (electrochemically) active cathode (FAC)' at C/10, C/5, C/2 and 1C rates for a given paper and chosen the maximum value. The dotted green line represents the required FAC value for practicality of Li-S cells.

Another critical issue is that in most of the reports regardless of the cathode structure (electrospun or non-electrospun), the E/S ratio is  $\geq 30$  μL/mg (Fig. 15 (c)). To reflect the effect of electrolyte, we consider that 50% of the cell electrolyte is held within porosity and voids of cathodes. In this scenario, for a given areal sulfur loading (1 mg/cm<sup>2</sup>), sulfur fraction of ~50% in the electrode, and area (A) of the electrode (1 cm<sup>2</sup>), the weight of the electrolyte ( $W_{\text{electrolyte}} = 0.5 * A * A_S * f_S * \rho = 15$  mg,  $\rho$  = electrolyte density (1 mg/μL assumed)) at high E/S ratio (30 μL/mg) becomes a deciding factor for total cell capacity. Therefore, another important step should be to reduce the E/S ratio to 3-4 μL/mg ( $W_{\text{electrolyte}} = 2$  mg) in order to utilize the potential of non-electrospun powdered, slurry-cast electrospun and free-standing electrospun cathodes. In free-

standing electrospun nanostructures, porosity and inherent excessive voids present in 3D architecture necessitate a high E/S ratio for better sulfur utilization, especially at high sulfur loading. Therefore, effect of E/S ratio becomes more dominating in case of free-standing electrospun nanostructures since  $W_T = 2 \text{ mg}$ , and  $A \cdot W_{Al} = 0 \text{ mg}$  due to free-standing nature.

### **5. Concluding remarks and future perspectives:**

In a brief summary, we have systematically reviewed recently reported advanced strategies in novel electrospun electrode materials for S and Se based lithium and sodium batteries. In particular, we have evaluated various electrospun nanostructures including hierarchical porous CNFs, heteroatom doped CNFs, CNF interlayers, catholytes and  $\text{Li}_2\text{S}$  with CNFs, 3D PANI/CNF nanostructures and SPAN in carbonate electrolytes, various electrospun oxides, carbides and metallic heterostructures as hosts, interlayers, and separator coatings in Li-S batteries. In addition, we have discussed porous CNFs and various heterostructures in RT Na-S,  $\text{Li-S}_x\text{Se}_y$ , RT Na-S $_x$ Se $_y$ , Li-Se and RT Na-Se batteries. In section 3.1.1, we have placed an emphasis on the influence of hierarchical porosity and large pore volume of electrospun CNFs to achieve high areal capacity in Li-S cells. The Li-S cells have shown promising performances by (a) tailoring the pore size, pore volume and surface area of electrospun CNFs via different activation agents and sacrificial templates, (b) modifying methods of sulfur infiltration into CNFs, and (c) using  $\text{Li}_2\text{S}$  or catholytes as starting active materials with CNF. Further, in this section, we have discussed the use of heteroatom doped CNFs and novel configurations with porous/functionalized CNF interlayers to improve the electrochemical performance of Li-S cells. In section 3.1.2, we have focused on the (a) use of advanced electrospun nanostructures of conducting polymers in the cathode and cyclized PAN in the interlayers, (b) sulfurized PAN with the conventional carbonate electrolyte, and (c) electrospun membranes as gel polymer electrolytes for achieving high performance in Li-S cells.

Furthermore, in section 3.1.3, this review focuses on the improvement in electrochemical performance of Li-S cells using various electrospun oxide, carbide and metallic heterostructures. The emphasis is placed on the recent approaches for introducing PS-functionality (polar-polar, Lewis acid base or polythionate type) and e-functionality (conductivity and catalytic activity) into single heterostructures by electrospinning organic/inorganic hybrid gels. Finally, in sections 3.2 and 3.3, we have discussed recently reported advanced electrospun nanostructures designed for RT Na-S and M-Se batteries to bring substantial improvements in electrochemical performance.

It is important to note that key factors for practical Li-S batteries are high gravimetric and volumetric capacity, high FAC content, high areal sulfur loading, prolonged cycle life, and cheap mass production of materials. Despite the considerable progress made so far using electrospun nanostructures, there are still several bottlenecks and substantial development room for performance enhancement in Li-S batteries. One of the long-lasting challenges is the development of high-performance thick (high-sulfur loading) free-standing S-cathodes. The limited diffusion pathways, electrolyte uptake and kinetics, and severe pulverization in thick S-cathodes result in poor sulfur utilization and short cycle life. Therefore, the development of thick S-electrodes using free-standing electrospun nanostructures demands a 3D architecture that can accommodate a large amount of sulfur and the corresponding volume expansion, maintain the electron conducting and ionic pathways over cycling, effectively suppress the shuttle, while minimizing the electrolyte volume. Important factors to be considered while developing such free-standing 3D architectures are porosity, pore volume, void size, surface area, and electrical conductivity. The use of recently reported hierarchically porous (micropores for polysulfide blocking and mesopores for high S loading) electrospun nanostructures is one of the promising solutions to develop thick S-cathodes with high areal loading and FAC content. We emphasize that the influence of parameters of

electrospun nanostructures (porosity, pore volume, void size, surface area, and electrical conductivity) should be further studied to comprehensively understand the correlations between structural features/surface activity of nanostructures and sulfur loading/FAC content, which will eventually help to achieve optimal electrochemical performance. Further, simply increasing the sulfur loading in free-standing electrospun nanostructures only deteriorates the overall cell performance and neutralizes the advantages of electrospun materials. Therefore, new cell configurations also need to be investigated. One possible approach is to construct layer-by-layer 3D S-cathodes using free-standing nanostructures where the thin top and bottom layers (highly microporous) function as polysulfide trapping layers, and the central layers with hierarchical (micro-meso) porosity serve as hosts for large amount of sulfur. The areal sulfur loading, and electrochemical performance can be augmented by adjusting the number of layers and tuning PS functionality (micro-porosity, heteroatom doping, oxides, carbides etc.) into top and bottom layers. Second, uniform dispersion of S into host matrix is essential for high sulfur utilization, especially at high S-loadings. The commonly used S melt-infiltration techniques result in formation of large inactive cores of sulfur (poor S utilization) into voids/inter-fiber macropores of free-standing electrospun 3D architecture, especially in thick electrodes. Therefore, alternative approaches for sulfur impregnation should also be explored to develop thick free-standing 3D electrodes. The possible solutions are (a) chemical synthesis of nanosized sulfur directly on the electrospun architecture, (b) use of catholytes.

To ensure high capacities and prolong cycling, especially at high sulfur loading, not only the texture properties but also the electronic conductivity of electrospun nanostructures is paramount. The use of 3D architectures of heteroatom doped hierarchically porous electrospun CNFs further decorated with conducting nanoparticles (e.g. non-stoichiometric oxides such as

Ti<sub>4</sub>O<sub>7</sub>, TiO; carbides e.g. TiC or metallic Co nanoparticles) would serve as ideal candidates for developing thick S-cathodes. Nevertheless, it is important to control the low mass-fraction/loading (3-5%) of electrochemically inactive functional species (e.g., oxides, carbides, metals) for achieving high FAC content.

Finally, it is worth mentioning that the poor packing of electrospun nanofibers in free-standing 3D architectures usually results in low volumetric density. The continuous alignment of nanofibers during electrospinning would be possible strategy not only to improve sulfur distribution within electrospun host matrix (due to small sized voids in aligned fibers) but also to increase the volumetric energy in Li-S batteries. The use of recently developed free-standing electrospun Li<sub>2</sub>S nanostructures is also recommended to build Li-anode free practical Li-S batteries with high energy density. These free-standing Li<sub>2</sub>S nanostructures not only can overcome the initial activation barrier associated with micro-sized powdered Li<sub>2</sub>S particles but also can be combined with alternate (Si, carbon) anodes.

Another important factor is E/S ratio, which is crucial for designing high energy density Li-S cells. As mentioned earlier, inter-fiber macropores/voids of free-standing 3D architecture of electrospun nanofibers necessitate a high E/S ratio in Li-S batteries. In this context, the use of catholytes or GPEs with rationally designed free-standing electrospun nanostructures having PS and e-functionality (conductivity, polysulfide trapping capability and catalytic activity) would be possible approaches to simultaneously reduce E/S ratio and achieve high sulfur loading (or FAC content) in cathodes. The sulfurized PAN or similar covalently-bonded sulfur based electrospun nanostructures are also interesting as the required amount of electrolyte for such materials is essentially the same as that for Li-ion batteries. However, grafted or tethered polysulfide chains could be more useful than covalently bonded S-atoms in order to simultaneously achieve high

sulfur content in the final cathode. The continuous depletion of electrolyte during cycling due to side reactions with metallic anode also accounts for high E/S ratio. Therefore, integration of free-standing electrospun nanostructured based cathodes with stabilized metallic anode (with stable SEI layers) may be a promising strategy for achieving low E/S ratio.

The RT Na-S battery systems are still in their nascent stage. Due to the large size of  $\text{Na}^+$  than  $\text{Li}^+$ , the volume change of the sulfur cathode ( $\sim 260\%$  for complete reduction of S to  $\text{Na}_2\text{S}$ ) will be one of the most critical issues for RT Na-S batteries, even more severe than for the analogous Li-S batteries. In this regard, development of advanced electrospun nanostructures to accommodate the volume expansion of sulfur cathodes during deep charge/discharge will be more demanding. The electrospun carbon nanostructures with fine tuning of porosity (ions and electron pathways), surface functionality (e.g., heteroatoms), and well embedded ultrafine nanoparticles of conducting non-stoichiometric oxides or metals can lead to high capacity, long-term cycling and circumvent the pulverization (particle cracking and fracture induced by volume expansion) of electrode during sodiation/de-sodiation. Similarly, selenium based battery systems viz., Li- $\text{S}_x\text{Se}_y$ , RT Na- $\text{S}_x\text{Se}_y$ , Li-Se, and RT Na-Se are also in their nascent stage. One of the promising approaches is to leverage the semiconducting nature of selenium to address the poor conductivity of S-cathodes to improve sulfur utilization, and rate performance. The S-Se mixtures are miscible in all proportions, and various  $\text{S}_x\text{Se}_y$  compounds can be prepared, including  $\text{SSe}_5$ ,  $\text{S}_2\text{Se}_5$ ,  $\text{S}_4\text{Se}_5$ ,  $\text{SSe}$ ,  $\text{S}_5\text{Se}_3$ ,  $\text{S}_2\text{Se}$ , and  $\text{S}_7\text{Se}$ , as well as a  $\text{S}_x\text{Se}_y$  compound with a very low amount of Se such as  $\text{S}_{20}\text{Se}$ . These  $\text{S}_x\text{Se}_y$  materials offer higher theoretical capacities (675–1550 mAh/g) compared to Se alone, with substantially improved conductivity compared to that of pure S electrode. On the other side, the electrical conductivity is not an issue for the Se electrode in Li-Se and RT Na-Se batteries due to its semiconducting nature. However, in both M-Se and M- $\text{S}_x\text{Se}_y$  batteries, shuttling of



intermediate polyselenides and volume expansion are major bottlenecks. Therefore, the current progress made over the last few years in Li-S cells using free-standing electrospun nanostructures should be exerted extensively for significant breakthroughs in Se based battery systems. Future studies should focus on the (a) development of rationally designed advanced free-standing electrospun nanostructures for high performance thick Se cathodes, (b) optimization of S:Se ratio in  $S_xSe_y$  compounds for optimal performance in terms of capacity, cycling, and rate capability, and (c) new devices configurations with layer-by-layer 3D cathodes, functional interlayers and separators. Furthermore, research efforts on the fundamental understanding of electrochemistry involved (reduction/oxidation mechanisms and performance deteriorating factors) in M-Se ( $S_xSe_y$ ) systems under different electrolyte systems are vital.

It is critical to maintain the intrinsic properties of electrospun nanostructures under a high production rate. The controllability and degree of accuracy achievable in the fabrication process of electrospun nanostructures are important for their application on an industrial scale. In terms of reproducibility and accuracy in the production stage, electrospun nanostructures are affected by solution (viscosity, concentration, electrical conductivity, surface tension), equipment (flow rate, voltage), and environmental process parameters (humidity, temperature). We have discussed all these parameters in brief in section 2. For more information, we refer the readers to review articles focusing on various electrospun fabrication techniques, conditions/parameters for product reproducibility, and challenges and prospects for transition of electrospinning technology from lab-scale to mass production.<sup>53-55,74,75,77,85</sup> We believe that research should also be centered on fabrication strategies for low cost and industrial scale production of electrospun nanostructures to meet the demand of abovementioned practical battery systems. It remains a major bottleneck to produce electrospun nanostructures on industrial scale using single-nozzle electrospinning

technique because the rate of fiber production depends on concentration, the density of spinning jets and the volume of solution forming spinning jet. Multi-nozzle electrospinning, bubble electrospinning, and needleless electrospinning are promising alternatives to single-nozzle electrospinning technique for mass-production of electrospun nanostructures with high reproducibility. However, at present, these new techniques are too expensive. Nevertheless, these electrospinning techniques will be promising candidates to realize cost-effective large scale production of free-standing nanostructures in the near future.

### Acknowledgements:

The authors would like to thank National Science Foundation (Award#s CMMI-1537827, CBET-1804374) and Drexel Ventures Innovations Fund (DVIF) for funding. The authors would like to thank Ayda Rafie for her assistance with the preparation of figures presented in the conclusion section.

**Conflicts of interest:** There are no conflicts to declare.

### References:

- 1 Z. Yang, J. Zhang, M. C. Kintner-Meyer, X. Lu, D. Choi, J. P. Lemmon and J. Liu, *Chem. Rev.*, 2011, **111**, 3577-3613.
- 2 J. Muldoon, C. B. Bucur and T. Gregory, *Chem. Rev.*, 2014, **114**, 11683-11720.
- 3 H. Ibrahim, A. Ilinca and J. Perron, *Renewable Sustainable Energy Rev.*, 2008, **12**, 1221-1250.
- 4 I. Hadjipaschalis, A. Poullikkas and V. Efthimiou, *Renewable and Sustainable Energy Rev.*, 2009, **13**, 1513-1522.
- 5 K. M. Abraham, *J. Phys. Chem. Lett.*, 2015, **6**, 830-844.
- 6 C. Wadia, P. Albertus and V. Srinivasan, *J. Power Sources*, 2011, **196**, 1593-1598.
- 7 J. Liu, J.-G. Zhang, Z. Yang, J. P. Lemmon, C. Imhoff, G. L. Graff, L. Li, J. Hu, C. Wang, J. Xiao, G. Xia, V. V. Viswanathan, S. Baskaran, V. Sprenkle, X. Li, Y. Shao and B. Schwenzler, *Adv. Funct. Mater.*, 2013, **23**, 929-946.
- 8 J. Yan, Q. Wang, T. Wei and Z. Fan, *Adv. Energy Mater.*, 2014, **4**, 1300816-1300858.
- 9 G. Wang, L. Zhang and J. Zhang, *Chem. Soc. Rev.*, 2012, **41**, 797-828.
- 10 S. M. Mousavi G, F. Faraji, A. Majazi and K. Al-Haddad, *Renewable Sustainable Energy Rev.*, 2017, **67**, 477-490.
- 11 S. Rehman, L. M. Al-Hadhrani and M. M. Alam, *Renewable Sustainable Energy Rev.*, 2015, **44**, 586-598.
- 12 M. Budt, D. Wolf, R. Span and J. Yan, *Appl. Energy*, 2016, **170**, 250-268.
- 13 Y. Sun, N. Liu and Y. Cui, *Nat. Energy*, 2016, **1**, 16071-16082.

- 14 J. Cabana, L. Monconduit, D. Larcher and M. R. Palacin, *Adv. Mater.*, 2010, **22**, E170-E192.
- 15 M. S. Whittingham, *Chem. Rev.*, 2004, **104**, 4271-4301.
- 16 N. Nitta, F. Wu, J. T. Lee and G. Yushin, *Mater. Today*, 2015, **18**, 252-264.
- 17 G. E. Blomgren, *J. Electrochem. Soc.*, 2017, **164**, A5019-A5025.
- 18 M. N. Obrovac and V. L. Chevrier, *Chem. Rev.*, 2014, **114**, 11444-11502.
- 19 M. M. Thackeray, C. Wolverton and E. D. Isaacs, *Energy Environ. Sci.*, 2012, **5**, 7854-7863.
- 20 A. Manthiram, *ACS Cent. Sci.*, 2017, **3**, 1063-1069.
- 21 M. S. Whittingham, *Chem. Rev.*, 2014, **114**, 11414-11443.
- 22 M. R. Palacin, *Chem. Soc. Rev.*, 2009, **38**, 2565-2575.
- 23 M. Wild, L. O'Neill, T. Zhang, R. Purkayastha, G. Minton, M. Marinescu and G. J. Offer, *Energy Environ. Sci.*, 2015, **8**, 3477-3494.
- 24 R. Chen, R. Luo, Y. Huang, F. Wu and L. Li, *Adv. Sci.*, 2016, **3**, 1600051-1600089.
- 25 J. Pan, Y. Y. Xu, H. Yang, Z. Dong, H. Liu and B. Y. Xia, *Adv. Sci.*, 2018, **5**, 1700691-1700720.
- 26 D. Aurbach, B. D. McCloskey, L. F. Nazar and P. G. Bruce, *Nat. Energy*, 2016, **1**, 16128-16138.
- 27 Y. Liu, Q. Sun, W. Li, K. R. Adair, J. Li and X. Sun, *Green Energy Environ.*, 2017, **2**, 246-277.
- 28 A. Manthiram and X. Yu, *Small*, 2015, **11**, 2108-2114.
- 29 P. Saha, M. K. Datta, O. I. Velikokhatnyi, A. Manivannan, D. Alman and P. N. Kumta, *Prog. Mater. Sci.*, 2014, **66**, 1-86.
- 30 L. J. Hardwick and C. P. de León, *Johnson Matthey Technol. Rev.*, 2018, **62**, 134-149.
- 31 L. D. Chen, J. K. Nørskov and A. C. Luntz, *J. Phys. Chem. C*, 2015, **119**, 19660-19667.
- 32 J. G. Smith, J. Naruse, H. Hiramatsu and D. J. Siegel, *Chem. Mater.*, 2017, **29**, 3152-3163.
- 33 A. A. Yaroshevsky, *Geochem. Int.*, 2006, **44**, 48-55.
- 34 Z. Hu and S. Gao, *Chem. Geol.*, 2008, **253**, 205-221.
- 35 W. Guo and Y. Fu, *Energy Environ. Mater.*, 2018, **1**, 20-27.
- 36 A. Manthiram, Y. Fu, S. H. Chung, C. Zu and Y. S. Su, *Chem. Rev.*, 2014, **114**, 11751-11787.
- 37 P. G. Bruce, S. A. Freunberger, L. J. Hardwick and J. M. Tarascon, *Nat. Mater.*, 2012, **11**, 19-29.
- 38 R. Demir-Cakan, M. Morcrette, Gangulibabu, A. Guéguen, R. Dedryvère and J.-M. Tarascon, *Energy Environ. Sci.*, 2013, **6**, 176-182.
- 39 M. K. Song, E. J. Cairns and Y. Zhang, *Nanoscale*, 2013, **5**, 2186-2204.
- 40 Z. Zhao-Karger and M. Fichtner, *MRS Commun.*, 2017, **7**, 770-784.
- 41 A. Robba, A. Vizintin, J. Bitenc, G. Mali, I. Arčon, M. Kavčič, M. Žitnik, K. Bučar, G. Aquilanti, C. Martineau-Corcós, A. Randon-Vitanova and R. Dominko, *Chem. Mater.*, 2017, **29**, 9555-9564.
- 42 P. G. Bruce, B. Scrosati and J. M. Tarascon, *Angew. Chem. Int. Ed. Engl.*, 2008, **47**, 2930-2946.
- 43 Y. Yang, G. Zheng and Y. Cui, *Chem. Soc. Rev.*, 2013, **42**, 3018-3032.
- 44 X. Fang and H. Peng, *Small*, 2015, **11**, 1488-1511.
- 45 W. Kang, N. Deng, J. Ju, Q. Li, D. Wu, X. Ma, L. Li, M. Naebe and B. Cheng, *Nanoscale*, 2016, **8**, 16541-16588.
- 46 Y. X. Yin, S. Xin, Y. G. Guo and L. J. Wan, *Angew. Chem. Int. Ed.*, 2013, **52**, 13186-13200.
- 47 C. P. Yang, Y. X. Yin and Y. G. Guo, *J. Phys. Chem. Lett.*, 2015, **6**, 256-266.
- 48 A. Abouimrane, D. Dambournet, K. W. Chapman, P. J. Chupas, W. Weng and K. Amine, *J. Am. Chem. Soc.*, 2012, **134**, 4505-4508.
- 49 Y. Liu, Z. Tai, Q. Zhang, H. Wang, W. K. Pang, H. K. Liu, K. Konstantinov and Z. Guo, *Nano Energy*, 2017, **35**, 36-43.
- 50 G.-L. Xu, J. Liu, R. Amine, Z. Chen and K. Amine, *ACS Energy Lett.*, 2017, **2**, 605-614.
- 51 A. Eftekhari, *Sustainable Energy Fuels*, 2017, **1**, 14-29.
- 52 L. Li, S. Peng, J. K. Y. Lee, D. Ji, M. Srinivasan and S. Ramakrishna, *Nano Energy*, 2017, **39**, 111-139.

- 53 J. V. Patil, S. S. Mali, A. S. Kamble, C. K. Hong, J. H. Kim and P. S. Patil, *Appl. Surf. Sci.*, 2017, **423**, 641-674.
- 54 S. Cavaliere, S. Subianto, I. Savych, D. J. Jones and J. Rozière, *Energy Environ. Sci.*, 2011, **4**, 4761-4785.
- 55 Z. Dong, S. J. Kennedy and Y. Wu, *J. Power Sources*, 2011, **196**, 4886-4904.
- 56 Q. Liu, J. Zhu, L. Zhang and Y. Qiu, *Renewable Sustainable Energy Rev.*, 2018, **81**, 1825-1858.
- 57 B. Yuan, X. Sun, L. Zeng, Y. Yu and Q. Wang, *Small*, 2018, **14**, 1703252-1703258.
- 58 H. J. Peng, J. Q. Huang and Q. Zhang, *Chem. Soc. Rev.*, 2017, **46**, 5237-5288.
- 59 Z. W. Seh, Y. Sun, Q. Zhang and Y. Cui, *Chem. Soc. Rev.*, 2016, **45**, 5605-5634.
- 60 M. Xu, M. Wang, H. Xu, H. Xue and H. Pang, *Chem. Asian J.*, 2016, **11**, 2967-2995.
- 61 V. Thavasi, G. Singh and S. Ramakrishna, *Energy Environ. Sci.*, 2008, **1**, 205-221.
- 62 X. Li, Y. Chen, H. Huang, Y.-W. Mai and L. Zhou, *Energy Storage Mater.*, 2016, **5**, 58-92.
- 63 J.-W. Jung, C.-L. Lee, S. Yu and I.-D. Kim, *J. Mater. Chem. A*, 2016, **4**, 703-750.
- 64 A. Chinnappan, C. Baskar, S. Baskar, G. Ratheesh and S. Ramakrishna, *J. Mater. Chem. C*, 2017, **5**, 12657-12673.
- 65 Z. Li, J.-w. Zhang, L.-g. Yu and J.-w. Zhang, *J. Mater. Sci.*, 2017, **52**, 6173-6195.
- 66 S. Peng, L. Li, J. Kong Yoong Lee, L. Tian, M. Srinivasan, S. Adams and S. Ramakrishna, *Nano Energy*, 2016, **22**, 361-395.
- 67 B. Zhang, F. Kang, J.-M. Tarascon and J.-K. Kim, *Prog. Mater. Sci.*, 2016, **76**, 319-380.
- 68 S. Kalluri, K. H. Seng, Z. Guo, H. K. Liu and S. X. Dou, *RSC Adv.*, 2013, **3**, 25576-25601.
- 69 L. Mai, J. Sheng, L. Xu, S. Tan and J. Meng, *Acc. Chem. Res.*, 2018, **51**, 950-959.
- 70 L. Zeng, X. Wei, J. Wang, Y. Jiang, W. Li and Y. Yu, *Journal of Power Sources*, 2015, **281**, 461-469.
- 71 Y. He, B. Matthews, J. Wang, L. Song, X. Wang and G. Wu, *J. Mater. Chem. A*, 2018, **6**, 735-753.
- 72 T. Jin, Q. Han, Y. Wang and L. Jiao, *Small*, 2018, **14**, 1703086-1703111.
- 73 W. Li, M. Li, K. R. Adair, X. Sun and Y. Yu, *J. Mater. Chem. A*, 2017, **5**, 13882-13906.
- 74 M. Inagaki, Y. Yang and F. Kang, *Adv. Mater.*, 2012, **24**, 2547-2566.
- 75 S. Agarwal, A. Greiner and J. H. Wendorff, *Prog. Polym Sci.*, 2013, **38**, 963-991.
- 76 V. Beachley and X. Wen, *Mater. Sci. Eng. C Mater. Biol. Appl.*, 2009, **29**, 663-668.
- 77 C. L. Zhang and S. H. Yu, *Chem. Soc. Rev.*, 2014, **43**, 4423-4448.
- 78 S.-H. Chung, P. Han, R. Singhal, V. Kalra and A. Manthiram, *Adv. Energy Mater.*, 2015, **5**, 1500738-1500749.
- 79 A. Singh and V. Kalra, *ACS Appl. Mater. Interfaces*, 2018, **10**, 37937-37947.
- 80 S. H. Chung, R. Singhal, V. Kalra and A. Manthiram, *J. Phys. Chem. Lett.*, 2015, **6**, 2163-2169.
- 81 J. S. Lee, W. Kim, J. Jang and A. Manthiram, *Adv. Energy Mater.*, 2016, **7**.
- 82 L. Ji, M. Rao, S. Aloni, L. Wang, E. J. Cairns and Y. Zhang, *Energy Environ. Sci.*, 2011, **4**, 5053-5059.
- 83 Y. Chen, X. Li, K.-S. Park, J. Hong, J. Song, L. Zhou, Y.-W. Mai, H. Huang and J. B. Goodenough, *J. Mater. Chem. A*, 2014, **2**, 10126-10130.
- 84 Z. Li, J. T. Zhang, Y. M. Chen, J. Li and X. W. Lou, *Nat. Commun.*, 2015, **6**, 8850-8857.
- 85 A. L. Yarin, *Polym. Adv. Technol.*, 2011, **22**, 310-317.
- 86 H. Qu, S. Wei and Z. Guo, *J. Mater. Chem. A*, 2013, **1**, 11513-11528.
- 87 J. Jin, X. Tian, N. Srikanth, L. B. Kong and K. Zhou, *J. Mater. Chem. A*, 2017, **5**, 10110-10126.
- 88 H. Lv, R. Chen, X. Wang, Y. Hu, Y. Wang, T. Chen, L. Ma, G. Zhu, J. Liang, Z. Tie, J. Liu and Z. Jin, *ACS Appl. Mater. Interfaces*, 2017, **9**, 25232-25238.
- 89 A. Rosenman, E. Markevich, G. Salitra, D. Aurbach, A. Garsuch and F. F. Chesneau, *Adv. Energy Mater.*, 2015, **5**, 1500212-1500232.
- 90 Y.-X. Wang, B. Zhang, W. Lai, Y. Xu, S.-L. Chou, H.-K. Liu and S.-X. Dou, *Adv. Energy Mater.*, 2017, **7**, 1602829-1602845.

- 91 R. Fang, S. Zhao, Z. Sun, D. W. Wang, H. M. Cheng and F. Li, *Adv. Mater.*, 2017, **29**, 1606823-1606847.
- 92 A. Manthiram, S. H. Chung and C. Zu, *Adv. Mater.*, 2015, **27**, 1980-2006.
- 93 P. Adelhelm, P. Hartmann, C. L. Bender, M. Busche, C. Eufinger and J. Janek, *Beilstein J. Nanotechnol.*, 2015, **6**, 1016-1055.
- 94 X. Yu and A. Manthiram, *J. Phys. Chem. C*, 2014, **118**, 22952-22959.
- 95 J. Xu, J. Ma, Q. Fan, S. Guo and S. Dou, *Adv. Mater.*, 2017, **29**, 1606454-1606473.
- 96 L. Borchardt, M. Oschatz and S. Kaskel, *Chem. Eur. J.*, 2016, **22**, 7324-7351.
- 97 G. Zheng, Y. Yang, J. J. Cha, S. S. Hong and Y. Cui, *Nano Lett.*, 2011, **11**, 4462-4467.
- 98 K. Fu, Y. Li, M. Dirican, C. Chen, Y. Lu, J. Zhu, Y. Li, L. Cao, P. D. Bradford and X. Zhang, *Chem. Commun.*, 2014, **50**, 10277-10280.
- 99 Y. Wu, M. Gao, X. Li, Y. Liu and H. Pan, *Journal of Alloys and Compounds*, 2014, **608**, 220-228.
- 100 L. Zeng, F. Pan, W. Li, Y. Jiang, X. Zhong and Y. Yu, *Nanoscale*, 2014, **6**, 9579-9587.
- 101 H. Wang, C. Zhang, Z. Chen, H. K. Liu and Z. Guo, *Carbon*, 2015, **81**, 782-787.
- 102 F. Wu, L. Shi, D. Mu, H. Xu and B. Wu, *Carbon*, 2015, **86**, 146-155.
- 103 C.-H. Chang, S.-H. Chung and A. Manthiram, *Mater. Horiz.*, 2017, **4**, 249-258.
- 104 D. Yang, W. Ni, J. Cheng, Z. Wang, T. Wang, Q. Guan, Y. Zhang, H. Wu, X. Li and B. Wang, *Appl. Surf. Sci.*, 2017, **413**, 209-218.
- 105 Y. Zhang, P. Wang, H. Tan, X. Fan and K. Huang, *J. Electrochem. Soc.*, 2018, **165**, A741-A745.
- 106 Y. Wang, *Int. J. Electrochem. Sci.*, 2018, **13**, 8388-8395.
- 107 G. Xia, L. Zhang, X. Chen, Y. Huang, D. Sun, F. Fang, Z. Guo and X. Yu, *Energy Storage Mater.*, 2018, **14**, 314-323.
- 108 J. H. Yun, J. H. Kim, D. K. Kim and H. W. Lee, *Nano Lett.*, 2018, **18**, 475-481.
- 109 X.-Q. Zhang, B. He, W.-C. Li and A.-H. Lu, *Nano Res.*, 2018, **11**, 1238-1246.
- 110 Y. Z. Zhang, Z. Zhang, S. Liu, G. R. Li and X. P. Gao, *ACS Appl. Mater. Interfaces*, 2018, **10**, 8749-8757.
- 111 X. Zhao, M. Kim, Y. Liu, H.-J. Ahn, K.-W. Kim, K.-K. Cho and J.-H. Ahn, *Carbon*, 2018, **128**, 138-146.
- 112 J. Scholz, B. Kayaalp, A. C. Juhl, D. Clemens, M. Fröba and S. Mascotto, *ACS Energy Lett.*, 2018, **3**, 387-392.
- 113 Q. Pang, X. Liang, C. Y. Kwok and L. F. Nazar, *J. Electrochem. Soc.*, 2015, **162**, A2567-A2576.
- 114 Q. Pang, X. Liang, C. Y. Kwok and L. F. Nazar, *Nat. Energy*, 2016, **1**, 16132-16142.
- 115 J. Song, T. Xu, M. L. Gordin, P. Zhu, D. Lv, Y.-B. Jiang, Y. Chen, Y. Duan and D. Wang, *Adv. Funct. Mater.*, 2014, **24**, 1243-1250.
- 116 L. Miao, W. Wang, K. Yuan, Y. Yang and A. Wang, *Chem. Commun.*, 2014, **50**, 13231-13234.
- 117 M. Agostini, J.-Y. Hwang, H. M. Kim, P. Bruni, S. Brutti, F. Croce, A. Matic and Y.-K. Sun, *Adv. Energy Mater.*, 2018, **8**, 1801560-1801566.
- 118 J. Lee, B. Ko, J. Kang, Y. Chung, Y. Kim, W. Halim, J. H. Lee and Y. L. Joo, *Mater. Today Energy*, 2017, **6**, 255-263.
- 119 C. Dillard, S.-H. Chung, A. Singh, A. Manthiram and V. Kalra, *Mater. Today Energy*, 2018, **9**, 336-344.
- 120 S. H. Chung, K. Y. Lai and A. Manthiram, *Adv. Mater.*, 2018, **30**, 1805571-1805577.
- 121 Y. Hwa, J. Zhao and E. J. Cairns, *Nano Lett.*, 2015, **15**, 3479-3486.
- 122 F. Wu, H. Kim, A. Magasinski, J. T. Lee, H.-T. Lin and G. Yushin, *Adv. Energy Mater.*, 2014, **4**, 1400196-1400202.
- 123 C. Nan, Z. Lin, H. Liao, M. K. Song, Y. Li and E. J. Cairns, *J. Am. Chem. Soc.*, 2014, **136**, 4659-4663.
- 124 K. Cai, M. K. Song, E. J. Cairns and Y. Zhang, *Nano Lett.*, 2012, **12**, 6474-6479.
- 125 M. Yu, Z. Wang, Y. Wang, Y. Dong and J. Qiu, *Adv. Energy Mater.*, 2017, **7**, 1700018-1700027.

- 126 F. Ye, Y. Hou, M. Liu, W. Li, X. Yang, Y. Qiu, L. Zhou, H. Li, Y. Xu and Y. Zhang, *Nanoscale*, 2015, **7**, 9472-9476.
- 127 D. H. Lim, M. Agostini, F. Nitze, J. Manuel, J. H. Ahn and A. Matic, *Sci. Rep.*, 2017, **7**, 6327-6335.
- 128 X. Yu and A. Manthiram, *Phys Chem Chem Phys*, 2015, **17**, 2127-2136.
- 129 S. Han, X. Pu, X. Li, M. Liu, M. Li, N. Feng, S. Dou and W. Hu, *Electrochim. Acta*, 2017, **241**, 406-413.
- 130 W. Ren, W. Ma, S. Zhang and B. Tang, *Chem. Eng. J.*, 2018, **341**, 441-449.
- 131 Y. Liang, N. Deng, J. Ju, X. Zhou, J. Yan, C. Zhong, W. Kang and B. Cheng, *Electrochim. Acta*, 2018, **281**, 257-265.
- 132 X. Li, N. Fu, J. Zou, X. Zeng, Y. Chen, L. Zhou and H. Huang, *Mater. Lett.*, 2017, **209**, 505-508.
- 133 W. Zhou, C. Wang, Q. Zhang, H. D. Abruña, Y. He, J. Wang, S. X. Mao and X. Xiao, *Adv. Energy Mater.*, 2015, **5**, 1401752-1401759.
- 134 L. Zhou, X. Lin, T. Huang and A. Yu, *Electrochim. Acta*, 2014, **116**, 210-216.
- 135 J. Yang, J. Xie, X. Zhou, Y. Zou, J. Tang, S. Wang, F. Chen and L. Wang, *J. Phys. Chem. C*, 2014, **118**, 1800-1807.
- 136 F. Sun, J. Wang, H. Chen, W. Li, W. Qiao, D. Long and L. Ling, *ACS Appl. Mater. Interfaces*, 2013, **5**, 5630-5638.
- 137 C. P. Yang, Y. X. Yin, H. Ye, K. C. Jiang, J. Zhang and Y. G. Guo, *ACS Appl. Mater. Interfaces*, 2014, **6**, 8789-8795.
- 138 X. Li and X. Sun, *Front. Energy Res.*, 2014, **2**, 1-9.
- 139 J. Song, M. L. Gordin, T. Xu, S. Chen, Z. Yu, H. Sohn, J. Lu, Y. Ren, Y. Duan and D. Wang, *Angew Chem. Int. Ed.*, 2015, **54**, 4325-4329.
- 140 T. Z. Hou, X. Chen, H. J. Peng, J. Q. Huang, B. Q. Li, Q. Zhang and B. Li, *Small*, 2016, **12**, 3283-3291.
- 141 X.-B. Cheng, J.-Q. Huang, H.-J. Peng, J.-Q. Nie, X.-Y. Liu, Q. Zhang and F. Wei, *Journal of Power Sources*, 2014, **253**, 263-268.
- 142 S. S. Zhang, *Inorg. Chem. Front.*, 2015, **2**, 1059-1069.
- 143 G. Zhou, E. Paek, G. S. Hwang and A. Manthiram, *Nat. Commun.*, 2015, **6**, 7760-7770.
- 144 B. P. Vinayan, T. Diemant, X.-M. Lin, M. A. Cambaz, U. Golla-Schindler, U. Kaiser, R. Jürgen Behm and M. Fichtner, *Adv. Mater. Interfaces*, 2016, **3**, 1600372-1600381.
- 145 Y. Qiu, W. Li, W. Zhao, G. Li, Y. Hou, M. Liu, L. Zhou, F. Ye, H. Li, Z. Wei, S. Yang, W. Duan, Y. Ye, J. Guo and Y. Zhang, *Nano Lett.*, 2014, **14**, 4821-4827.
- 146 H. Wu, Y. Huang, S. Xu, W. Zhang, K. Wang and M. Zong, *Chem. Eng. J.*, 2017, **327**, 855-867.
- 147 T. Gao, Z. Yu, Z.-H. Huang and Y. Yang, *ACS Appl. Energy Mater.*, 2018, **2**, 777-787.
- 148 S. Yao, S. Xue, S. Peng, M. Jing, X. Shen, T. Li and Z. YiLiu, *Int. J. Energy Res.*, 2019, 1-11.
- 149 Y. S. Su and A. Manthiram, *Nat. Commun.*, 2012, **3**, 1166-1171.
- 150 B. P. Williams and Y. L. Joo, *J. Electrochem. Soc.*, 2016, **163**, A2745-A2756.
- 151 J. Wang, Y. Yang and F. Kang, *Electrochim. Acta*, 2015, **168**, 271-276.
- 152 R. Singhal, S.-H. Chung, A. Manthiram and V. Kalra, *J. Mater. Chem. A*, 2015, **3**, 4530-4538.
- 153 Y. Cui, X. Wu, J. Wu, J. Zeng, A. P. Baker, F. Lu, X. Liang, J. Ouyang, J. Huang, X. Liu, Z. Li and X. Zhang, *Energy Storage Mater.*, 2017, **9**, 1-10.
- 154 Y. Yang, W. Sun, J. Zhang, X. Yue, Z. Wang and K. Sun, *Electrochim. Acta*, 2016, **209**, 691-699.
- 155 D. K. Lee, C. W. Ahn and H.-J. Jeon, *J. Power Sources*, 2017, **360**, 559-568.
- 156 K. Wu, Y. Hu, Z. Shen, R. Chen, X. He, Z. Cheng and P. Pan, *J. Mater. Chem. A*, 2018, **6**, 2693-2699.
- 157 P. M. Shanthi, P. J. Hanumantha, T. Albuquerque, B. Gattu and P. N. Kumta, *ACS Appl. Energy Mater.*, 2018, **1**, 483-494.

- 158 S. Zeng, L. Li, D. Zhao, J. Liu, W. Niu, N. Wang and S. Chen, *J. Phys. Chem. C*, 2017, **121**, 2495-2503.
- 159 A. Freitag, M. Stamm and L. Ionov, *J. Power Sources*, 2017, **363**, 384-391.
- 160 P. T. Dirlam, R. S. Glass, K. Char and J. Pyun, *J. Polym. Sci., Part A: Polym. Chem.*, 2017, **55**, 1635-1668.
- 161 W. J. Chung, J. J. Griebel, E. T. Kim, H. Yoon, A. G. Simmonds, H. J. Ji, P. T. Dirlam, R. S. Glass, J. J. Wie, N. A. Nguyen, B. W. Guralnick, J. Park, A. Somogyi, P. Theato, M. E. Mackay, Y. E. Sung, K. Char and J. Pyun, *Nat. Chem.*, 2013, **5**, 518-524.
- 162 Y. Zhang, K. Li, H. Li, Y. Peng, Y. Wang, J. Wang and J. Zhao, *J. Mater. Chem. A*, 2017, **5**, 97-101.
- 163 K. Park, J. H. Cho, J.-H. Jang, B.-C. Yu, A. T. De La Hoz, K. M. Miller, C. J. Ellison and J. B. Goodenough, *Energy Environ. Sci.*, 2015, **8**, 2389-2395.
- 164 S. Matsuda, Y. Kubo, K. Uosaki and S. Nakanishi, *ACS Energy Lett.*, 2017, **2**, 924-929.
- 165 P. Zhu, J. Zhu, C. Yan, M. Dirican, J. Zang, H. Jia, Y. Li, Y. Kiyak, H. Tan and X. Zhang, *Adv. Mater. Interfaces*, 2018, **5**, 1701598-1701607.
- 166 Y. Liu, A. K. Haridas, Y. Lee, K.-K. Cho and J.-H. Ahn, *Appl. Surf. Sci.*, 2018, In press.
- 167 S. K. Simotwo and V. Kalra, *Curr. Opin. Chem. Eng.*, 2016, **13**, 150-160.
- 168 L. Wang, X. He, J. Li, M. Chen, J. Gao and C. Jiang, *Electrochim. Acta*, 2012, **72**, 114-119.
- 169 D.-H. Lim, M. Agostini, J.-H. Ahn and A. Matic, *Energy Technol.*, 2018, **6**, 1214-1219.
- 170 W. Zhou, Y. Yu, H. Chen, F. J. DiSalvo and H. D. Abruna, *J. Am. Chem. Soc.*, 2013, **135**, 16736-16743.
- 171 Q. Li, M. Liu, X. Qin, J. Wu, W. Han, G. Liang, D. Zhou, Y.-B. He, B. Li and F. Kang, *J. Mater. Chem. A*, 2016, **4**, 12973-12980.
- 172 X. Song, S. Wang, Y. Bao, G. Liu, W. Sun, L.-X. Ding, H. Liu and H. Wang, *J. Mater. Chem. A*, 2017, **5**, 6832-6839.
- 173 P. Zhu, J. Zhu, J. Zang, C. Chen, Y. Lu, M. Jiang, C. Yan, M. Dirican, R. Kalai Selvan and X. Zhang, *J. Mater. Chem. A*, 2017, **5**, 15096-15104.
- 174 Z. Zhou, T. Zhao, X. Lu, H. Cao, X. Zha and Z. Zhou, *J. Power Sources*, 2018, **396**, 542-550.
- 175 S. Huang, R. Guan, S. Wang, M. Xiao, D. Han, L. Sun and Y. Meng, *Prog. Polym. Sci.*, 2018, In press.
- 176 L. Xiao, Y. Cao, J. Xiao, B. Schwenzer, M. H. Engelhard, L. V. Saraf, Z. Nie, G. J. Exarhos and J. Liu, *Adv. Mater.*, 2012, **24**, 1176-1181.
- 177 M. Liu, Y. Ren, D. Zhou, H. Jiang, F. Kang and T. Zhao, *ACS Appl. Mater. Interfaces*, 2017, **9**, 2526-2534.
- 178 S. S. Zhang and D. T. Tran, *Electrochim. Acta*, 2013, **114**, 296-302.
- 179 S. Choi, J. Song, C. Wang, S. Park and G. Wang, *Chem. Asian J.*, 2017, **12**, 1470-1474.
- 180 H. Li, M. Li, S. H. Siyal, M. Zhu, J.-L. Lan, G. Sui, Y. Yu, W. Zhong and X. Yang, *J. Membr. Sci.*, 2018, **555**, 169-176.
- 181 W. Sven, H. Andreas and B. M. R., *J. Electrochem. Soc.*, 165, **165**, A2093-A2095.
- 182 Q. Li, J. Chen, L. Fan, X. Kong and Y. Lu, *Green Energy Environ.*, 2016, **1**, 18-42.
- 183 R. Kumar, J. Liu, J.-Y. Hwang and Y.-K. Sun, *J. Mater. Chem. A*, 2018, **6**, 11582-11605.
- 184 S. Zhang, K. Ueno, K. Dokko and M. Watanabe, *Adv. Energy Mater.*, 2015, **5**, 1500117-1500144.
- 185 C. Qu, Y. Chen, X. Yang, H. Zhang, X. Li and H. Zhang, *Nano Energy*, 2017, **39**, 262-272.
- 186 P. M. Shanthi, P. J. Hanumantha, B. Gattu, M. Sweeney, M. K. Datta and P. N. Kumta, *Electrochim. Acta*, 2017, **229**, 208-218.
- 187 T. Yim, M.-S. Park, J.-S. Yu, K. J. Kim, K. Y. Im, J.-H. Kim, G. Jeong, Y. N. Jo, S.-G. Woo, K. S. Kang, I. Lee and Y.-J. Kim, *Electrochim. Acta*, 2013, **107**, 454-460.
- 188 L. Hu, Y. Lu, T. Zhang, T. Huang, Y. Zhu and Y. Qian, *ACS Appl. Mater. Interfaces*, 2017, **9**, 13813-13818.

- 189 Y. Z. Zhang, Z. Z. Wu, G. L. Pan, S. Liu and X. P. Gao, *ACS Appl. Mater. Interfaces*, 2017, **9**, 12436-12444.
- 190 G. Liang, J. Wu, X. Qin, M. Liu, Q. Li, Y. B. He, J. K. Kim, B. Li and F. Kang, *ACS Appl. Mater. Interfaces*, 2016, **8**, 23105-23113.
- 191 X. Chen, H.-J. Peng, R. Zhang, T.-Z. Hou, J.-Q. Huang, B. Li and Q. Zhang, *ACS Energy Lett.*, 2017, **2**, 795-801.
- 192 Z. Li, J. Zhang and X. W. Lou, *Angew. Chem. Int. Ed.*, 2015, **54**, 12886-12890.
- 193 C. Shang, L. Cao, M. Yang, Z. Wang, M. Li, G. Zhou, X. Wang and Z. Lu, *Energy Storage Mater.*, 2018, In press.
- 194 J. Balach, J. Linnemann, T. Jaumann and L. Giebeler, *J. Mater. Chem. A*, 2018, **6**, 23127-23168.
- 195 X. Liu, J. Q. Huang, Q. Zhang and L. Mai, *Adv. Mater.*, 2017, **29**, 1601759-1601783.
- 196 C. Li, Z. Xi, D. Guo, X. Chen and L. Yin, *Small*, 2018, **14**, 1701986-1702006.
- 197 Y. Zhong, K. R. Yang, W. Liu, P. He, V. Batista and H. Wang, *J. Phys. Chem. C*, 2017, **121**, 14222-14227.
- 198 X. Liang, C. Y. Kwok, F. Lodi-Marzano, Q. Pang, M. Cuisinier, H. Huang, C. J. Hart, D. Houtarde, K. Kaup, H. Sommer, T. Brezesinski, J. Janek and L. F. Nazar, *Adv. Energy Mater.*, 2016, **6**, 1501636-1501645.
- 199 M. Liu, Q. Li, X. Qin, G. Liang, W. Han, D. Zhou, Y. B. He, B. Li and F. Kang, *Small*, 2017, **13**, 1602539-1602545.
- 200 J. Zhu, R. Pitcheri, T. Kang, Y. Guo, J. Li and Y. Qiu, *Ceram. Int.*, 2018, **44**, 16837-16843.
- 201 Z. Liu, B. Liu, P. Guo, X. Shang, M. Lv, D. Liu and D. He, *Electrochim. Acta*, 2018, **269**, 180-187.
- 202 C. Guo, H. Yang, A. Naveed, Y. Nuli, J. Yang, Y. Cao, H. Yang and J. Wang, *Chem. Commun.*, 2018, **54**, 8347-8350.
- 203 C.-L. Lee, C. Kim and I.-D. Kim, *RSC Adv.*, 2017, **7**, 44804-44808.
- 204 X. Song, T. Gao, S. Wang, Y. Bao, G. Chen, L.-X. Ding and H. Wang, *J. Power Sources*, 2017, **356**, 172-180.
- 205 Q. Zhang, Y. Wang, Z. W. Seh, Z. Fu, R. Zhang and Y. Cui, *Nano Lett.*, 2015, **15**, 3780-3786.
- 206 Y. Zhang, S. Yao, R. Zhuang, K. Luan, X. Qian, J. Xiang, X. Shen, T. Li, K. Xiao and S. Qin, *J. Alloys Compd.*, 2017, **729**, 1136-1144.
- 207 H. Wei, E. F. Rodriguez, A. S. Best, A. F. Hollenkamp, D. Chen and R. A. Caruso, *Adv. Energy Mater.*, 2016, 1601616-1601625.
- 208 S. Mei, C. J. Jafta, I. Laueremann, Q. Ran, M. Kärge, M. Ballauff and Y. Lu, *Adv. Funct. Mater.*, 2017, **27**, 1701176-1701185.
- 209 Z. Yang, Z. Zhu, J. Ma, D. Xiao, X. Kui, Y. Yao, R. Yu, X. Wei, L. Gu, Y.-S. Hu, H. Li and X. Zhang, *Advanced Energy Materials*, 2016, **6**, 1600806.
- 210 X. Tao, J. Wang, Z. Ying, Q. Cai, G. Zheng, Y. Gan, H. Huang, Y. Xia, C. Liang, W. Zhang and Y. Cui, *Nano Lett.*, 2014, **14**, 5288-5294.
- 211 B. Xu, H. Y. Sohn, Y. Mohassab and Y. Lan, *RSC Adv.*, 2016, **6**, 79706-79722.
- 212 H. Tang, S. Yao, S. Xue, M. Liu, L. Chen, M. Jing, X. Shen, T. Li, K. Xiao and S. Qin, *Electrochim. Acta*, 2018, **263**, 158-167.
- 213 T.-T.-N. Nguyen and J.-L. He, *Adv. Powder Technol.*, 2016, **27**, 1868-1873.
- 214 D. Liu, C. Zhang, G. Zhou, W. Lv, G. Ling, L. Zhi and Q. H. Yang, *Adv. Sci.*, 2018, **5**, 1700270-1700281.
- 215 C. Dillard, S.-H. Chung, A. Singh, A. Manthiram and V. Kalra, *Materials Today Energy*, 2018, **9**, 336-344.
- 216 G. Zhou, H. Tian, Y. Jin, X. Tao, B. Liu, R. Zhang, Z. W. Seh, D. Zhuo, Y. Liu, J. Sun, J. Zhao, C. Zu, D. S. Wu, Q. Zhang and Y. Cui, *Proc. Natl. Acad. Sci. U. S. A.*, 2017, **114**, 840-845.



- 217 Y. Yao, W. Feng, M. Chen, X. Zhong, X. Wu, H. Zhang and Y. Yu, *Small*, 2018, **14**, 1802516-1802524.
- 218 Z. Hao, L. Yuan, C. Chen, J. Xiang, Y. Li, Z. Huang, P. Hu and Y. Huang, *J. Mater. Chem. A*, 2016, **4**, 17711-17717.
- 219 J. Deng, J. Guo, J. Li, M. Zeng and D. Gong, *Ceram. Int.*, 2018, **44**, 17340-17344.
- 220 B. Cao, Y. Chen, Li, L. Yin and Y. Mo, *ChemSusChem*, 2016, **9**, 3338-3344.
- 221 L. Ma, H. Yuan, W. Zhang, G. Zhu, Y. Wang, Y. Hu, P. Zhao, R. Chen, T. Chen, J. Liu, Z. Hu and Z. Jin, *Nano Lett.*, 2017, **17**, 7839-7846.
- 222 Z. Yuan, H. J. Peng, T. Z. Hou, J. Q. Huang, C. M. Chen, D. W. Wang, X. B. Cheng, F. Wei and Q. Zhang, *Nano Lett.*, 2016, **16**, 519-527.
- 223 N. Deng, W. Kang, Y. Liu, J. Ju, D. Wu, L. Li, B. S. Hassan and B. Cheng, *J. Power Sources*, 2016, **331**, 132-155.
- 224 Y. Xiang, J. Li, J. Lei, D. Liu, Z. Xie, D. Qu, K. Li, T. Deng and H. Tang, *ChemSusChem*, 2016, **9**, 3023-3039.
- 225 G. Chen, X. Song, S. Wang, Y. Wang, T. Gao, L.-X. Ding and H. Wang, *J. Membr. Sci.*, 2018, **548**, 247-253.
- 226 M. S. Kim, L. Ma, S. Choudhury and L. A. Archer, *Adv. Mater. Interfaces*, 2016, **3**, 1600450-1600457.
- 227 D. Kumar, S. K. Rajouria, S. B. Kuhar and D. K. Kanchan, *Solid State Ionics*, 2017, **312**, 8-16.
- 228 K. B. Hueso, V. Palomares, M. Armand and T. Rojo, *Nano Res.*, 2017, **10**, 4082-4114.
- 229 S. Wenzel, H. Metelmann, C. Raiß, A. K. Dürr, J. Janek and P. Adelhelm, *J. Power Sources*, 2013, **243**, 758-765.
- 230 S. Xin, Y. X. Yin, Y. G. Guo and L. J. Wan, *Adv. Mater.*, 2014, **26**, 1261-1265.
- 231 A. Manthiram and X. Yu, *Small*, 2015, **11**, 2108-2114.
- 232 D. Kumar, S. B. Kuhar and D. K. Kanchan, *J. Energy Storage*, 2018, **18**, 133-148.
- 233 S. Wei, S. Xu, A. Agrawal, S. Choudhury, Y. Lu, Z. Tu, L. Ma and L. A. Archer, *Nat. Commun.*, 2016, **7**, 11722-11731.
- 234 J. Wang, J. Yang, Y. Nuli and R. Holze, *Electrochem. Commun.*, 2007, **9**, 31-34.
- 235 T. H. Hwang, D. S. Jung, J. S. Kim, B. G. Kim and J. W. Choi, *Nano Lett.*, 2013, **13**, 4532-4538.
- 236 H. Ryu, T. Kim, K. Kim, J.-H. Ahn, T. Nam, G. Wang and H.-J. Ahn, *J. Power Sources*, 2011, **196**, 5186-5190.
- 237 X. Yu and A. Manthiram, *J. Phys. Chem. Lett.*, 2014, **5**, 1943-1947.
- 238 I. Bauer, M. Kohl, H. Althues and S. Kaskel, *Chem. Commun.*, 2014, **50**, 3208-3210.
- 239 X. Yu and A. Manthiram, *Chem. Eur. J.*, 2015, **21**, 4233-4237.
- 240 Y. Hao, X. Li, X. Sun and C. Wang, *ChemistrySelect*, 2017, **2**, 9425-9432.
- 241 W. Du, Q. Xu, R. Zhan, Y. Zhang, Y. Luo and M. Xu, *Mater. Lett.*, 2018, **221**, 66-69.
- 242 H. Wang, C. Wang, E. Matios and W. Li, *Angew. Chem. Int. Ed. Engl.*, 2018, **57**, 7734-7737.
- 243 X. Yu and A. Manthiram, *Adv. Energy Mater.*, 2015, **5**, 1500350-1500355.
- 244 I. Kim, C. H. Kim, S. h. Choi, J.-P. Ahn, J.-H. Ahn, K.-W. Kim, E. J. Cairns and H.-J. Ahn, *J. Power Sources*, 2016, **307**, 31-37.
- 245 X. Yu and A. Manthiram, *Chem. Mater.*, 2016, **28**, 896-905.
- 246 Q. Lu, X. Wang, J. Cao, C. Chen, K. Chen, Z. Zhao, Z. Niu and J. Chen, *Energy Storage Mater.*, 2017, **8**, 77-84.
- 247 D. Ma, Y. Li, J. Yang, H. Mi, S. Luo, L. Deng, C. Yan, M. Rauf, P. Zhang, X. Sun, X. Ren, J. Li and H. Zhang, *Adv. Funct. Mater.*, 2018, **28**, 1705537-1705545.
- 248 K. Xie, Y. You, K. Yuan, W. Lu, K. Zhang, F. Xu, M. Ye, S. Ke, C. Shen, X. Zeng, X. Fan and B. Wei, *Adv. Mater.*, 2016, **29**, 1604724-1604729.

- 249 Y. Wei, Y. Tao, Z. Kong, L. Liu, J. Wang, W. Qiao, L. Ling and D. Long, *Energy Storage Mater.*, 2016, **5**, 171-179.
- 250 Z. Li, J. Zhang, H. B. Wu and X. W. D. Lou, *Adv. Energy Mater.*, 2017, **7**, 1700281-1700287.
- 251 X. Li, J. Liang, K. Zhang, Z. Hou, W. Zhang, Y. Zhu and Y. Qian, *Energy Environ. Sci.*, 2015, **8**, 3181-3186.
- 252 Y. Yao, L. Zeng, S. Hu, Y. Jiang, B. Yuan and Y. Yu, *Small*, 2017, **13**, 1603513-1603520.
- 253 B. Kalimuthu and K. Nallathamby, *ACS Appl. Mater. Interfaces*, 2017, **9**, 26756-26770.
- 254 X. Zhao, L. Yin, T. Zhang, M. Zhang, Z. Fang, C. Wang, Y. Wei, G. Chen, D. Zhang, Z. Sun and F. Li, *Nano Energy*, 2018, **49**, 137-146.
- 255 J. Zhou, J. Yang, Z. Xu, T. Zhang, Z. Chen and J. Wang, *J. Mater. Chem. A*, 2017, **5**, 9350-9357.
- 256 Y. J. Hong, K. C. Roh and Y. Chan Kang, *J. Mater. Chem. A*, 2018, **6**, 4152-4160.
- 257 K. Balakumar and N. Kalaiselvi, *Carbon*, 2017, **112**, 79-90.
- 258 J. Ding, H. Zhou, H. Zhang, L. Tong and D. Mitlin, *Adv. Energy Mater.*, 2018, **8**, 1701918-1701927.
- 259 R. Mukkabla, S. Deshagani, P. Meduri, M. Deepa and P. Ghosal, *ACS Energy Lett.*, 2017, **2**, 1288-1295.
- 260 J. He, W. Lv, Y. Chen, J. Xiong, K. Wen, C. Xu, W. Zhang, Y. Li, W. Qin and W. He, *J. Power Sources*, 2017, **363**, 103-109.
- 261 M. Jia, S. Lu, Y. Chen, T. Liu, J. Han, B. Shen, X. Wu, S.-J. Bao, J. Jiang and M. Xu, *J. Power Sources*, 2017, **367**, 17-23.
- 262 L. Zeng, X. Wei, J. Wang, Y. Jiang, W. Li and Y. Yu, *J. Power Sources*, 2015, **281**, 461-469.
- 263 L. Zeng, X. Chen, R. Liu, L. Lin, C. Zheng, L. Xu, F. Luo, Q. Qian, Q. Chen and M. Wei, *J. Mater. Chem. A*, 2017, **5**, 22997-23005.
- 264 S.-K. Park, J.-S. Park and Y. C. Kang, *J. Mater. Chem. A*, 2018, **6**, 1028-1036.
- 265 L. Zeng, Y. Yao, J. Shi, Y. Jiang, W. Li, L. Gu and Y. Yu, *Energy Storage Mater.*, 2016, **5**, 50-57.